# Graphene Transistor Based Nanoelectronic and Nanophotonic Applications

**by**

**Che-Hung Liu**

A dissertation submitted in partial fulfillment
of the requirements for the degree of
Doctor of Philosophy
(Electrical Engineering)
in the University of Michigan
2016

Doctoral Committee:

Associate Professor Zhaohui Zhong, Chair
Assistant Professor Xiaogan Liang
Professor Wei D. Lu
Professor Theodore B. Norris

Dedicated to my family, friends and all above.

# Acknowledgements

I would like to firstly thank my research advisor Prof. Zhaohui Zhong for giving me this treasurable opportunity to pursue my Ph.D. degree at the University of Michigan five years ago with all his unconditional help, guidance, and supports. He taught me the right way to conduct/approach researches and think critically. We went through countless discussions and, of course, sometimes severe arguments. He always tried to push me out of my comfort zone, which made me learn and grow tremendously fast throughout these years. I believe all these things that I learned throughout my Ph.D. is definitely going to be the most valuable asset for my future career.

I would also like to thank all the faculty members I worked with for helping me scrutinize my research results and provide valuable insights. Thanks to Prof. Norris for selflessly providing resources and supports from his lab, especially the ultrafast laser system setup for all the optical measurements. Thanks to Prof. Lu for generously sharing the sophisticated array readout/control system, and even modifying the layout to meet my measurement requirements. Thanks to Prof. Liang for willingly being on the committee

board providing his ideas and suggestions from different aspects. Without them, I won't even have any chances to finish my Ph.D. studies.

In addition, I am very grateful to all my colleagues. Thanks to senior group members, Chung Chiang Wu, Seunghyun Lee, Chang-Hua Liu, Girish Kulkarni, and Kyunghoon Lee, for their guidance and discussion. Furthermore, I deeply appreciate those valuable supports from my collaborators: You-Chia Chang, Miao-Bin Lien, Gong Cheng, Zhen Xu, Yuchao Yang, Chao Du, and Fuxi Cai. Especially, I would like to give many thanks to You-Chia Chang for his important fundamental works and efforts to set up the whole ultrafast optical measurement infrastructures for all my optical measurements. Besides, I would also like to give special thanks to Luke Lee, Michael Kuo, Chu-Hsiang Teng, Chen Lin, Wenbing Hu, Hsun-Jen (Ben) Chuang, Ye-Sheng (Sam) Kuo, Tzu-Wei (Paul) Huang, Te-Hsuan Chen and Yen-Po Chen, for their company, discussion and technical supports throughout my Ph.D. studies.

Finally, and most importantly, I would like to thank my family and all my friends all over the world. It is your constant support, trust, and encouragements that allowed me to pursue knowledge abroad and made me get through all those tough times. I can't imagine how my Ph.D. life will be without anyone of you. Thank you all.

# Table of Contents

Dedication..... ii

Acknowledgements..... iii

List of Figures..... ix

Abstract..... xviii

Chapter 1 Introduction..... 1

1.1 Discovery of Graphene and its Physical Geometry/Morphology..... 3

1.2 Graphene Unique Electrical Properties..... 5

1.2.1 Graphene Energy Band Structure..... 6

1.2.2 High Carrier Mobility in Graphene..... 9

1.2.3 Graphene Ambipolarity..... 10

1.3 Graphene Unique Optical Properties..... 11

1.3.1 Optical Conductivity in Graphene..... 11

1.3.2 Photo-Induced Hot Carriers in Graphene..... 17

1.3.3 High Transparency of Graphene..... 24

1.4 Graphene Synthesis ..... 26

1.5 Thesis Overview ..... 29

Chapter 2 Graphene Ambipolar Nanoelectronics for High Noise Rejection Amplification ..... 31

2.1 Introduction ..... 31

2.2 The Dual-Gate Graphene Ambipolar Device ..... 33

2.3 The Amplification Mechanism for Multi-Mode Operation ..... 37

2.3.1 Common Mode Amplification Operation ..... 39

2.3.2 Differential Mode Amplification Operation ..... 41

2.4 The Common Mode Rejection Ratio (CMRR) ..... 43

2.5 Conclusion ..... 46

Chapter 3 Realization of Mid-Infrared Graphene Hyperbolic Metamaterials ..... 48

3.1 Introduction ..... 48

3.2 Design of Graphene HMM ..... 51

3.3 Characterization of the Optical Conductivity in Graphene ..... 56

3.4 Measurement of the Effective Permittivity of Graphene HMM ..... 60

3.5 Conclusion ..... 66

Chapter 4 Review of Photo-Gating Effect for Broadband and High Responsivity

Graphene Photodetectors ..... 68

4.1 Introduction ..... 68

4.2 Graphene Double-Layer Heterostructure Photodetector ..... 71

4.3 Photo-Gating Effect ..... 73

4.4 Broadband Photodetection ..... 78

4.4.1 Photoresponse in Visible Regime ..... 78

4.4.2 Photoresponse in Near- to Mid-Infrared Regime ..... 81

4.5 Conclusion ..... 83

Chapter 5 Graphene-SOI Heterojunction Broadband and High Responsivity Photodetectors ..... 84

5.1 Introduction ..... 84

5.2 Graphene-SOI Heterojunction Photodetector ..... 85

5.3 Device I-V Characterization and Photodetection Measurement ..... 86

5.4 Conclusion ..... 89

Chapter 6 All-Graphene Transparent Heterojunction Broadband Photodetectors for One-Dimensional Light-Field Ranging ..... 90

6.1 Introduction ..... 90

6.2 All-Graphene Transparent Heterojunction Photodetector ..... 91

6.3 Broadband Photodetection Characterization ..... 93

6.4 One-Dimensional Light-Field Ranging ..... 95

6.5 Conclusion ..... 100

Chapter 7 Conclusions and Future Work ..... 102

7.1 Conclusions ..... 102

7.2 Future Work ..... 104

7.2.1 Graphene-SOI Heterojunction Photodetector Image Sensor Array ..... 104

7.2.2 All-Graphene Transparent Photodetector for Light-Field Imaging ..... 106

Bibliography ..... 109

# List of Figures

Figure 1-1 Diverse forms of $sp^2$ graphitic materials composed of a basic building block – graphene, which can be wrapped up into 0D fullerenes, rolled into 1D CNTs or stacked into 3D graphite [7]. ..... 4

Figure 1-2 The transmission electron microscope (TEM) images of graphene. (a) A high-resolution image directly taken at 80 kV in the TEAM 0.5. The white arrow indicates the edge of the sheet. Scale bar, 4 A. (b) An atomic-resolution image of a clean and structurally perfect synthesized graphene sheet. Individual carbon atoms appear white in the image. The image was obtained through the reconstruction of the electron exit wave function from 15 lattice images using MacTempas software [9]. ..... 5

Figure 1-3 (a) Hexagonal crystal lattice of graphene. $a_1$ and $a_2$ are the lattice unit vectors and $\delta_i$, i=1,2,3 are the nearest-neighbor vectors. (b) The corresponding Brillouin zone and the Dirac cones are located at K and K' points [8]..... 6

Figure 1-4 The three-dimensional (3D) energy dispersions of graphene crystal lattice. The conductance band touches at K and K' points [8]..... 8

Figure 1-5 Ambipolar electric field effect in single layer graphene. The insets show its low energy spectrum, indicating changes in the position of the Fermi energy $E_F$ with respect to the varying gate biases [7]..... 10

Figure 1-6 (a) The extracted optical conductivity of a monolayer CVD graphene sample. (b) The optical conductivity of monolayer graphene predicted by the non-interacting theory with a Fermi level of 277 meV and a scattering rate (in units of energy) of 54 meV. The optical conductivity is normalized to the universal conductivity. The circles and diamonds are the control points of the

cubic splines. ..... 14

Figure 1-7 The extracted optical conductivity of a monolayer CVD graphene sample before and after chemical doping by nitric acid vapor. The optical conductivity is normalized to the universal conductivity. The markers are the control points of the cubic splines. ..... 16

Figure 1-8 Calculated phonon dispersion relation of graphene showing the iLO, iTO, oTO, iLA, iTA and oTA phonon branches. [41]. ..... 18

Figure 1-9 Dynamics of hot carrier cooling in graphene. (a) Photoexcited hot carriers thermalize within the timescale $\tau_1$, and the subsequent cooling via optical phonon emissions occurs on a timescale $\tau_2$. (b) Experimental results of the pump-probe measurements. The curves provide information about the thermalization timescale ($\tau_1$) and relaxation timescale ($\tau_2$) [44]..... 19

Figure 1-10 (Left) Hot carrier relaxation in pristine graphene while each relaxation step is restricted by momentum and energy conservation, resulting in slow hot carrier cooling. (Right) Hot carrier relaxation in disorder-graphene while the disorder relaxes momentum conservation and leads to faster hot carrier cooling [49]. ..... 21

Figure 1-11 Nonlinear photoluminescence in graphene. (a) Inefficient carrier-carrier scattering in the parabolic band. (b) Efficient carrier-carrier scattering in the linear band. (c) The photoluminescence measured from graphene under 1.5 eV pulse excitation [52]. ..... 22

Figure 1-12 The hot carrier created by absorbing (a) a high energy photon and (b) a low energy photon will relax its energy to the electrons in the Fermi sea, which creates multiple hot electrons in the conduction band [54]. ..... 23

Figure 1-13 (a) Photograph of a 50 μm aperture partially covered by graphene and its bilayer. The line scan profile shows the intensity of transmitted white light along the yellow line. The inset is a 20-μm-thick metal support structure with apertures of 20, 30, and 50 μm in diameter with graphene placed over them. (b) Transmittance spectrum of single layer graphene (open circles). Slightly

lower transmittance for λ < 500 nm is probably due to hydrocarbon contamination. The red line is the transmittance $T = (1 + 0.5\pi\alpha) - 2$ expected for two-dimensional Dirac fermions, whereas the green curve takes into account a nonlinearity and triangular warping of graphene's electronic spectrum. The gray area indicates the standard error for our measurements. The inset shoes the transmittance of white light as a function of the number of graphene layers (squares). The dashed lines correspond to an intensity reduction by $\pi\alpha$ with each added layer [56]. ..... 26

Figure 1-14 The growth mechanism of graphene on Cu. (a) Annealing of a Cu foil with native oxide in $H_2$ (b) Nucleation of graphene islands. (c) Coalescing of graphene flakes into a film [73]. ..... 29

Figure 2-1 Device geometry of dual-gate graphene ambipolar device and its I-V characterization. (a) Schematic of the device. Source (S) and drain (D) electrodes are shown in red, and the dual-gate electrodes (G1 and G2) are shown in yellow. (b) The SEM image of the fabricated device. Scale bar, 10 μm. (c) The conductance versus gate voltage response curves for gate 1 (black) and gate 2 (red). The inset illustrates the proposed equivalent circuit symbol of our dual-gate graphene ambipolar device. ..... 35

Figure 2-2 The two-dimensional (2D) color plot of conductance versus gate biasing voltages for dual-gate graphene ambipolar device. The graphene channel can be operated under p-p (lower left), n-n (upper right), p-n (upper left), and n-p (lower right) regions by biasing two gate accordingly. ..... 36

Figure 2-3 The operation mechanism of dual-gate graphene ambipolar device. (a) Schematic showing the common mode operation mechanism. Two AC inputs ($v_{in1}$ and $v_{in2}$) are supplied through two gates, and the output signal ($v_{out}$) is recorded at the drain of the device with source grounded. (b) Schematic showing the differential mode operation mechanism. ..... 37

Figure 2-4 The common mode operation demonstrated by the dual-gate graphene ambipolar device. (a) Diagram of the electrical measurement setup. $R_L$ = 0.5 kohm and $V_{dd}$ = 10 V. (b) The time-traced AC voltage amplitude curves recorded for input and the outputs under n-n, p-n, p-p, and n-p dual-gate

biasing conditions. (c) Two-dimensional color plot of output voltage amplitude versus the dual-gate biasing voltages. In-phase AC inputs ($v_{in}$ = 10 mV) are supplied at two gates during the measurement for common mode operation. ..... 40

Figure 2-5 The circuit diagram of the custom-built phase shift module with 2N3904 NPN BJTs. ..... 41

Figure 2-6 The differential mode operation demonstrated by the dual-gate graphene ambipolar device. (a) Diagram of the electrical measurement setup. $R_L$ = 0.5 kohm and $V_{dd}$ = 10 V. A phase shift circuit is used in one of the gates in order to achieve 180 degrees phase difference between two inputs. (b) The time-traced AC voltage amplitude curves recorded for input and outputs under n-n, p-n, p-p, and n-p dual-gate biasing conditions. (c) Two-dimensional color plot of output voltage amplitude versus the dual-gate biasing voltages. Out-of-phase AC inputs ($v_{in}$ = 10 mV) are supplied at two gates during the measurement for differential mode operation. ..... 42

Figure 2-7 The two-dimensional (2D) color plot of common mode rejection ratio versus the dual-gate biasing voltages. The CMRR values are calculated from the common mode and differential mode measurements plotted in Figure 2-4(c) and Figure 2-6(c). High noise rejection can be achieved with either pn or np differential mode biasing conditions. ..... 44

Figure 2-8 The two-dimensional (2D) color plot of CMRR versus dual-gate biasing voltages for two other devices. Measurements are done under the same condition as in Figure 2-7, and high noise rejection is once again confirmed. ..... 44

Figure 2-9 Frequency spectrum analysis by using a commercial FFT spectrum analyzer (Stanford Research System SR760). The carrier frequency is 30 kHz. ..... 45

Figure 2-10 Output characteristics I-$V_{ds}$ of dual-gate graphene amplifier under different gate bias. There is no current saturation due to the semi-metallic nature of graphene. ..... 46

Figure 3-1 The schematic representation of the graphene-dielectric multilayer structure that turns into a HMM at mid-infrared frequencies. It consists of five periods of alternating CVD graphene sheets and $Al_2O_3$ layers on a $CaF_2$ substrate. The thickness of the $Al_2O_3$ layer is ~ 10 nm. ..... 52

Figure 3-2 The theoretical optical conductivity of graphene. It is plotted with $EF$ = 350 meV and $\hbar\gamma$ = 40 meV. These numbers correspond to heavily doped CVD graphene. At the high-frequency end of the spectrum, graphene is lossy because of the inter-band absorption. At the low-frequency end, graphene is again lossy because of the intra-band free-carrier absorption. There is a useful spectral range in between, where the imaginary part of the optical conductivity exceeds the real part. In this particular example, the useful wavelengths range from 2 to 30 μm in the mid-infrared range. The inset shows another example of lightly doped CVD graphene with $EF$ = 150 meV and $\hbar\gamma$ = 40 meV. The useful wavelength range is smaller when the doping is lower. ..... 55

Figure 3-3 The optical conductivity of CVD graphene measured by ellipsometry. (a) The real and imaginary part of the optical conductivity of the chemically doped CVD graphene (blue and magenta curves) and the unintentionally doped CVD graphene (black and green curves). These curves are mathematically expressed by cubic splines, and the markers denote the control points of the splines. The chemically doped CVD graphene has a larger imaginary conductivity in the mid-infrared range. (b) The real and imaginary part of the optical conductivity of the chemically doped CVD graphene. The blue and magenta curves are obtained by fitting with cubic splines, and the black dash lines are obtained by using the model given by Equation 3-3. The model fitting is consistent with the spline fitting in the mid-infrared range. The extracted $EF$ and $\hbar\gamma$ from the model fitting are 460 and 23 meV, respectively, which corresponds to a mobility of ~ 2,000 $cm^2V^{-1}s^{-1}$. ..... 57

Figure 3-4 Calculation of ellipsometric angles with exact transfer-matrix method and EMA. Ellipsometric angles Ψ and Δ are defined by $rprs = (tan\Psi)ei\Delta$, where $rp$ and $rp$ are the reflection coefficients for p and s light, respectively. They are the quantities an ellipsometer measures. The transfer-matrix method calculates the response of five periods of

graphene-dielectric multilayer structure, while the EMA simulates a homogenized anisotropic layer with the permittivities given by Equation 3-1. This calculation shows that the EMA is an accurate approximation for the structure. The wavelength used in this simulation is 6 μm. The material properties are $\varepsilon d$ = 2.1 and σ = (0.43 + 0.98i)$\sigma 0$. Thickness d = 10 nm. The substrate has a refractive index of 1.39. ..... 62

Figure 3-5 Extraction of the effective permittivity of the graphene HMM. (a,b) The ellipsometric angles Ψ and Δ acquired from the graphene-dielectric multilayer structure. The measurement is performed at incident angles of 47°, 57° and 67°. The blue dash lines show the fitting by homogenizing the multilayer structure into a metamaterial with the effective permittivities given by Equation 3-1. We extract from the fitting that $EF$ = 365 meV and $\hbar\gamma$ = 41 meV. (c) The extracted effective permittivity of the metamaterial, which exhibits an optical topological transition from elliptical to hyperbolic dispersion at 4.5 μm. When the wavelength is at 6 μm, $\varepsilon eff,\parallel$ equals 2.1+0.9i and $\varepsilon eff,\perp$ equals 2.1. (d) The extracted optical conductivity of the constituent CVD graphene in the metamaterial. ..... 63

Figure 4-1 Graphene double-layer heterostructure photodetector. (a) Schematic of device structure. (b) Black (right and top axes): transfer curve for bottom graphene layer using a silicon backgate ($V_{gb}$). Red (left and bottom axes): transfer curve for top graphene layer using the bottom graphene as the gate ($V_{gm}$). From these transport curves, we calculate the Fermi energies of the top and bottom graphene layers to be 4.756 eV and 4.655 eV, respectively. Inset: False- color scanning electron microscopy (SEM) image of the device. The gold areas indicate the metal electrodes and the purple and red areas the bottom and top graphene layers, respectively. Scale bar, 1 μm. ..... 72

Figure 4-2 (a) Schematic of band diagram and photoexcited hot carrier transport under light illumination. Electrons and holes are represented by grey and red spheres, respectively. Vertical arrows represent photoexcitation, and lateral arrows represent tunneling of hot electron (grey) and hole (red). (b) Vertical tunneling current as a function of bias voltage applied across two graphene layers. The bottom layer is grounded, and bias voltage is applied to the top layer. Inset: Schematic band diagrams under forward and reverse bias. Red

dashed lines indicate the Fermi levels of the graphene layers. ..... 74

Figure 4-3 Photoexcited hot carrier tunneling in graphene double-layer heterostructures. (a) Schematic of electrical measurement setup for scanning photocurrent imaging. Photocurrent across the two graphene layers is directly measured to confirm the photoexcited hot carrier tunneling mechanism. (b)(c) Scanning photocurrent images of the graphene double-layer heterostructures at excitation wavelengths of 900 nm (b) and 800 nm (c). Blue dotted lines indicate the edges of the bottom electrodes and red dotted lines the edges of the top electrodes. Vertical tunneling current across the heterostructures was measured under the short-circuit condition with the bottom graphene layer grounded. The laser spot size for these scanning measurements was ~ 1.5 μm, and the laser power was 1 mW. Scale bar, 2 μm. (d) Responsivity comparison of graphene photodetector at wavelengths of 800 nm (red) and 900 nm (blue). (e) Photoresponse of a control device with identical design, except for the absence of the top graphene layer. Inset: Schematic of control device. ..... 77

Figure 4-4 Photoresponse of the graphene double-layer heterostructures in the visible region. (a) $I–V_{gb}$ characteristics of the measured graphene photodetector under different laser powers. The potential of the top graphene layer was allowed to float, while the current of the bottom graphene transistor was measured under 1 V source–drain bias voltage. The laser wavelength is 532 nm with a spot size of 10 μm, covering the entire graphene photodetector. Inset: Energy band diagram of the graphene/$Ta_2O_5$/graphene heterostructures. (b) Gate dependence of photocurrent under different laser powers. (c) Power dependence of photocurrent at 240 V (blue squares) and 220 V (red circles) backgate voltages. Inset: Shift of Dirac point gate voltages as a function of illumination power. (d) Measured photoresponsivity versus illumination power. (e) The magnitude of the photocurrent increases linearly with source–drain bias voltage of the bottom graphene layer transistor. Red lines are linear fits. $V_{gb}$ = 0 V. (f) Temporal photoresponse of the graphene photodetector (black curve). The illumination power is 0.3 μW and the laser wavelength is 532 nm. The laser on–off (red curve) is controlled by a mechanical shutter synchronized with the reset backgate voltage pulses (blue curve). ..... 80

Figure 4-5 Near- to mid-infrared photoresponse of the graphene/silicon/graphene heterostructure photodetector. (a)-(c) Gate dependence of photocurrent under different illumination powers with excitation wavelengths at 1.3 μm (a), 2.1 μm (b), and 3.2 μm (c). Measurements were conducted by applying 1.5 V bias voltage to the bottom graphene transistor, and the laser spots were focused to ~ 20 μm, covering the entire graphene photodetector. (d)-(f) Photocurrent versus illumination power under excitation wavelengths of 1.3 μm (d), 2.1 μm (e), and 3.2 μm (f). Representative curves with backgate voltages set at 260 V (blue squares) and 230 V (red circles) are shown. Inset in (d): band diagram of graphene/silicon/graphene heterostructures..... 82

Figure 5-1 Cross-sectional view of graphene-SOI heterojunction photodetector. ..... 86

Figure 5-2 Characterization of bottom-gated silicon-on-insulator field-effect transistor (BG-SOI-FET). (a) I-$V_g$ transfer curves. (b) I-$V_{ds}$ linear and saturation characteristics..... 87

Figure 5-3 Near-infrared photodetection measurement of the graphene-SOI heterojunction photodetector. (a) I-$V_g$ transfer curves and (b) photocurrent under different laser power illumination. (c) Power dependence photoresponsivity..... 88

Figure 6-1 (a) The schematic of all-graphene transparent heterojunction photodetector. (b) Actual fabricated all-graphene transparent heterojunction photodetectors on a sheet of paper with Univ. of Michigan “M” logo printout..... 92

Figure 6-2 Photoresponse characterization of the all-graphene transparent heterojunction photodetector at 1.2 μm wavelength (signal). (a) I-$V_g$ transfer curves and (b) photocurrents under different laser power illumination. (c)(d) Laser power dependence photocurrent (c) and photoresponsivitiy (d) at gate bias ($V_g$) of -6 V..... 93

Figure 6-3 Photoresponse characterization of the all-graphene transparent heterojunction photodetector at 2.4 μm wavelength (idler). (a) I-$V_g$ transfer curves and (b) photocurrents under different laser power illumination. (c)(d) Laser power dependence photocurrent (c) and photoresponsivitiy (d) at gate bias ($V_g$) of

-7 V. ..... 95

Figure 6-4 (a)(b) Cross-sectional (a) and top-down (b) views of two stacking all-graphene transparent heterojunction broadband photodetectors along the light propagation direction. (c) Schematic of one-dimensional (1D) light-field photodetection optical imaging system. ..... 96

Figure 6-5 (a)(b) Transfer curve (a) and photocurrent (b) for the detector on focal plane 1 (focusing position #1). (c)(d) Transfer curve (c) and photocurrent (d) for the detector on focal plane 2 (focusing position #10). ..... 98

Figure 6-6 Photocurrent versus laser beam focusing position at gate bias ($V_g$) of -5 V for two individual all-graphene transparent heterojunction photodetectors placed along the light propagation direction separated by 2 mm distance. ..... 100

Figure 7-1 (a) Top view of thirty single-pixel devices and two 32 x 32 photodetector arrays fabricated on SOI wafer. (b) The SEM image of graphene-SOI heterojunction photodetectors in array matrix arrangement. (c) Integration of a 32 x 32 array wire-bonded onto a chip carrier mounted on a custom designed PCB board with 4 DACs, 16 matrix switches and a 12-bit ADC. 106

Figure 7-2 Schematic of an optical parametric amplification (OPA) system setup for light-field photodetection with stacked all-graphene transparent heterojunction photodetector arrays along the light propagation direction. 108

# Abstract

Over the past few decades, electronics and photonics have made significant impacts on every aspect of our daily life. Importantly, as the technology advancing and moving forward, the development of these devices not only relies on deeper fundamental understanding but also requires novel materials with unique properties as well as new device architecture to achieve higher performance with more diverse functionalities. In this regards, low dimensional materials inherently possess properties that are conceptually different from those of bulk materials in most aspects. The capability to tailor these nanomaterials as well as their unique properties is essential to achieve unconventional devices with revolutionary impacts.

In this dissertation work, our aim is to develop novel nanoelectronics and nanophotonics by exploiting the extraordinary characteristics of purely two-dimensional (2D) monolayer graphene and its heterostructures. Firstly, we design and propose the dual-gate graphene ambipolar transistor that can operate as either common mode or differential mode amplifier by properly tuning the gate biases. Our device can also

achieve high noise rejection amplification with common mode rejection ration (CMRR) as high as 80 dB, which is comparable to a commercial operational amplifier (op-amp). Secondly, we demonstrate the hyperbolic metamaterials (HMMs) by using precisely controlled periodic graphene-dielectric multilayer nanostructures to investigate the optical topological transition from elliptical to hyperbolic dispersion in mid-infrared regime. Thirdly, we propose the graphene-SOI heterojunction broadband photodetector design to improve the device on-off operation speed, strengthen the photo-gating effect, as well as minimize the dark current. We further fabricate the single pixels into 32 x 32 matrix arrangement to demonstrate the proof-of-concept image array readout, opening up the development of graphene-based ultra-broadband image sensor array applications. Lastly, we propose the all-graphene transparent photodetector design for light-field imaging and demonstrate the proof-of-concept one-dimensional (1D) ranging by using two stacked single-pixel transparent photodetectors. The results should lay the stepping stones and foundation for the new generation of graphene-based light-field photodetectors and image sensors.

# Chapter 1

# Introduction

Over the past few decades, electronics and photonics have been intensively and widely studied then applied due to their significant/tremendous impacts on every aspect of our daily life, including communication, transportation, living, entertainment, lighting, imaging, and sensing…etc. To date, almost nothing can be completely detached from these ultra-fast growing technology trend. Importantly, as the technology advanced and moving forward, the development of these devices not only relies on more fundamental understanding but also requires novel materials with unique properties as well as new device architecture design in order to achieve higher-performance devices with more diverse functionalities. In this regards, nanoscale electronics and photonics exploiting nanomaterials' extraordinary characteristics is envisioned as a promising approach [1]–[5]. First of all, device miniaturization leads to better device performances in terms of speed, power consumption and weights, which was being pursued and contribute to the constant evolution of microelectronics technology. More importantly, miniaturization

may display new functionalities because the dimensionality of materials is eventually reduced, where quantum mechanical effects will play much more significant roles over the classical pictures. These effects lead to unique properties of low dimensional materials that are conceptually different from those of bulk materials in all aspects, including their electrical, optical and mechanical properties... etc. Therefore, the capability to tailor these nanomaterials and their unique properties is essential to achieve unconventional devices with revolutionary impacts.

In this thesis, my aim is to develop novel nanoelectronics and nanophotonics by exploiting the extraordinary characteristics of purely two dimensional (2D) monolayer graphene, where its remarkable electrical, optical properties have been widely and intensively studied since the first discovery in 2004 [6]. In this Chapter, I will start my discussion from graphene's physical geometry in section 1.1; and its electrical properties including carrier mobility, energy band structure and ambipolarity in section 1.2; then its optical properties including optical conductivity, hot carrier behaviors and transparency in sections 1.3; lastly its synthesis processes in section 1.4. To summarize, I will briefly conclude and outline this thesis in section 1.5.

## 1.1 Discovery of Graphene and its Physical Geometry/Morphology

Carbon is the 6th and one of the most distinctive elements in the periodic table that contains four valence electrons, providing various chemical bonding possibilities. Carbon bonds allow almost infinite number of carbon derivatives with other elements, forming the basis of all known organic materials. Moreover, carbon atoms also bond very stably with themselves, such as sp, $sp^2$ and $sp^3$ hybridized orbits. This flexibility of carbon bonding yields a wide variety of organic compounds and carbon allotropes, and more importantly, these different bonding results in distinct properties. For instance, diamond, which is composed of face-centered cubic $sp^3$ hybridized crystalline structure of carbon atoms, is transparent, highly abrasive and acts as an electrical insulator as well as efficient thermal conductor. Conversely, crystalline graphite, which consists of parallel layered sheets of $sp^2$ hybridized carbon atoms, is opaque, an excellent lubricant and good electrical conductor. In addition, the thermal conductivity between parallel carbon sheets is poor. Furthermore, even carbon atoms are connected with the same covalent bond, different physical structures can also yield different properties. This interesting outcome has been revealed since the discovery of diverse $sp^2$ hybridized graphitic materials, such as the zero-dimensional (0D) fullerenes, one-dimensional (1D) carbon nanotubes (CNTs) and three-dimensional (3D) graphite. Essentially, the most fundamental element of these

low dimensional structures is graphene – a purely two-dimensional (2D) monolayer of $sp^2$ hybridized carbon atoms densely packed in a honeycomb crystal lattice, as shown in Figure 1-1.

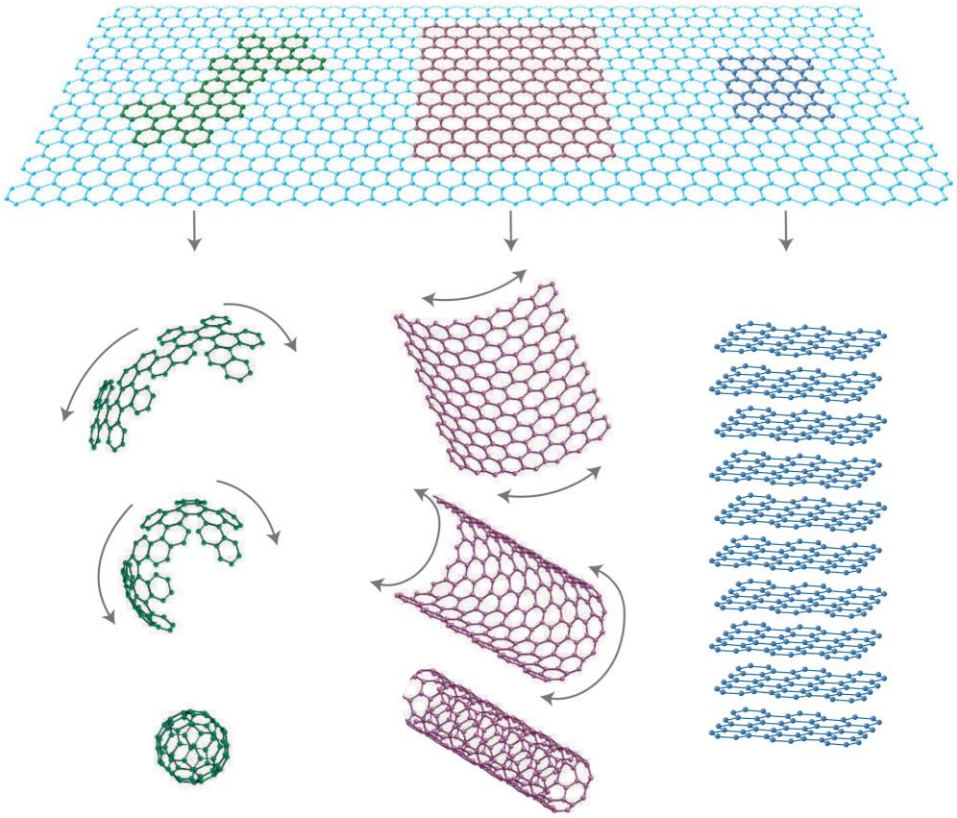

Figure 1-1 Diverse forms of $sp^2$ graphitic materials composed of a basic building block – graphene, which can be wrapped up into 0D fullerenes, rolled into 1D CNTs or stacked into 3D graphite [7].

Due to its unique atomically thick monolayer nature, the preparation of graphene was a big challenge until scientists A. Geim and K. Novoselov successfully exfoliated stand-alone monolayer graphene from bulk graphite in 2004 [6]–[8]. Figure 1-2 shows

the transmission electron microscope (TEM) images of graphene [9], the interatomic distance of two carbon atoms is ~ 1.42 A. Carbon atoms are arranged in a hexagonal crystal lattice, where the structure can be understood as a triangular lattice with a basis of two atoms per unit cell, as shown in Figure 1-3(a). Since discovery, graphene has soon emerged as a promising nanomaterial for novel applications in electronics as well as photonics due to its remarkable electrical and optical properties, which will be explained and discussed in the following subchapters.

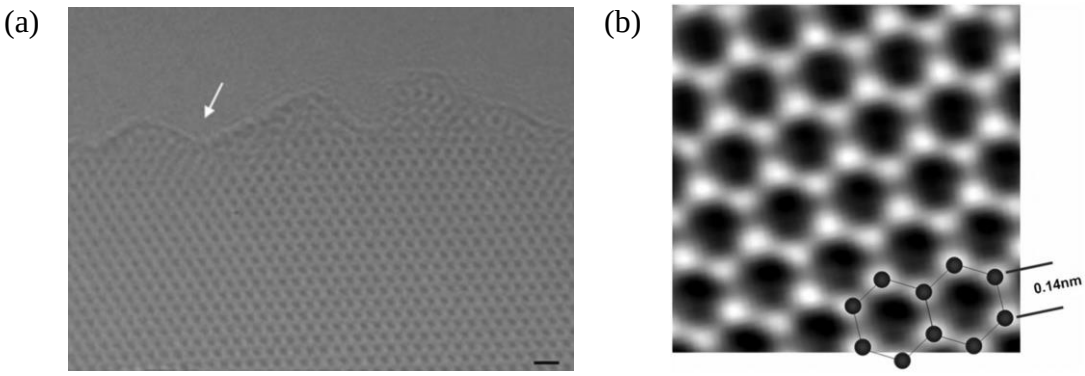


Figure 1-2 The transmission electron microscope (TEM) images of graphene. (a) A high-resolution image directly taken at 80 kV in the TEAM 0.5. The white arrow indicates the edge of the sheet. Scale bar, 4 A. (b) An atomic-resolution image of a clean and structurally perfect synthesized graphene sheet. Individual carbon atoms appear white in the image. The image was obtained through the reconstruction of the electron exit wave function from 15 lattice images using MacTempas software [9].

## 1.2 Graphene Unique Electrical Properties

In this subchapter, I will discuss the electrical properties of graphene which is

utilized and applied to my studies in the thesis, including linear gapless energy band structure (semi-metallic feature), extremely high carrier mobility (high speed/gain transistor application) and its ambipolarity (multi-mode operation).

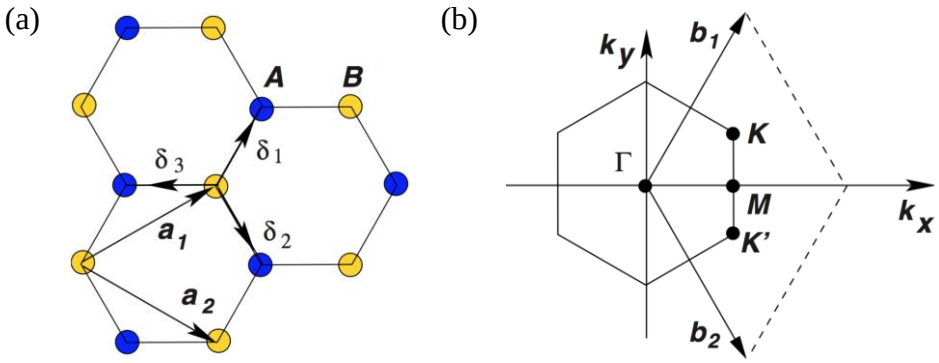


Figure 1-3 (a) Hexagonal crystal lattice of graphene. $a_1$ and $a_2$ are the lattice unit vectors and $\delta_i$, i=1,2,3 are the nearest-neighbor vectors. (b) The corresponding Brillouin zone and the Dirac cones are located at K and K' points [8].

### 1.2.1 Graphene Energy Band Structure

As mentioned previously, in graphene, carbon atoms are arranged in a hexagonal crystal lattice, where the structure can be understood as a triangular lattice with a basis of two atoms per unit cell, as shown in Figure 1-3(a). Each $sp^2$ hybridized carbon atom contains four valence electrons, where three of these electrons form carbon-carbon (C-C) σ bonds with their nearest neighbor atoms while the fourth one in the $2p_z$ orbital forms π bonds extending out of the graphene plane. Because the energy of σ electrons is far below

the Fermi energy, only the energy and interaction of π electrons make significant contributions to the electronic properties in the tight binding calculation. Detailed calculations are given in Wallace in 1947 [10] and McClure et al. in 1956 [11]. The energy band structure of graphene allows simple nearest neighbor tight binding approximation and give the derived energy dispersion relation:

$$\mathrm{E}(k_x, k_y) = \pm \mathrm{t}\sqrt{1 + 4 \cdot cos^2\left(\frac{k_x a}{2}\right) + 4 \cdot cos\left(\frac{k_x a}{2}\right) cos\left(\frac{k_y a\sqrt{3}}{2}\right)} \qquad (1\text{-}1)$$

where t is the interaction integral and $a$ is the lattice constant of graphene. Figure 1-4 shows the energy dispersion diagram based on Equation 1-1. Due to its two atoms basis, the points of particular importance are K and K' at the corners of hexagonal Brillouin zone, which are known as Dirac points shown in Figure 1-3(b). Near Dirac point, the energy band derived from the tight binding Hamiltonian shows linear dependence to the wave vector and the intersection near the edge of hexagonal Brillouin zone results in a conical energy dispersion, as shown in the zoom-in of Figure 1-4. Importantly, the energy bandgap of graphene is exactly zero, with conduction and valence band meeting at K and K' points, which are also known as charge neutrality points. Because of this linear dispersion relation, the quasiparticles in graphene behave very differently from those in other semiconductors with energy band structure approximated by parabolic dispersion relations. For instance, although the bandgap is zero in graphene, the gate voltage bias

can still modulate the density of states and switch from low conductivity states near the Dirac point to high conductivity states elsewhere [12]. Due to its gapless feature, there is still a finite amount of current flowing at low conductivity state near Dirac point leading to high switch-off current in graphene based transistors [8], [12], resulting in a non-negligible dark current in device operation. In addition, due to the symmetric conduction and valence band structure, the electrons behave exactly the same electronic properties as holes. More importantly, in the vicinity of the K and K' points, the energy dispersion within this Dirac cone region can be described as:

$$\mathrm{E(k)} = \pm \hbar v_F |k| \tag{1-2}$$

where $\hbar v_F$ is the Fermi velocity. This linear dispersive property leads to massless charge carriers, analogous to the relativistic massless carriers described by the Dirac theory.

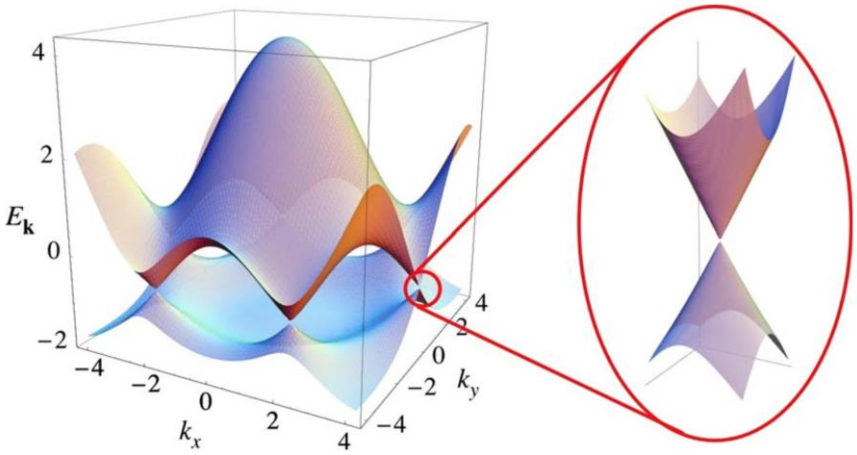


Figure 1-4 The three-dimensional (3D) energy dispersions of graphene crystal lattice. The conductance band touches at K and K' points [8].

### 1.2.2 High Carrier Mobility in Graphene

As mentioned previously, in graphene, each $sp^2$ hybridized carbon atom contains four valence electrons, where three of them form carbon-carbon (C-C) σ bonds with their nearest neighbor atoms while the fourth one in the $2p_z$ orbital forms π bonds extending out of the graphene plane. As the result, only one of the two allowable energy states in every un-bonding $2p_z$ orbitals is occupied while leaving another one empty, providing a pathway for electrons to hop/move carbon to carbon along the graphene surface without much limitation theoretically. Several literatures were reported that single layer graphene shows exceptional electronic quality as the charge carriers can travel ballistically over submicron distance and its mobility value reaches ~ 20,000 $cm^2/Vs$ [6], [7], [13]–[16]. Please note that these mobility value is limited by charged impurities scattering [17], [18] or microscopic ripples [19], [20], however, both scattering events can be reduced significantly by careful sample preparation and are not the ultimate limiting factors of carrier mobility in graphene. Instead, the intrinsic scatterers such as phonons, which cannot be removed at room temperature, should set the fundamental limit of carrier mobility [13], [14], [16]. Interestingly, Chen et al. [21] have experimentally shown the electron-acoustic phonon scattering contributes only ~ 30 Ω to graphene overall resistivity and proved the phonons' relatively weak contribution at room temperature.

Moreover, at carrier density of $1\times10^{12}$ $cm^{-2}$, they successfully reach the mean free path of over 2 μm and intrinsic mobility value of astonishing 200,000 $cm^2/Vs$.

### 1.2.3 Graphene Ambipolarity

Besides graphene's linear gapless energy band structure and extreme high carrier mobility, its transfer characteristics is also worthwhile discussing as it shows perfect ambipolar electric field effect so that its charge carriers parity can be tuned, unlike conventional CMOS technology, to be either n- or p-type by applying different gate biases, which is shown in Figure 1-5.

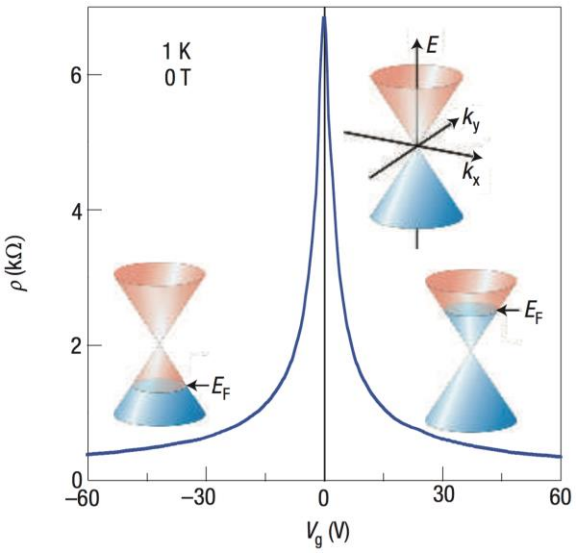


Figure 1-5 Ambipolar electric field effect in single layer graphene. The insets show its low energy spectrum, indicating changes in the position of the Fermi energy $E_F$ with respect to the varying gate biases [7].

Furthermore, graphene's low energy spectrum is also shown as insets in Figure 1-5, indicating the changes in the position of Fermi energy $E_F$ with respect to the varying gate biases. Interestingly, instead of doping materials to achieve different carrier parity in traditional silicon technology, by varying the gate biases, positive gate bias induces electrons while negative bias induces holes within the biased graphene region. Moreover, under suitable design/operation, the carrier concentration of electrons and holes can be reached as high as $10^{13}$ $cm^{-2}$ [7].

## 1.3 Graphene Unique Optical Properties

In this subchapter, I will discuss the optical properties of graphene which is utilized and applied to my studies in the thesis, including the optical conductivity (hyperbolic metamaterials HMMs), the photo-induced hot carriers (high responsivity photodetectors) and its transparency (light-field imaging).

### 1.3.1 Optical Conductivity in Graphene

Even though two-dimensional (2D) graphene can physically be considered as the reduction of three-dimensional (3D) bulk graphite layer numbers, they possess distinct properties and this reduced dimensionality requires different description for graphene's

important physical quantities. For instance, the refractive index is not well defined for two-dimensional (2D) graphene since there is no rigorous definition for the induced polarization per unit volume, instead, optical conductivity, which is associated with the surface current generated by light [22]–[24], should be a better physical quantity to describe its optical properties. The optical conductivity is a complex number, where the real part determines the loss while the imaginary part is closely related to several important optical phenomena. One explicit example is that whether graphene supports transverse-electric (TE) or transverse-magnetic (TM) plasmons depends on the sign of the imaginary part of the optical conductivity [25], and it also determines the behavior of a hyperbolic metamaterial consisting of truly 2D materials [26]. However, obtaining the imaginary part is not as straightforward as the real part. With this regard, Chang et al. [27] models graphene as an infinitely thin sheet with an in-plane surface conductivity, rather than a phenomenological effective refractive index. The complex optical conductivity is extracted by fitting the ellipsometric measurement of 2D materials on a known transparent substrate ($CaF_2$) over a broad spectral range from ultraviolet to mid-infrared. This approach allows connection to the theoretical predictions in which the optical conductivity is directly derived from the surface current induced in the 2D crystal by light [22]–[24]. Notably, the mid-infrared regime is particularly interesting since graphene has

been shown to be a good candidate material for mid-infrared plasmonics and metamaterials [28], [29].

In the model, the real and imaginary parts of the optical conductivity are the unknown parameters of interest. The Marquardt-Levenberg algorithm is applied to extract the optical conductivity $\sigma$ which minimizes the mean square error (MSE) between the measured data and the model-predicted values defined by:

$$\mathrm{MSE} = \sqrt{\frac{1}{3n-m}\sum_{i=1}^{n}[(N_i^{EXP} - N_i^{MOD})^2 + (C_i^{EXP} - C_i^{MOD})^2 + (S_i^{EXP} - S_i^{MOD})^2]} \times 1000 \qquad (1\text{-}3)$$

where n equals the number of wavelengths multiplied by the number of incidence angles; m is the number of fitting parameters; $N_i = \cos(2\Psi_i)$; $C_i = \sin(2\Psi_i)\cos\Delta_i$; $S_i = \sin(2\Psi_i)\sin\Delta_i$. The superscripts of EXP and MOD correspond to measured and model-predicted values, respectively. The subscript i indicates the particular set of data of a wavelength and an incident angle. The real and imaginary parts of the unknown optical conductivity as functions of wavelength are described by general smooth functions parameterized by cubic splines. The refractive index of the transparent substrate is described by the Sellmeier equation, whose coefficients are obtained from measurements of bare substrates.

Figure 1-6(a) shows the optical conductivity of monolayer CVD graphene extracted. The quality of the fit can be quantified by the MSE defined by Equation 1-3, indicating

good fitting quality. A value of the optical conductivity very close to the universal conductivity of graphene around 1 μm, moreover, the real part peak at 270 nm (with a photon energy of 4.6 eV) associated with the exciton-shifted van Hove singularity is observed.

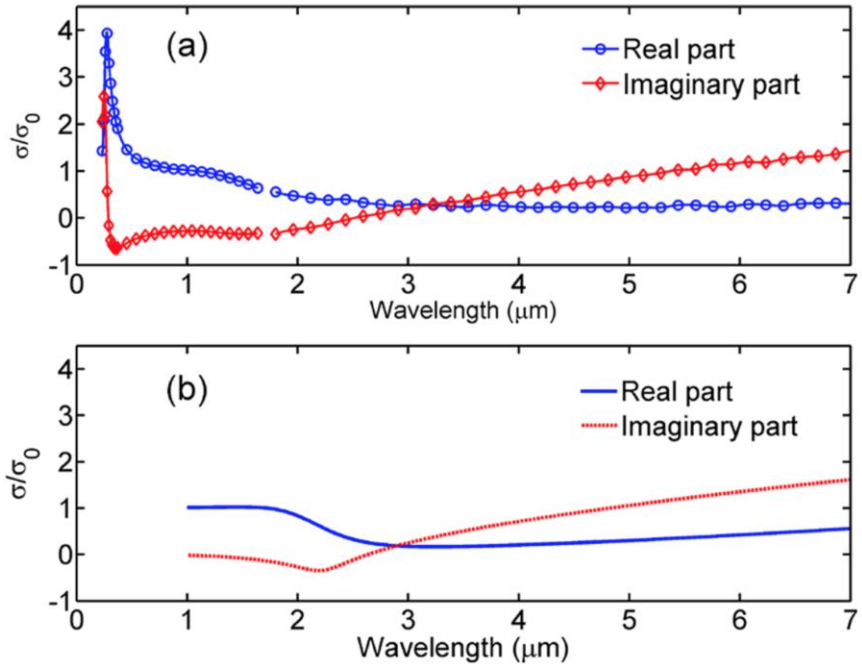


Figure 1-6 (a) The extracted optical conductivity of a monolayer CVD graphene sample. (b) The optical conductivity of monolayer graphene predicted by the non-interacting theory with a Fermi level of 277 meV and a scattering rate (in units of energy) of 54 meV. The optical conductivity is normalized to the universal conductivity. The circles and diamonds are the control points of the cubic splines.

The theoretical optical conductivity can be predicted by the non-interacting linear response theory [22]–[24]

$$\sigma(\omega) = \frac{\sigma_0}{2}\left(\tanh\frac{\hbar\omega+2\mu}{4k_BT} + \tanh\frac{\hbar\omega-2\mu}{4k_BT}\right) - i\frac{\sigma_0}{2\pi}\log\left[\frac{(\hbar\omega+2\mu)^2}{(\hbar\omega-2\mu)^2+(2k_BT)^2}\right] + i\frac{4\sigma_0}{\pi}\frac{\mu}{\hbar\omega+i\hbar\gamma} \quad (1\text{-}4)$$

where the first two terms and the third term are contributed by the inter-band and intra-band transitions respectively. $\sigma_0$ is the universal conductivity defined by $e^2/4\hbar$; $\mu$ is the Fermi level; $\gamma$ is the intra-band scattering rate. Figure 1-6(b) is plotted with a Fermi level of 277 meV and a $\hbar\gamma$ value of 54 meV. The measured conductivity shows a smoother feature around 2 μm than the theoretical curves, which is resulting from the non-uniform distribution of the Fermi level and scattering rate within measuring spot. Moreover, the broadening is also attributed by the damping in the inter-band transition, which is not considered in the theoretical conductivity described by Equation 1-4.

This technique can also be applied to study how chemical doping modifies the optical conductivity in graphene. Figure 1-7 shows the optical conductivity of monolayer graphene before and after chemical doping by nitric acid vapor [30]. According to the theoretical conductivity described by Equation 1-4, the Fermi level can be identified by the local minimum of the imaginary part [31]. As the result, the nitric acid chemical doping pushes the Fermi level to 530 meV (relative to the Dirac point), as the imaginary part local minimum at the wavelength of 1.16 μm corresponds to a photon energy of twice the Fermi level. Meanwhile, the real part in the near-infrared region is decreased by Pauli blocking and the optical conductivity at wavelengths below 0.6 μm shows

negligible changes.

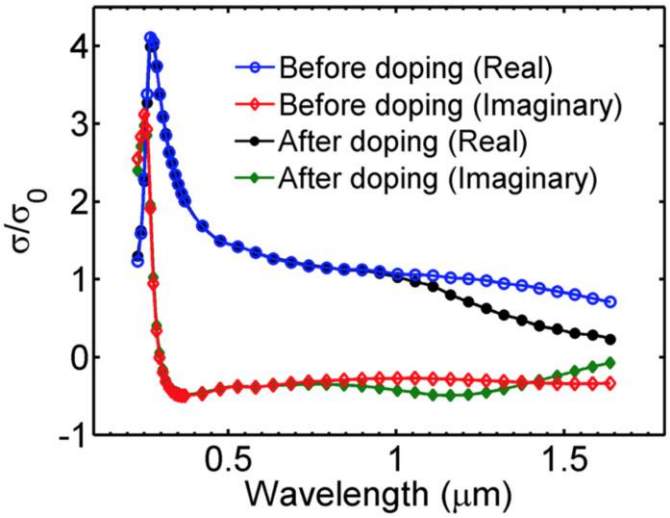


Figure 1-7 The extracted optical conductivity of a monolayer CVD graphene sample before and after chemical doping by nitric acid vapor. The optical conductivity is normalized to the universal conductivity. The markers are the control points of the cubic splines.

Here, a method for analysis of spectroscopic ellipsometry data is demonstrated to extract the complex optical conductivity in graphene. As two-dimensional (2D) materials gradually become building blocks for more complicated structures and create optical functionalities, people can expect this simple and robust technique will become crucial and increasingly important for further advance in optoelectronic and metamaterial applications [26], [32]–[35], which will be addressed in the following chapters.

### 1.3.2 Photo-Induced Hot Carriers in Graphene

Electrons in semiconductors can be excited into higher energy states by absorbing photons and generating so-called hot carriers. Efficiently converting these energies of hot carriers into electric energy with minimum losses is highly desirable for various optoelectronic applications. However, in most conventional semiconductors, excited hot carriers rapidly relax to the band edge within picoseconds via electron-phonon scattering, dissipating energies as heats to excite phonons instead of being exploited, thus significantly limit the efficiency. Theoretically, the maximum efficiency of a single-junction device is only 31 %, which is known as Shockley-Queisser limit and primarily caused by phonon losses [36]. To overcome this single-junction theoretical limit, ideas utilizing hot carriers to enhance the power conversion efficiency have been proposed, aiming to suppress the energy relaxation of hot carriers to phonons. Successful suppression has been observed in several semiconductor nanocrystals because their energy relaxation pathways can be greatly altered by quantum confinement effects [37]–[40]. Specifically, graphene, as a semi-metallic nanomaterial, is expected its massless linear energy band structure can lead to unique hot carrier photoresponses compared with conventional parabolic-like energy band semiconductors.

Studies have demonstrated that hot carriers in graphene can be thermally decoupled

from the lattice temperature even under weak illumination due to its relatively high optical phonon energy (~ 196 meV near the zone center [41]–[43], as shown in Figure 1-8), which can only relax high energy carriers rapidly. Once the carriers cool below the optical phonon energy, they must scatter with multiple acoustic phonons to reach equilibrium, where this process is inefficient and slows down the hot carrier cooling.

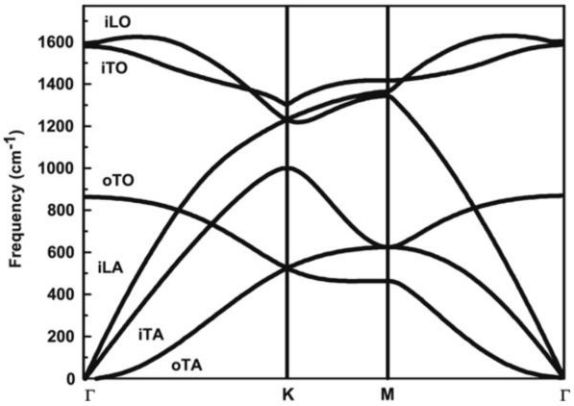


Figure 1-8 Calculated phonon dispersion relation of graphene showing the iLO, iTO, oTO, iLA, iTA and oTA phonon branches. [41].

Among diverse measurement techniques, ultrafast optical pump-probe spectroscopy has been widely used to resolve the dynamics of photo-induced hot carriers [44]–[46]. The pump-probe measurements have indicated that efficient carrier-carrier scattering in graphene results in rapid thermalization of hot carriers immediately after excitation. Hot carriers are easily heated to a few thousand Kelvin due to graphene's low electronic heat

capacity, then in the next few hundreds of femtoseconds, they lose energies to optical phonons and reach thermal equilibrium with the strongly coupled optical phonon temperature. Thus, the cooling rate of optical phonons then becomes the main bottleneck to subsequent hot carrier cooling.

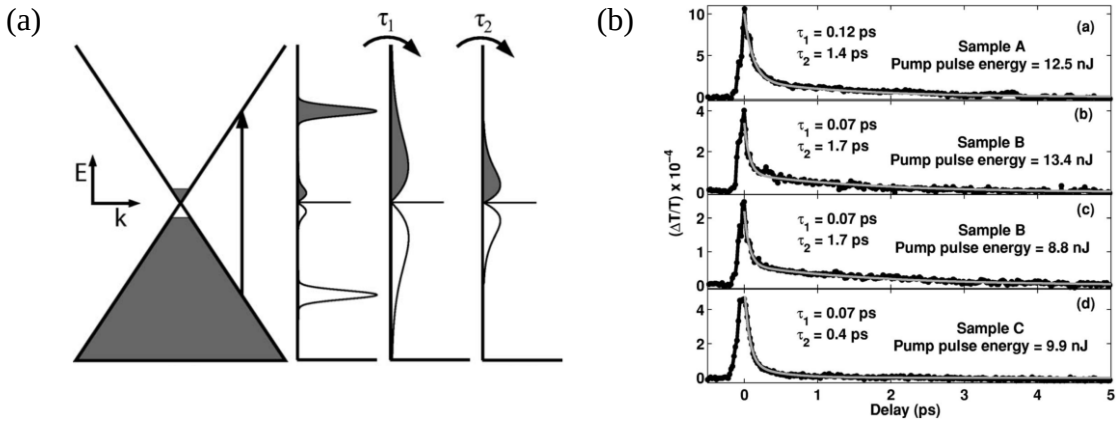


Figure 1-9 Dynamics of hot carrier cooling in graphene. (a) Photoexcited hot carriers thermalize within the timescale $\tau_1$, and the subsequent cooling via optical phonon emissions occurs on a timescale $\tau_2$. (b) Experimental results of the pump-probe measurements. The curves provide information about the thermalization timescale ($\tau_1$) and relaxation timescale ($\tau_2$) [44].

Figure 1-9 presents the results of a typical pump-probe measurement and the curve represents the transmission of the differential probe [44]. By tuning the pump-probe time delay, we observe the decay of the curve because the transmission of the probe beam is sensitive to the hot carrier population induced by the pump beam. From the measurements, it is clear that each curve exhibits two distinct time scales. The initial fast

decay within the first 70-120 femtoseconds range ($\tau_1$) represents the rapid hot carrier thermalization processes in graphene, and the slower relaxation time within the 1-2 picoseconds range ($\tau_2$) is determined by the optical phonon scattering rate.

As mentioned previous, when the hot carrier energy is below the optical phonon energy, carrier cooling will be dominated by acoustic phonons emission. Ideally, the small Fermi surface and momentum conservation severely constrain the pathway of carrier relaxation as shown in Figure 1-10 (Left), rendering the carrier cooling inefficient. However, experiments with the optical pump-terahertz probe measurement show much slower decay (> 60 ps) and is the direct evidence of inefficient cooling by acoustic phonons [47]. The hot carrier relaxation time remains 1-2 orders of magnitude faster than the theoretical predictions (~ ns) [48], which suggests that other mechanisms in addition to acoustic phonon emissions may also play an important role in assisting carrier cooling. To clarify this issue, the concept of disorder-assisted scattering (also called supercollision cooling) was proposed and experimentally confirmed by photocurrent and Johnson noise thermometry measurements [49]–[51], where the impurities could provide alternative pathways for hot carrier cooling as shown in Figure 1-10 (Right). Therefore, scattering via these impurities will not be constrained by the small Fermi surface in graphene because the impurities can provide large momentum space and energy, that is, faster

energy relaxation would be observed in disordered graphene than in disorder-free graphene.

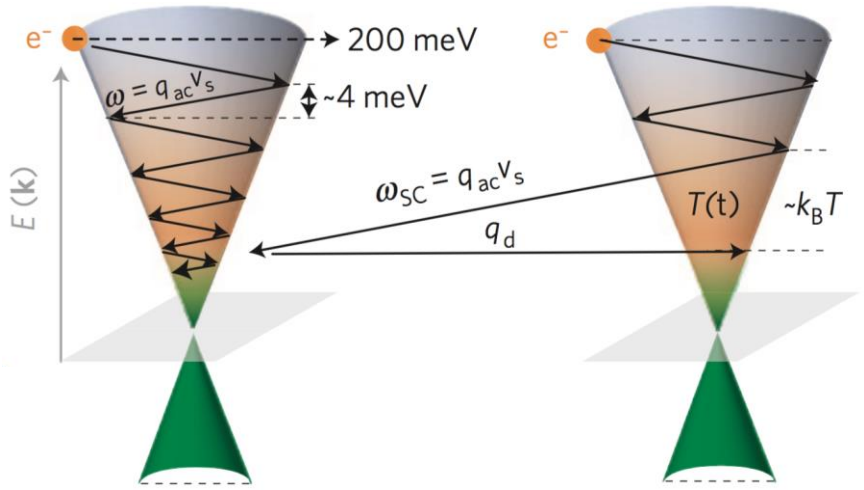


Figure 1-10 (Left) Hot carrier relaxation in pristine graphene while each relaxation step is restricted by momentum and energy conservation, resulting in slow hot carrier cooling. (Right) Hot carrier relaxation in disorder-graphene while the disorder relaxes momentum conservation and leads to faster hot carrier cooling [49].

Besides the cooling pathway of photo-induced hot carriers, radiative recombination of electron-hole pairs can result in light emission, which is known as photoluminescence (PL). In conventional semiconductors, its spectral emission is generally below the excitation photon energy, with the highest intensity near the semiconductor bandgap. The blue-shift of photoluminescence can be observed in a few bulk semiconductors, demonstrating intra-band carrier-carrier scattering, as shown in Figure 1-11(a). However,

the parabolic energy band structure limits the momentum exchange, hence the range of blue-shifted photoluminescence usually appears in a relatively narrow frequency range. In contrast, graphene inherits a linear energy band structure and strong carrier-carrier scattering, under femtosecond pulse illumination, excited hot carriers can efficiently exchange momentum and energy, which elevates carriers into higher energy states, as shown in Figure 1-11(b). By exciting graphene with the 1.5 eV pulse laser, a broadband photoluminescence as high as 3.1 eV can be measured, as shown in Figure 1-11(c). The results agree with Planck's law, indicating that hot carriers in graphene would rapidly thermalize after excitation [52], [53].

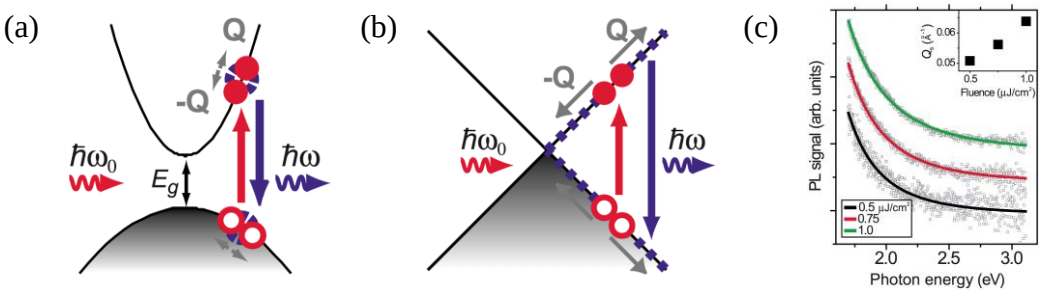


Figure 1-11 Nonlinear photoluminescence in graphene. (a) Inefficient carrier-carrier scattering in the parabolic band. (b) Efficient carrier-carrier scattering in the linear band. (c) The photoluminescence measured from graphene under 1.5 eV pulse excitation [52].

Instead of electron-phonon scattering, studies have exploited optical pump-terahertz probe techniques and further clarified that electron-electron scattering would be very

efficient in highly doped graphene during the initial stage of hot carrier cooling. Therefore, carrier multiplication can be observed in doped graphene after pulse laser excitation [54]. As shown in Figure 1-12, a photoexcited hot carrier triggers a cascade of intra-band electron-electron scattering processes, where energy and momentum are transferred to electrons in the Fermi sea, producing multiple secondary hot carriers in the conduction band. The efficiency of carrier multiplication depends not only on the graphene doping level but also on the excitation photon energy.

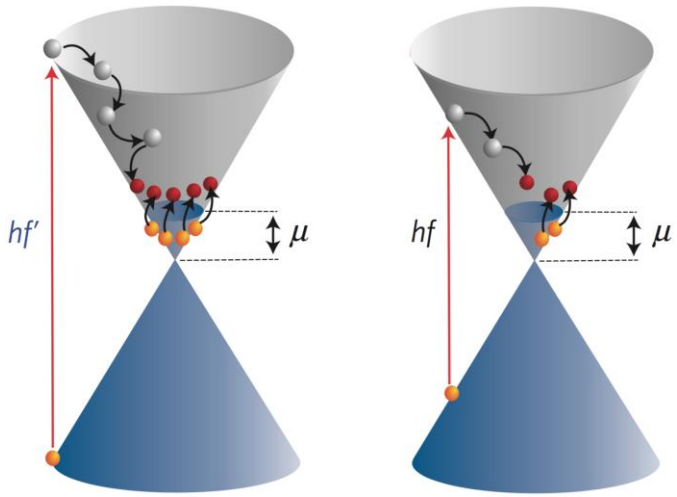


Figure 1-12 The hot carrier created by absorbing (a) a high energy photon and (b) a low energy photon will relax its energy to the electrons in the Fermi sea, which creates multiple hot electrons in the conduction band [54].

Understanding the dynamics of hot carriers is not only of fundamental interest but also essential for developing novel hot carrier optoelectronics. With the discussion and

observations of its energy relaxation pathways, graphene suggests and serves as a promising photo-active material candidate, motivating us to perform further explorations.

### 1.3.3 High Transparency of Graphene

Graphene also provides interesting optical property in its transparency. Studies show that the absorption of suspended graphene is defined solely by the fine structure constant, $\alpha = e^2/\hbar c \approx 1/137$, the parameter that describes coupling between light and relativistic electrons and that is traditionally associated with quantum electrodynamics rather than materials science. Despite being atomically thick, graphene is found to absorb a significant fraction of incident white light, a consequence of graphene's unique electronic structure. The universal conductance [55] implies that observable quantities such as graphene's optical transmittance are also universal and given by (for the normal light incidence)

$$T \equiv (1 + 2\pi G/c)^{-2} = (1 + \pi\alpha/2)^{-2} \approx 1 - \pi\alpha \tag{1-5}$$

where the equation yields graphene's absorption $(1 - T) \approx \pi\alpha = 2.3\ \%$. The origin of the optical properties being defined by the fundamental constants lies in the two-dimensional nature and gapless electronic spectrum of graphene and does not directly involve the chirality of its charge carriers.

Figure 1-13(a) shows the image of graphene sample in transmitted white light. An aperture is partially covered by suspended graphene so that opacities of different areas can be compared. The line scan across the image qualitatively illustrates changes in the observed light intensity. Further measurements yield graphene's absorption of $2.3 \pm 0.1$ %, whereas optical spectroscopy shows that the opacity is practically independent of wavelength, as shown in Figure 1-13(b). Moreover, the absorption is found to increase with number of layers so that each graphene layer contributes another 2.3 % absorption, as shown in Figure 1-13(b) inset. Notably, their result also suggests the universal/flat absorption spectrum over a wide range of frequencies, whereas the behavior is expected for massless ideal Dirac fermions.

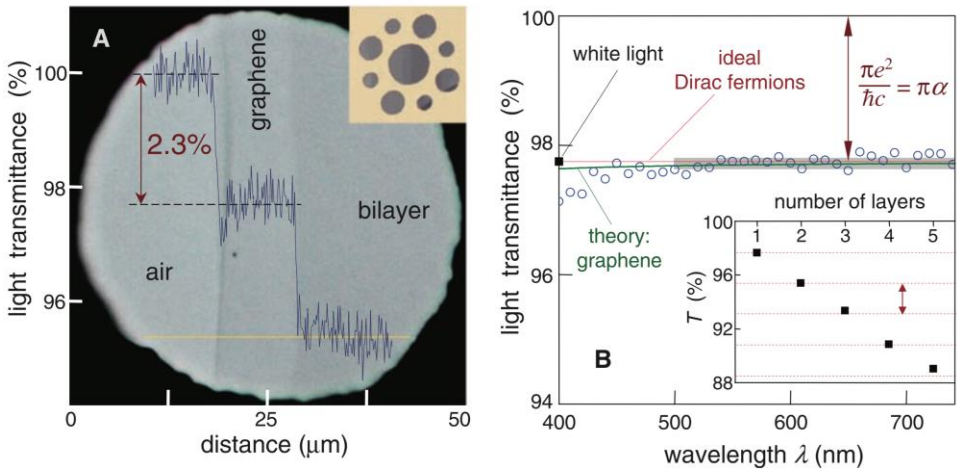


Figure 1-13 (a) Photograph of a 50 μm aperture partially covered by graphene and its bilayer. The line scan profile shows the intensity of transmitted white light along the yellow line. The inset is a 20-μm-thick metal support structure with apertures of 20, 30, and 50 μm in diameter with graphene placed over them. (b) Transmittance spectrum of single layer graphene (open circles). Slightly lower transmittance for $\lambda < 500$ nm is probably due to hydrocarbon contamination. The red line is the transmittance $T = (1 + 0.5\pi\alpha)^{-2}$ expected for two-dimensional Dirac fermions, whereas the green curve takes into account a nonlinearity and triangular warping of graphene's electronic spectrum. The gray area indicates the standard error for our measurements. The inset shoes the transmittance of white light as a function of the number of graphene layers (squares). The dashed lines correspond to an intensity reduction by πα with each added layer [56].

## 1.4 Graphene Synthesis

As mentioned previously, graphene is being first introduced in 2004 by mechanical exfoliation, in which the adhesive tape is utilized to repeatedly spit graphite crystals into thinner flakes and eventually produce monolayer graphene. This method can offer the highest quality graphene since it is directly obtained from crystalline graphite, however, it is very challenging to control the flake thickness, size and location, which is impractical

and limits its industrial large-scale applications. In this regard, several synthesis approaches are in need of development and have been explored [57]–[63].

One of the successful synthesis methods is epitaxial growth, which converts silicon carbide (0001) into graphene via the sublimation of silicon atoms under high growth temperature (~ 1500 °C) and ultra-high vacuum. Instead of mechanical exfoliation, this epitaxial approach can produce wafer scale graphene for potential industrial applications, however, this method requires precise control of the growth conditions and the SiC substrates are relatively high cost. Moreover, epitaxial growth method can only offer graphene on specific substrates, which also limits its application possibilities.

People then pay their attention to the chemical vapor deposition (CVD) synthesis method [64]–[67], where graphene is synthesized by injecting hydrocarbons (in a form of methane gas) with hydrogen ($H_2$) in furnace (~ 1000 °C) to interact with transition metals, such as nickel (Ni), copper (Cu), ruthenium (Ru) and iridium (Ir). The growth mechanism varies with the choice of different transition metals, among of all, CVD graphene synthesis on copper foil is highly attractive due to its capability of producing large scale and uniform polycrystalline films, which can easily achieve more than 95% coverage and its size is only limited by the synthesis apparatus [68]. In addition, with proper synthesis, high quality graphene with mobility up to 7000 $cm^2V^{-1}s^{-1}$ is also achieved and

demonstrated. Moreover, CVD graphene synthesis on copper is relatively inexpensive and readily compatible/accessible with the development of transfer techniques to obtain high quality graphene on any arbitrary substrates. With all these advantages, even it still exhibits several considerable imperfections such as domain sizes, wrinkles and defects, which limit its device performance to some extent [69]–[72], the CVD graphene on copper is undoubtedly one of the most widely used synthesis methods for electronic and optoelectronic application/research nowadays.

The CVD graphene synthesis/growth mechanism on copper can be understood and is shown step-by-step in Figure 1-14 [73], [74]. Initially, hydrogen catalyzes the metal surfaces and leads the grain growth in transition metals. Then, carbon atoms start to nucleate into several small graphene flakes and grows larger along preferential crystallographic directions. The formation of graphene is the consequence of diffusion and segregation of carbon atoms during the annealing and cooling stages. Eventually, these flakes coalesce into a continuous film as the growth time increases and is properly controlled. All in all, this method involves thermal decomposition of hydrocarbons (in a form of methane gas) on the surface of transition metal and then carbon was segregated from the surface upon cooling down, forming two-dimensional monolayer graphene along the copper surface.

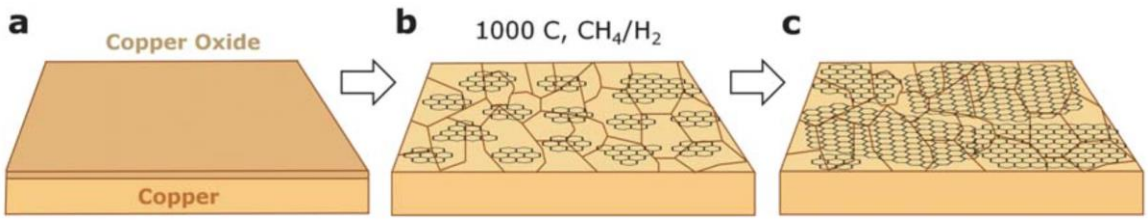


Figure 1-14 The growth mechanism of graphene on Cu. (a) Annealing of a Cu foil with native oxide in $H_2$ (b) Nucleation of graphene islands. (c) Coalescing of graphene flakes into a film [73].

Here at the University of Michigan, our lab (Nanoelectronics and Nanophotonics Lab, https://wwweb.eecs.umich.edu/zhonglab/) runs a commercial CVD system (FirstNano EasyTube 3000) with the capability to flow required gases methane at controlled temperature and vacuum level for not only single but also bilayer graphene growth, offering and supporting the flexibility and diversity for various related research studies.

## 1.5 Thesis Overview

This thesis focuses on exploiting graphene's unique properties with novel nanostructure and transistor design for both electrical and optical applications. It is organized as following: Chapter 1 introduces graphene in different aspects, including discovery, physical geometry, electrical and optical properties, as well as its synthesis methods; Chapter 2 proposes the dual-gate graphene ambipolar transistor design that can

operate as either common mode or differential mode amplifier, meanwhile, achieve high noise rejection amplification; Chapter 3 demonstrates the hyperbolic metamaterials (HMMs) by using precisely controlled periodic graphene-dielectric multilayer nanostructures in mid-infrared regimes; Chapter 4 reviews the photo-gating effect resulting from well-designed graphene heterojunction nanostructure for ultra-broadband and high responsivity photodetectors; Chapter 5 proposes the graphene-SOI heterojunction photodetector design to improve device on-off operation speed as well as strengthen photo-gating effect, moreover, fabricates single pixels into matrix arrangement to achieve image array readout; Chapter 6 demonstrates all-graphene transparent heterojunction photodetectors for light-field imaging; Chapter 7 concludes the thesis and propose ideas for further studies.

# Chapter 2

# Graphene Ambipolar Nanoelectronics for High Noise Rejection Amplification

## 2.1 Introduction

With over half of the world's population having access to cellular phones and other mobile/wearable information devices, there is a definite movement towards the realization of ubiquitously available wireless communication system that are even more compact and portable. Among the modern wireless communication system, signal amplification is one of the key processes and critical for overcoming losses during multiple data transformations/processes and long-distance transmission. There are four basic types of electronic amplifiers: voltage, current, transconductance, and transresistance amplifiers [75]. Generally, the voltage amplifier is the most common one and widely used in modern circuit architecture. More specifically, there are two main and fundamental amplification mechanisms for voltage amplifiers, i.e. common and differential mode amplifications respectively [76]. Common mode is basically the most

generic concept of amplification, which amplifies particular input voltage, while the differential mode amplifies the voltage difference between two input signals. Both the common and differential mode amplifiers are crucial and widely used in the circuitry nowadays, however, they utilize two totally different circuit configurations.

During the past decade, graphene has been widely studied and shown extremely high intrinsic carrier mobility at room temperature [14], [16], [21], linear dispersion relation in energy band structure, and ambipolar behavior for both electron- and hole-dominated regions [6], [15], [77]. In particular, the intriguing ambipolarity of graphene has enabled unique RF device applications [78], [79] which not only provide greater controllability for signal processing and modulation, but with much simplified circuitry. Recent advances in graphene integrated electronics have led to notable progress: a number of RF integrated circuits with various functionality have been successfully demonstrated including mixer [80]–[83], frequency doubler [84], [85], tripler [86], multiplier [87], [88], antenna [89]–[91] and receiver [92]. Moreover, researchers also achieved circuit logic operation [93], invertor [94]–[96], modulator [97], [98] and electromechanical devices, such as resonators [99], [100] and switch [101]. Flexible and transparent graphene-based device and circuit were also demonstrated [64], [97], [102], [103], which further showcase the possibilities of graphene for novel nanoelectronic applications.

We report an extremely simple device design which can be programed to achieve the functionality of both common and differential mode amplifications. To implement the idea, we designed and fabricated a new type of dual-gate graphene ambipolar device, where the phase of the RF signal can be modulated independently at two gates to be either in phase or out of phase. This unusual tunability is enabled by the unique ambipolarity of graphene, and leads to both common mode and differential mode operations in a single device. In addition, these devices can achieve a common-mode rejection ratio (CMRR) as high as 80dB, making it relevant for low noise circuit applications.

## 2.2 The Dual-Gate Graphene Ambipolar Device

To fabricate the device, a pristine single layer graphene film is first synthesized by chemical vapor deposition (CVD) method on copper foil. One side of the copper sample is coated with 950 PMMA A2 (MicroChem) photoresist as protection layer and the other side is exposed to oxygen plasma to etch away the undesired graphene. The sample is left in ammonium persulfate solution (0.023 g/ml) to dissolve away the copper layer underneath, and then the graphene film with PMMA coating is cleaned and transferred onto prepared intrinsic silicon wafer with 300 nm thermal $SiO_2$ on top. After removing

the PMMA coating by rinsing with acetone and isopropyl alcohol, the single layer graphene is then patterned into the desired transistor channel (W/L = 50 μm/20 μm) by conventional photolithography and oxygen plasma etching. After graphene patterning, Cr/Au (5 nm/50 nm) source and drain metal contacts are deposited by e-beam evaporation and photolithography lift-off processes, leaving 7 μm length and 50 μm width graphene film in between as device channel. Then 2 nm aluminum layer is e-beam evaporated onto the sample, followed by 12 hours oxidation in air and additional 13.5 nm $Al_2O_3$ deposited by atomic layer deposition (ALD) at 250 °C. The total thickness of $Al_2O_3$ is 16.1 nm, which is used as our top gate dielectric layer. Lastly, two 2 μm wide Cr/Au (5 nm/50 nm) top gate metal strips with 1 μm spacing are electrostatically coupled and deposited by e-beam evaporation and photolithography lift-off processes, providing modulation to the RF signal.

Figure 2-1(a) shows the schematic of dual-gate graphene ambipolar device structure and the scanning electron microscope (SEM) image of the actual fabricated device is shown in Figure 2-1(b). During a typical operation, drain-source is DC biased with a supplied voltage, and two gates are DC biased at the desired biasing points. AC input is supplied through two gates via bias tees, and the output signal is recorded at the drain with a AC lock-in amplifier and oscilloscope.

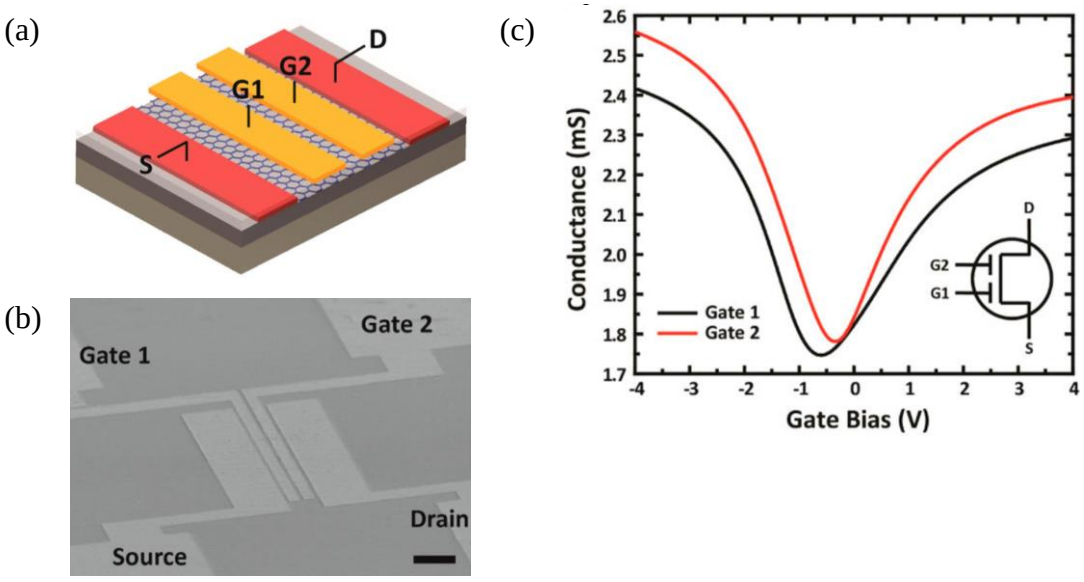


Figure 2-1 Device geometry of dual-gate graphene ambipolar device and its I-V characterization. (a) Schematic of the device. Source (S) and drain (D) electrodes are shown in red, and the dual-gate electrodes (G1 and G2) are shown in yellow. (b) The SEM image of the fabricated device. Scale bar, 10 μm. (c) The conductance versus gate voltage response curves for gate 1 (black) and gate 2 (red). The inset illustrates the proposed equivalent circuit symbol of our dual-gate graphene ambipolar device.

The conductance-gate voltage transfer curves for two independent gates are shown in Figure 2-1(c), where the ambipolarity is clearly presented with Dirac points at -0.6 V and -0.34 V for gate 1 and 2 respectively. To further investigate the transistor properties, the contact resistance and the carrier mobility can be extracted by fitting the experimental resistance value across the source and drain with the following equation [97], [104],

$$R_{total} = \frac{V_{ds}}{I_{ds}} = R_{contact} + \frac{L}{q\mu W \cdot \sqrt{n_0^2 + (\frac{C_{ox}(V_g - V_{Dirac})}{q})^2}} \quad (2\text{-}1)$$

where the variables are defined as drain-to-source voltage $V_{ds}$, drain-to-source current $I_{ds}$,

contact resistance $R_{contact}$, channel length $L$ and width $W$, mobility $\mu$, residual carrier concentration $n_0$, gate capacitance $C_{ox}$, the gate bias voltage $V_g$, and the charge neutrality point $V_{Dirac}$. The device presented in Figure 2-1(c) yield a hole mobility of 844 $cm^2V^{-1}s^{-1}$ and electron mobility of 866 $cm^2V^{-1}s^{-1}$ with $n_0$ of $1.57\times10^{12}$ $cm^{-2}$ and $R_{contact}$ of 378 Ω.

Both gate 1 and 2 offer electrostatic control of electron-dominated versus hole-dominated transport within graphene channel, as shown in Figure 2-2. We propose a new equivalent circuit symbol, shown in Figure 2-1(c) inset, for our ambipolar device to represent in dual gate tuning.

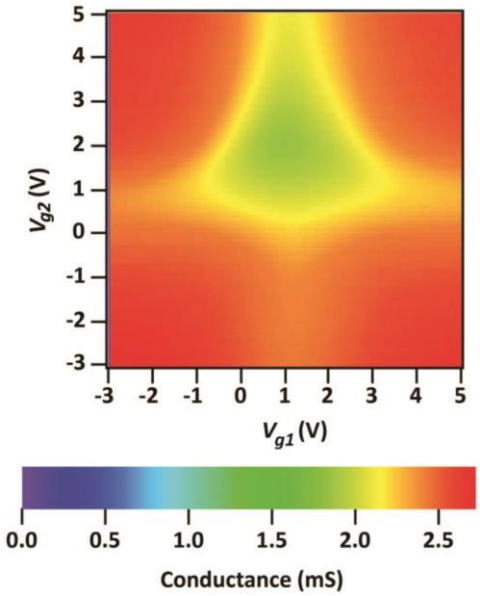


Figure 2-2 The two-dimensional (2D) color plot of conductance versus gate biasing voltages for dual-gate graphene ambipolar device. The graphene channel can be operated under p-p (lower left), n-n (upper right), p-n (upper left), and n-p (lower right) regions by biasing two gate accordingly.

## 2.3 The Amplification Mechanism for Multi-Mode Operation

We examine how independent modulation by the two gates can be configured to achieve common and differential mode operations. The key principle lies in the ambipolarity of graphene: the phase of an AC input can be shifted by 180 degree when switching the DC gate biasing point from electron-dominated region to hole-dominated region, and vice versa [97].

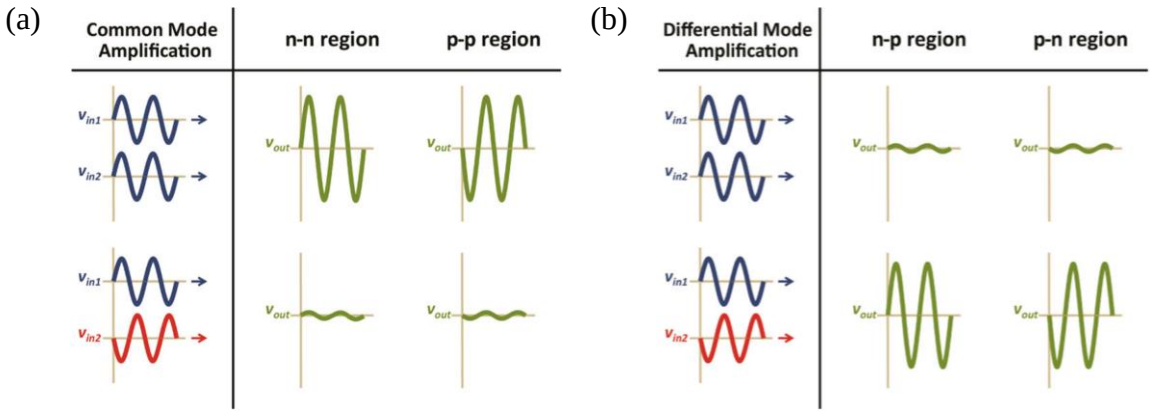


Figure 2-3 The operation mechanism of dual-gate graphene ambipolar device. (a) Schematic showing the common mode operation mechanism. Two AC inputs ($v_{in1}$ and $v_{in2}$) are supplied through two gates, and the output signal ($v_{out}$) is recorded at the drain of the device with source grounded. (b) Schematic showing the differential mode operation mechanism.

To achieve common mode operation, one can configure the phase modulation of gate 1 and 2 to be in phase by DC biasing two gates in the same electron- (or hole-) dominated region, as shown in Figure 2-3(a). In the schematic, two in-phase input signals

are amplified with the same phase, which lead to two in-phase outputs and add up to a significant overall output signal. On the other hand, two out-of-phase input signals yield two out-of-phase outputs, which cancel each other and lead to a negligible overall output signal. As the result, the dual-gate graphene ambipolar device is functioning as a common-mode amplifier.

For differential more operation, one can configure the phase modulation of gate 1 and 2 to be out of phase (n-p or p-n region) by DC biasing one gate in electron-dominated region, and the other gate in hole-dominated region, as shown in Figure 2-3(b). Contrary to the common mode operation, two out-of-phase input signals are amplified with opposite phase, which lead to two in-phase outputs and add up to a larger overall output signal. On the other hand, two in-phase input signals yield two out-of-phase outputs, which cancel each other and lead to a negligible overall output signal. As the result, the dual-gate graphene ambipolar device is configured as a differential mode amplifier by simply changing the gate biasing conditions. We note that one can also operate one of the gates at the charge-neutral Dirac point, and the device will become a typical graphene transistor.

### 2.3.1 Common Mode Amplification Operation

To experimentally verify the common mode operation, we test our dual-gate graphene ambipolar device with two in-phase AC inputs. Figure 2-4(a) shows the electrical measurement setup. Here, we use the built-in sinusoidal wave generated from the lock-in amplifier (Stanford Research Systems SR830) as our AC source ($v_{ac}$ = 10 mV, $f$ = 100 kHz), which is coupled into two gates through bias tees for the two AC inputs. The output signal is measured at the drain using the lock-in amplifier with source grounded. Four different gate biasing conditions are tested, which are n-n ($V_{g1}$ = 3.5 V, $V_{g2}$ = 2.8 V), p-p ($V_{g1}$ = 0.2 V, $V_{g2}$ = -0.3 V), p-n ($V_{g1}$ = -2.5 V, $V_{g2}$ = 2.8 V), and n-p ($V_{g1}$ = 3.6 V, $V_{g2}$ = -2.3 V) regions. Figure 2-4(b) shows real-time output signal waveform under these four gate biasing conditions, together with the input waveform. When two gates are biased in the same electron-dominated (n-n) or hole-dominated (p-p) region, we recover the sinusoidal waveform at the output. On the contrary, when two gates are biased in p-n or n-p region, the output signal amplitude is negligible. These results confirm the common mode operation mechanism illustrated in Figure 2-3(a). Furthermore, in order to present the complete picture of how dual-gate graphene ambipolar device response to two in-phase inputs, we measure the output signal amplitude when sweeping both gates across the Dirac point, as shown in Figure 2-4(c).

The output signals in n-n and p-p regions are significantly larger than the signals in p-n and n-p regions. The maximum achievable common mode gain is larger than unity under corresponding gate biasing point in n-n region. We note that the slight difference in n-n and p-p regions is caused by the asymmetry of electron and hole transport.

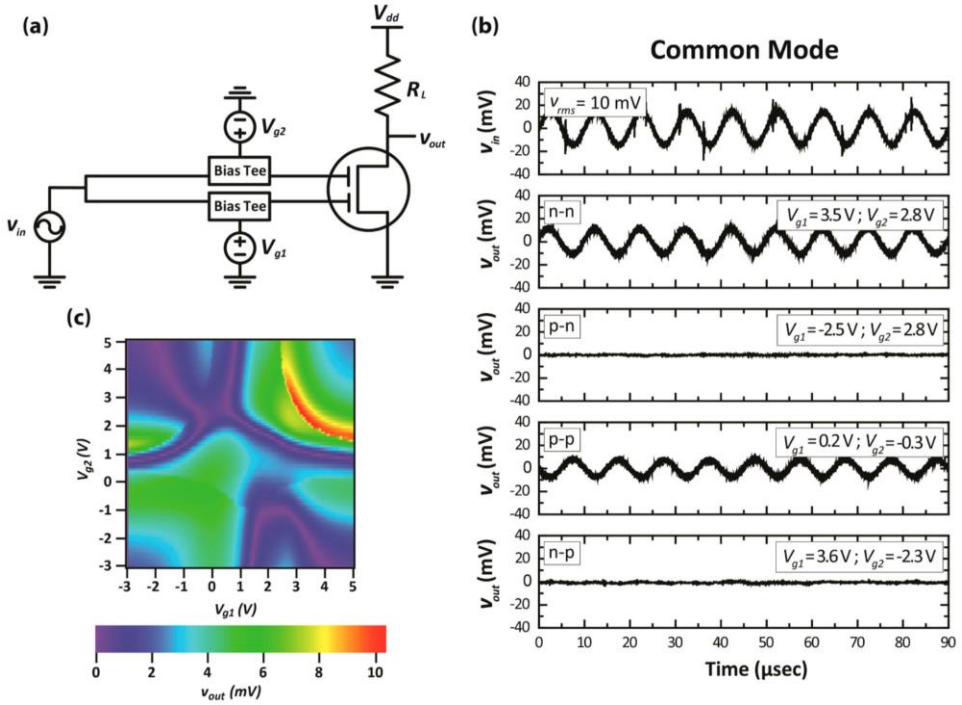


Figure 2-4 The common mode operation demonstrated by the dual-gate graphene ambipolar device. (a) Diagram of the electrical measurement setup. $R_L$ = 0.5 kohm and $V_{dd}$ = 10 V. (b) The time-traced AC voltage amplitude curves recorded for input and the outputs under n-n, p-n, p-p, and n-p dual-gate biasing conditions. (c) Two-dimensional color plot of output voltage amplitude versus the dual-gate biasing voltages. In-phase AC inputs ($v_{in}$ = 10 mV) are supplied at two gates during the measurement for common mode operation.

### 2.3.2 Differential Mode Amplification Operation

We also examine the differential mode operation by testing the same dual-gate graphene ambipolar device with two out-of-phase inputs. Here, we use a custom-built phase shift circuit, as shown in Figure 2-5, in one of the gates in order to achieve 180 degrees phase difference between two inputs.

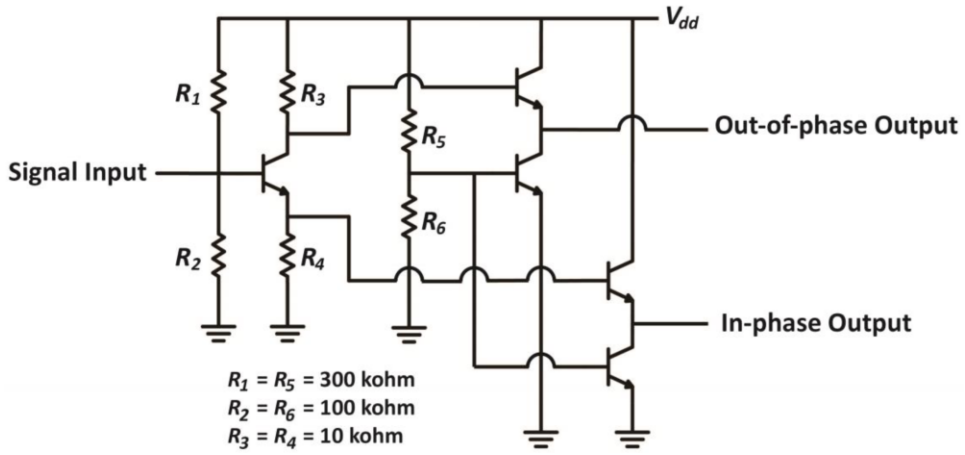


Figure 2-5 The circuit diagram of the custom-built phase shift module with 2N3904 NPN BJTs.

Figure 2-6(a) shows the electrical measurement setup for different mode amplification operation. We again tested four different gate biasing conditions, which are n-n ($V_{g1}$ = 2.5 V, $V_{g2}$ = 3.4 V), p-n ($V_{g1}$ = -0.8 V, $V_{g2}$ = 3.2 V), p-p ($V_{g1}$ = -0.5 V, $V_{g2}$ = -0.3 V), and n-p ($V_{g1}$ = 2.4 V, $V_{g2}$ = 0.5 V). As shown in Figure 2-6(b), we recover a strong sinusoidal waveform at the output when two gates are biased in p-n or n-p regions.

On the contrary, when two gates are biased in n-n or p-p region, the output signal amplitude is negligible. These results contrast the common mode operation shown earlier, and confirm the differential mode operation mechanism illustrated in Figure 2-3(b).

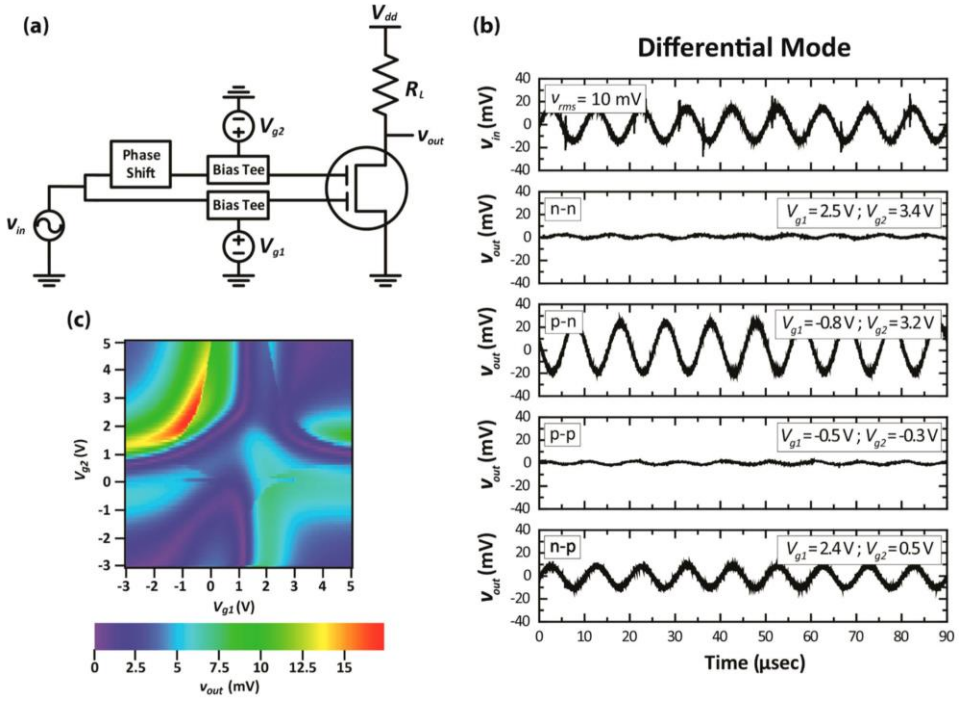


Figure 2-6 The differential mode operation demonstrated by the dual-gate graphene ambipolar device. (a) Diagram of the electrical measurement setup. $R_L$ = 0.5 kohm and $V_{dd}$ = 10 V. A phase shift circuit is used in one of the gates in order to achieve 180 degrees phase difference between two inputs. (b) The time-traced AC voltage amplitude curves recorded for input and outputs under n-n, p-n, p-p, and n-p dual-gate biasing conditions. (c) Two-dimensional color plot of output voltage amplitude versus the dual-gate biasing voltages. Out-of-phase AC inputs ($v_{in}$ = 10 mV) are supplied at two gates during the measurement for differential mode operation.

A more complete picture is shown in Figure 2-6(c), where the output signal amplitude is again plotted against two gate biasing voltages. Noticeably, large output signal regions are located in n-p or p-n regions, which is the exact opposite of the common mode operation scenario shown in Figure 2-4(c). Furthermore, a voltage gain higher than 1.7 is obtained under differential mode operation.

## 2.4 The Common Mode Rejection Ratio (CMRR)

With the results from both common and differential mode operations, we can further calculate the common mode rejection ratio (CMRR) given by:

$$CMRR = 20 \cdot log_{10}\left(\frac{A_d}{|A_c|}\right)\ dB \tag{2-2}$$

where $A_d$ and $A_c$ are the amplification gain for differential and common mode operation. The calculated two-dimensional CMRR at varying gate biasing voltages is shown in Figure 2-7. From the plot we observe, under appropriate gate biasing points, our un-optimized dual-gate graphene ambipolar device can already achieve CMRR of over 80 dB. Importantly, our device utilizes a much simplified design compared to conventional amplifier, namely a single device can achieve both common and differential mode amplifications. We note that all measured devices show the same characteristics and confirm the high CMRR, as shown in Figure 2-8.

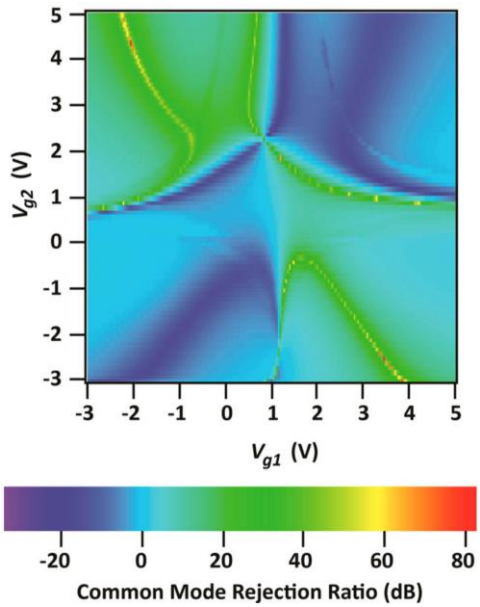


Figure 2-7 The two-dimensional (2D) color plot of common mode rejection ratio versus the dual-gate biasing voltages. The CMRR values are calculated from the common mode and differential mode measurements plotted in Figure 2-4(c) and Figure 2-6(c). High noise rejection can be achieved with either pn or np differential mode biasing conditions.

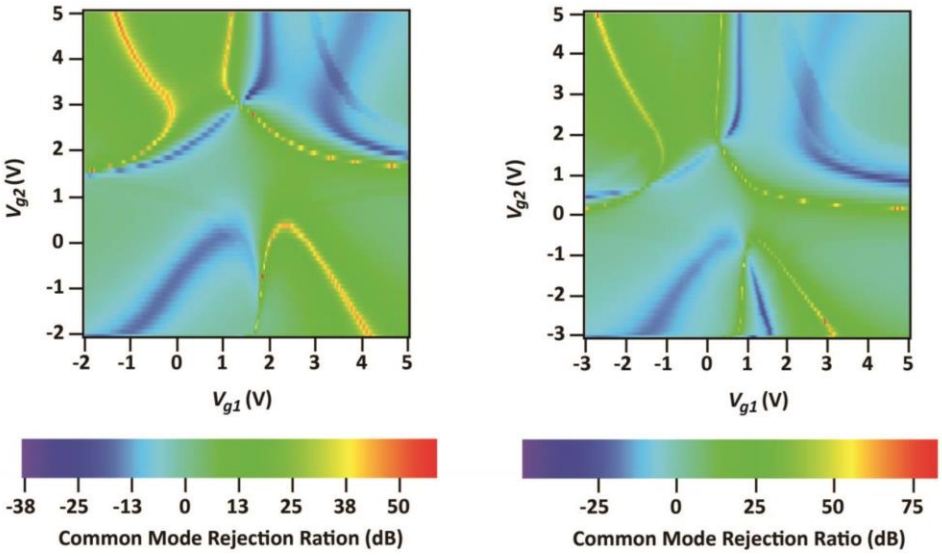


Figure 2-8 The two-dimensional (2D) color plot of CMRR versus dual-gate biasing voltages for two other devices. Measurements are done under the same condition as in Figure 2-7, and high noise rejection is once again confirmed.

In addition, the output frequency spectrum analysis is also being done by using a commercial FFT spectrum analyzer (Stanford Research System SR760) with carrier frequency at 30 kHz, our device shows a clean spectrum and higher order harmonics are negligible, as shown in Figure 2-9. We do notice small peaks at higher frequency, but not at the harmonics of the carrier frequency. These are likely due to the measurement setup and the custom-built phase shift module.

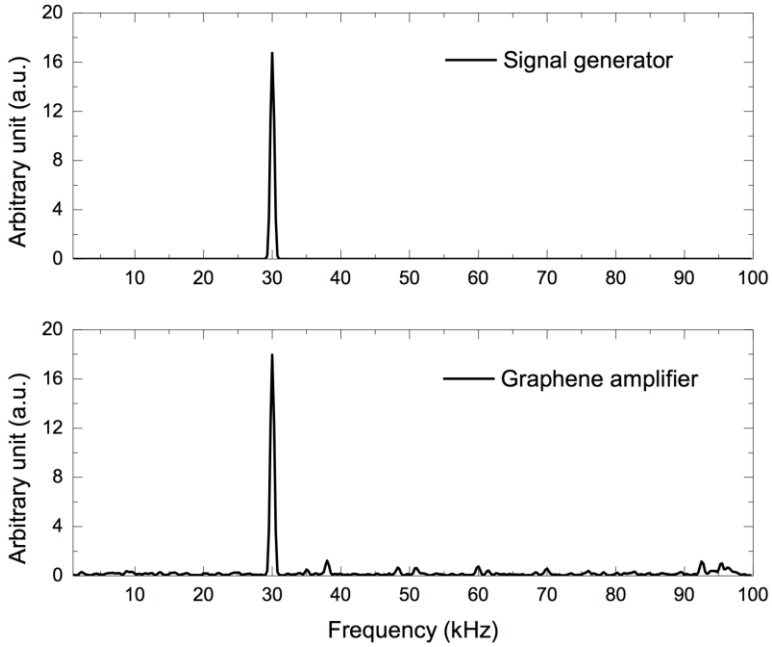


Figure 2-9 Frequency spectrum analysis by using a commercial FFT spectrum analyzer (Stanford Research System SR760). The carrier frequency is 30 kHz.

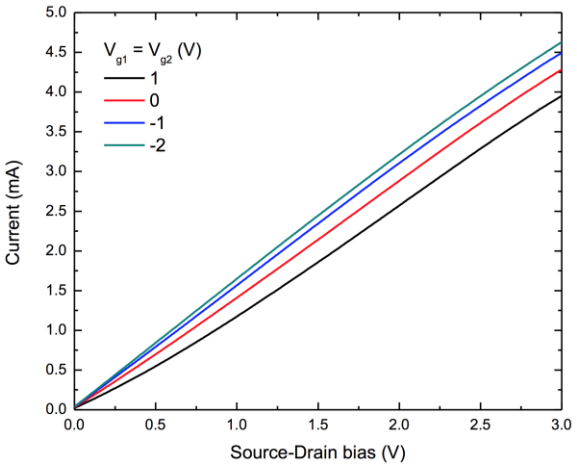


Figure 2-10 Output characteristics I-$V_{ds}$ of dual-gate graphene amplifier under different gate bias. There is no current saturation due to the semi-metallic nature of graphene.

## 2.5 Conclusion

In summary, we demonstrated a new type of dual-gate graphene ambipolar device with capability of operating under both common and differential modes to realize signal amplification. The signal goes through two stages of modulation, where the phase of signal can be individually modulated to be either in phase or out of phase at two stages by exploiting the ambipolarity of graphene. As the results, both common and differential mode amplifications can be achieved within one single device, which is not possible in the conventional silicon-based amplifier circuit configuration. In addition, a common-mode rejection ratio (CMRR) over 80 dB can be achieved, making it possible for low noise circuit applications.

However, our current generation of devices is not without some serious limitations.

First, the output characteristics shown in Figure 2-10 shows the lack of current saturation due to the semi-metallic nature of graphene, potentially limits the intrinsic voltage gain and maximum frequency of the devices. Second, the device is still limited by the small voltage gain, ~1 for common mode operation and close to 2 for differential mode operation. However, high gain graphene amplifiers have been shown in literatures through the adoption of high-k dielectrics [105] and thinner dielectrics [106]. More importantly, the results shown here not only open up new directions of graphene-based ambipolar electronics that greatly simplify the RF circuit complexity and the design of multi-function device operation but also hint at a broad range of graphene-based ambipolar electronics which can enable More-Moore and More-than-Moore technologies [107]–[110] in the post-CMOS era.

# Chapter 3

# Realization of Mid-Infrared Graphene Hyperbolic Metamaterials

## 3.1 Introduction

Hyperbolic metamaterials (HMMs) are artificially structured materials designed to attain an extremely anisotropic optical response, in which the permittivities associated with different polarization directions exhibit opposite signs [111]–[113]. Such anisotropic behavior results in an isofrequency surface in the shape of a hyperboloid, which supports propagating high k-modes and exhibits an enhanced photonic density of states. Many interesting applications have been enabled by HMMs. For example, the spontaneous emission rate of quantum emitters can be modified if they are brought close to a HMM [114], and similarly, the scattering cross-section of small scatterers near a HMM is enhanced [115]. The near-field radiative heat transfer associated with HMMs becomes super-Planckian [116]. Also, the propagating high k-modes supported by HMM are exploited to achieve sub-diffraction-limited images using a hyperlens [117]. Some natural

materials such as bismuth, graphite and hexagonal boron nitride exhibit hyperbolic dispersion in specific spectral ranges [118]–[120], while artificial HMMs are most commonly realized with two categories of structures such as metal-dielectric multilayers [114], [117] and metallic nanorod arrays [121]. The former structure can be fabricated layer by layer using vapor deposition, and the latter is often obtained by electrochemical deposition of a metal on porous anodic aluminum oxide. In both cases, metal is the essential element to provide the conducting electrons that make the extreme anisotropicity possible. Metals can also be replaced by doped semiconductors for realizing HMMs in the infrared range [122].

We explore the realization of a particular HMM, in which the role of the metal in providing a conducting layer is taken over by graphene [26], [35], [123]–[129]. Graphene is a two-dimensional (2D) semi-metal with a thickness of only one atom [6], [15]. It has been shown that doped graphene is a good infrared plasmonic material in terms of material loss [28]. As a truly two-dimensional (2D) material that only conducts in the plane, graphene by nature has the anisotropicity required for HMMs. As the thinnest material imaginable, graphene also makes an ideal building block for multilayer structures, as it enables the minimum possible period and therefore the highest possible cutoff for the high k-modes [123], [130], which has been limited in metal and

semiconductor-based HMMs by the non-negligible thickness of those materials. The conductivity of graphene, unlike that of metals, can be effectively modulated by electrical gating or optical pumping [131], [132]. This unique advantage has been demonstrated in other graphene-based metamaterials [133], and can potentially be exploited to realize a tunable HMM, in which the photonic density of states can be controlled electronically on demand. In addition, graphene shows much richer optoelectronic behavior than metals, and the massless Dirac quasi-particles in graphene also give rise to very different carrier dynamics compared with other semiconductors. Various photodetection mechanisms, such as thermoelectric, bolometric, photovoltaic, photo-gating and photo-Dember effects, have been demonstrated with graphene [33], [134]–[136]. Graphene multilayer structures can therefore serve as a unique platform in optoelectronics, incorporating the unusual photonic behavior of HMMs into graphene detectors or other optoelectronic devices. For example, an ultrathin super-absorber enabled by HMM could be incorporated into graphene detectors to enhance the light absorption [126].

Here, the design criterions and material choices for realizing the graphene HMM will be discussed. Graphene is identified as a good practical choice in the mid-infrared range when it is heavily doped. A chemical doping method is developed to obtain the desired high carrier density and ellipsometry is used to characterize the optical

conductivity of monolayer graphene. The metamaterial with multilayer structure is fabricated by repetitive graphene transfers and dielectric deposition. We characterize the effective permittivities of the fabricated metamaterial with ellipsometry to demonstrate the hyperbolic dispersion in the mid-infrared range.

## 3.2 Design of Graphene HMM

Figure 3-1 shows the structure of the graphene-based HMM, which consists of alternating dielectric and graphene layers. Similar graphene-dielectric multilayer structures have been proposed and analyzed theoretically by different groups and shown to function as a HMM operating at terahertz (THz) and mid-infrared frequencies [26], [35], [123]–[129]. Various applications have also been discussed. For example, in our previous work we have calculated theoretically the Purcell factor of a graphene-based HMM with a finite number of layers [35], and we have simulated numerically the light coupling from free space into a graphene-based HMM slab with a metallic grating [126]. In spite of the large body of theoretical work on graphene-based HMMs, no experimental demonstrations have yet been reported, the primary reason being the challenge in obtaining a sufficiently high level of doping in the graphene layers in the required multilayer structure.

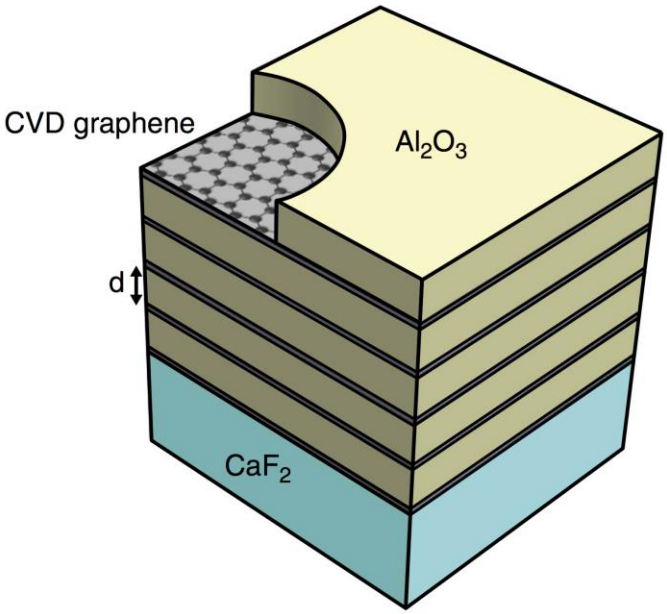


Figure 3-1 The schematic representation of the graphene-dielectric multilayer structure that turns into a HMM at mid-infrared frequencies. It consists of five periods of alternating CVD graphene sheets and $Al_2O_3$ layers on a $CaF_2$ substrate. The thickness of the $Al_2O_3$ layer is ~ 10 nm.

The graphene-dielectric multilayer structure can be homogenized and viewed as a metamaterial using the effective medium approximation (EMA). The effective out-of-plane and in-plane permittivities of this metamaterial can be derived by taking the long-wavelength limit of the Bloch theory [26], [123]–[125]:

$$\varepsilon_{eff,\perp} = \varepsilon_d;\ \ \varepsilon_{eff,\parallel} = \varepsilon_d + i\frac{\sigma Z_0}{2\pi}\left(\frac{\lambda}{d}\right) \tag{3-1}$$

Here $\varepsilon_d$ is the permittivity of the dielectric layer, d is the dielectric thickness and $\sigma$ is the optical conductivity of graphene. $Z_0$ is the vacuum impedance. Here graphene, as a two-dimensional (2D) material, is treated as an infinitely thin layer described by its

in-plane sheet conductivity. As indicated by Equation 3-1, the graphene-dielectric multilayer system forms a uniaxial anisotropic metamaterial. $\varepsilon_{eff,\perp}$ is the same as the constituent dielectric and is always positive. On the other hand, the real part of $\varepsilon_{eff,\parallel}$ becomes negative if

$$\mathrm{Im}\,\sigma > 2\pi(\mathrm{d}/\lambda)(\varepsilon_d/Z_0) \tag{3-2}$$

When this criterion is satisfied, the isofrequency surface becomes a hyperboloid and we obtain HMM. Such an isofrequency surface allows the existence of propagating high k-modes, which can be traced back to the coupled plasmon modes in the graphene-dielectric multilayer structure [35]. The criterion described by Equation 3-2 determines the wavelength at which the optical topological transition between elliptical and hyperbolic dispersions occurs [114].

While most previous theoretical work has concentrated on using high-mobility graphene that may be obtained from mechanically exfoliated or epitaxially grown samples, we use CVD graphene because it is the most realistic choice for practical fabrication of a multilayer structure [68]. Growth of large-area CVD graphene is well established, and it can be transferred onto arbitrary surfaces using polymethyl methacrylate (PMMA) as the carrier material. In spite of its advantage in fabrication, CVD graphene often has a higher degree of disorder, which is typically manifested by a

reduced mobility. As a result of the lower crystal quality, the stronger carrier scattering in typical polycrystalline CVD graphene enhances the free-carrier absorption at THz frequencies, which can be understood from the theoretical optical conductivity of graphene [22]–[24],

$$\sigma(\omega) = \frac{\sigma_0}{2}\left(\tanh\frac{\hbar\omega+2E_F}{4k_BT} + \tanh\frac{\hbar\omega-2E_F}{4k_BT}\right) - i\frac{\sigma_0}{2\pi}\log\left[\frac{(\hbar\omega+2E_F)^2}{(\hbar\omega-2E_F)^2+(2k_BT)^2}\right] + i\frac{4\sigma_0}{\pi}\frac{E_F}{\hbar\omega+i\hbar\gamma} \quad (3\text{-}3)$$

where $\sigma_0$ equals to $e^2/(4\hbar)$, $E_F$ is the Fermi energy relative to the Dirac point and $\gamma$ is the intra-band scattering rate. In this expression, the first two terms correspond to inter-band transitions, while the third term is the Drude-like intra-band conductivity. Figure 3-2 shows a plot of the theoretical optical conductivity given by Equation 3-3 with parameters typical for doped polycrystalline CVD graphene. To realize a good HMM, we need graphene with a large positive imaginary conductivity to interact with light, but with a small real conductivity to minimize the material loss. As shown in Figure 3-2, graphene is lossy at high frequencies when $\hbar\omega > 2E_F$ because of inter-band transitions. On the other hand, at low frequencies when $\hbar\omega \lesssim \hbar\gamma$, graphene also exhibits a large loss because of the intra-band free carrier absorption enabled by scattering. Because CVD graphene typically has a $\hbar\gamma$ of tens of meV, it is a lossy material at THz frequencies [30]. As shown by Figure 3-2, however, there is a spectral range between the two lossy regions, such that the imaginary part of the conductivity exceeds the real part. As this spectral

range lies in the mid-infrared part of the spectrum, CVD graphene-based HMM operates better in the mid-infrared than the THz region. Also, Figure 3-2 indicates that doping can improve the properties of graphene for realizing a HMM. A large $E_F$ can turn off the inter-band absorption by the Pauli blocking and increase the Im σ required for achieving negative $\varepsilon_{eff,\parallel}$. Furthermore, doping can also suppress the intra-band scattering by screening charged impurities [30], [137].

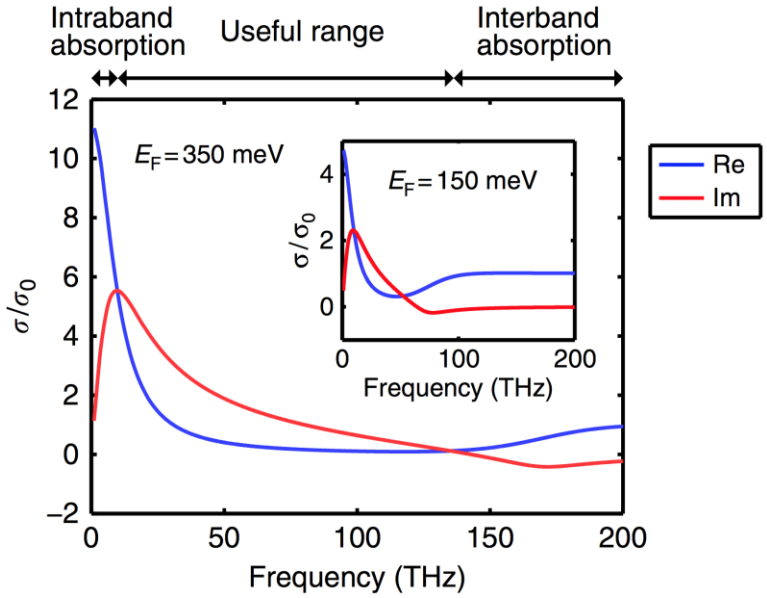


Figure 3-2 The theoretical optical conductivity of graphene. It is plotted with $E_F$ = 350 meV and $\hbar\gamma$ = 40 meV. These numbers correspond to heavily doped CVD graphene. At the high-frequency end of the spectrum, graphene is lossy because of the inter-band absorption. At the low-frequency end, graphene is again lossy because of the intra-band free-carrier absorption. There is a useful spectral range in between, where the imaginary part of the optical conductivity exceeds the real part. In this particular example, the useful wavelengths range from 2 to 30 μm in the mid-infrared range. The inset shows another example of lightly doped CVD graphene with $E_F$ = 150 meV and $\hbar\gamma$ = 40 meV. The useful wavelength range is smaller when the doping is lower.

## 3.3 Characterization of the Optical Conductivity in Graphene

Because graphene is the key building block of the metamaterial, it is important to have an accurate measurement on the optical conductivity of the actual CVD graphene layers used to fabricate the sample. Although the theoretical optical conductivity given by Equation 3-3 provides a good guideline for designing the graphene HMM, real CVD graphene layers can have imperfections or extrinsic properties that are not taken into account by Equation 3-3. We therefore need to characterize actual graphene samples and examine the scope of validity of Equation 3-3.

We have developed a technique based on ellipsometry to measure the optical conductivity of truly two-dimensional (2D) materials [27], discussed in Chapter 1.3.1. In this technique, the analysis used in conventional ellipsometry is modified to handle the infinitely thin 2D material whose properties are fully described by the 2D optical conductivity. To characterize actual CVD graphene samples with this technique, we have prepared two kinds of samples, unintentionally doped and the chemically doped CVD graphene, on $CaF_2$ substrates by the standard PMMA transfer method. Even without chemical treatment, unintentionally doped CVD graphene is p-type because of adsorbed gas molecules and residual ammonium persulfate from the transfer process [19], [64].

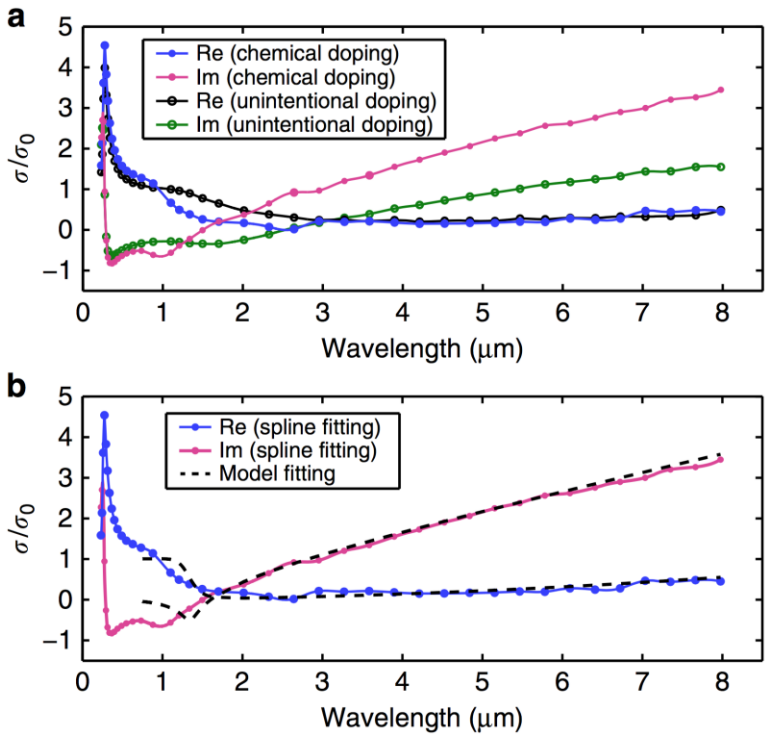


Figure 3-3 The optical conductivity of CVD graphene measured by ellipsometry. (a) The real and imaginary part of the optical conductivity of the chemically doped CVD graphene (blue and magenta curves) and the unintentionally doped CVD graphene (black and green curves). These curves are mathematically expressed by cubic splines, and the markers denote the control points of the splines. The chemically doped CVD graphene has a larger imaginary conductivity in the mid-infrared range. (b) The real and imaginary part of the optical conductivity of the chemically doped CVD graphene. The blue and magenta curves are obtained by fitting with cubic splines, and the black dash lines are obtained by using the model given by Equation 3-3. The model fitting is consistent with the spline fitting in the mid-infrared range. The extracted $E_F$ and $\hbar\gamma$ from the model fitting are 460 and 23 meV, respectively, which corresponds to a mobility of ~ 2,000 $cm^2V^{-1}s^{-1}$.

The chemically doped CVD graphene is prepared by a solution process that leaves a sub-monolayer of tris (4-bromophenyl)ammoniumyl hexachloroantimonate (also known as magic blue), a somewhat air-stable p-type dopant, on the surface [138], [139]. Figure

3-3(a) shows the optical conductivities of both samples measured with ellipsometry. The optical conductivities shown here are mathematically described by cubic splines without assuming an a priori theoretical expression like Equation 3-3. Consistent with Figure 3-2, in the mid-infrared range the chemically doped graphene has a larger imaginary conductivity, which is necessary for creating the extreme anisotropicity in the metamaterial.

Although the spline-fitted conductivity of actual CVD graphene sample shown in Figure 3-3(a) is useful in many applications, a conductivity model based on a theoretical expression such as Equation 3-3 provides more physical insight and requires fewer unknown parameters to perform the fit. The latter is important when we want to parameterize the homogenized metamaterial, which will be discussed in next section. In Figure 3-3(b), we examine how well Equation 3-3 works for our chemically doped CVD graphene samples. In fitting the ellipsometer data, we express the optical conductivity $\sigma(\omega)$ by the model given by Equation 3-3 with $E_F$ and $\gamma$ being the only two unknown fitting parameters. We also show in the same figure the spline-fitted conductivity obtained from the same set of data. It is apparent that the resulting conductivity based on Equation 3-3 overlaps very well with the spline-fitted conductivity throughout the mid-infrared range, assuring the validity of using Equation 3-3 for the mid-infrared

metamaterial. We extract from the fit that $E_F$ = 460 meV and $\hbar\gamma$ = 23meV. A mobility of ~ 2,000 $cm^2V^{-1}s^{-1}$ can be calculated from these numbers using the relationship $\mu = e\pi\hbar {V_F}^2/(\hbar\gamma E_F)$, where $\mu$ is the mobility and $V_F$ is the Fermi velocity.

In the mid-infrared range, the optical conductivity is mostly determined by intra-band transitions, which are described by the Drude-like term in Equation 3-3. Our result is consistent with reference [30], which shows that the Drude model can successfully fit the measured absorption spectrum of CVD graphene over a broad range of infrared wavelengths. We do not apply Equation 3-3 in the ultraviolet to visible wavelength range because the many-body correction has been shown to be important [140], [141]. There is some discrepancy between the model and spline fits in the near-infrared regime ~ 1.5 μm, that is, near the wavelength corresponding to inter-band transitions close to the Fermi level. The origin of this discrepancy is not quantitatively understood, but may be related to spatial inhomogeneity in the Fermi energy or other disorder effects. Since the optical topological transition wavelength of our HMM is very far from this spectral region, and the fit is excellent over the entire mid-infrared range, the failure of the simple model in the near-infrared region does not affect the behavior of the material in the mid-infrared, which is the region of concern in this work. Equation 3-3 thus provides an excellent description for the mid-infrared conductivity. Other

imperfections that are typically present in transferred CVD graphene samples, such as the existence of small multilayer graphene patches and holes, can also contribute to the deviations observed in Figure 3-3(b) [142].

### 3.4 Measurement of the Effective Permittivity of Graphene HMM

We have fabricated the multilayer structure shown in Figure 3-1, which consists five periods of alternating CVD graphene and $Al_2O_3$. The CVD graphene is transferred by the PMMA method and doped with tris (4-bromophenyl)ammoniumyl hexachloroantimonate (magic blue). The $Al_2O_3$ dielectric layer is grown by atomic layer deposition (ALD). We choose $Al_2O_3$ as the dielectric material, because it has negligible loss at the mid-infrared wavelengths up to 8 μm. The dielectric thickness is chosen to be ~ 10 nm to create an optical topological transition in the mid-infrared range.

To characterize the metamaterial, we use infrared ellipsometry, which is appropriate to probe the effective permittivity of a metamaterial, since it measures the sample with free-space plane waves and the transverse wave vector ($k_0 \sin\theta$) associated with the free-space plane waves is very small ($k_0 \sin\theta d \ll 1$, where $\theta$ is the angle of incidence). We are therefore probing the low k-modes of the metamaterial, ensuring the validity of the long-wavelength approximation. Although the long-wavelength approximation is

evidently satisfied for our metamaterial ($d/\lambda < 1/300$ in our case), we still need to confirm the validity of the EMA with a rigorous transfer-matrix calculation, since the EMA is derived for an infinite periodic system, while our metamaterial has only five periods. In Figure 3-4, we show the transfer-matrix calculation of five periods of graphene-dielectric multilayer structure and the EMA calculation with the structure homogenized into an anisotropic layer, with the permittivities of the homogenized anisotropic layer given by Equation 3-1. Here we calculate the ellipsometric angles $\Psi$ and $\Delta$, the quantities an ellipsometer acquires directly, at different incident angles. $\Psi$ and $\Delta$ are defined by $r_p/r_s = (tan\Psi)e^{i\Delta}$, where $r_p$ and $r_s$ are the reflection coefficients for p and s light, respectively. Numbers used in the simulation are chosen according to measured material properties of the individual layers. As demonstrated by Figure 3-4, the two methods give very close results, confirming that the five-period graphene-dielectric structure, in the low k-regime probed by ellipsometry, can be accurately treated as a metamaterial with the effective permittivities given by Equation 3-1. In fact, in the low k-regime, even one period of the graphene-dielectric unit cell can be homogenized by the same EMA formula given by Equation 3-1 and still reproduce the optical properties accurately. However, the high k-regime is where the real interest of HMM lies, the high k optical properties depend on the number of unit cells in the

metamaterial. The five-period structure in our experimental realization of graphene HMM is chosen to create desirable high k optical properties.

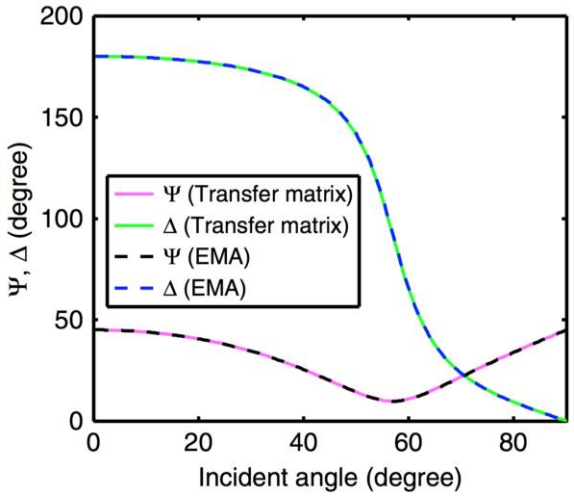


Figure 3-4 Calculation of ellipsometric angles with exact transfer-matrix method and EMA. Ellipsometric angles $\Psi$ and $\Delta$ are defined by $r_p/r_s = (tan\Psi)e^{i\Delta}$, where $r_p$ and $r_p$ are the reflection coefficients for p and s light, respectively. They are the quantities an ellipsometer measures. The transfer-matrix method calculates the response of five periods of graphene-dielectric multilayer structure, while the EMA simulates a homogenized anisotropic layer with the permittivities given by Equation 3-1. This calculation shows that the EMA is an accurate approximation for the structure. The wavelength used in this simulation is 6 μm. The material properties are $\varepsilon_d$ = 2.1 and σ = (0.43 + 0.98i)$\sigma_0$. Thickness d = 10 nm. The substrate has a refractive index of 1.39.

The results of infrared ellipsometry, ellipsometric angles $\Psi$ and $\Delta$ for our HMM sample, are shown in Figure 3-5(a) and Figure 3-5(b), from which we extract the effective permittivities by fitting the acquired data. A robust and physical fitting in

ellipsometry requires correct prior knowledge about the sample parameters, which allows us to use a minimal number of unknowns.

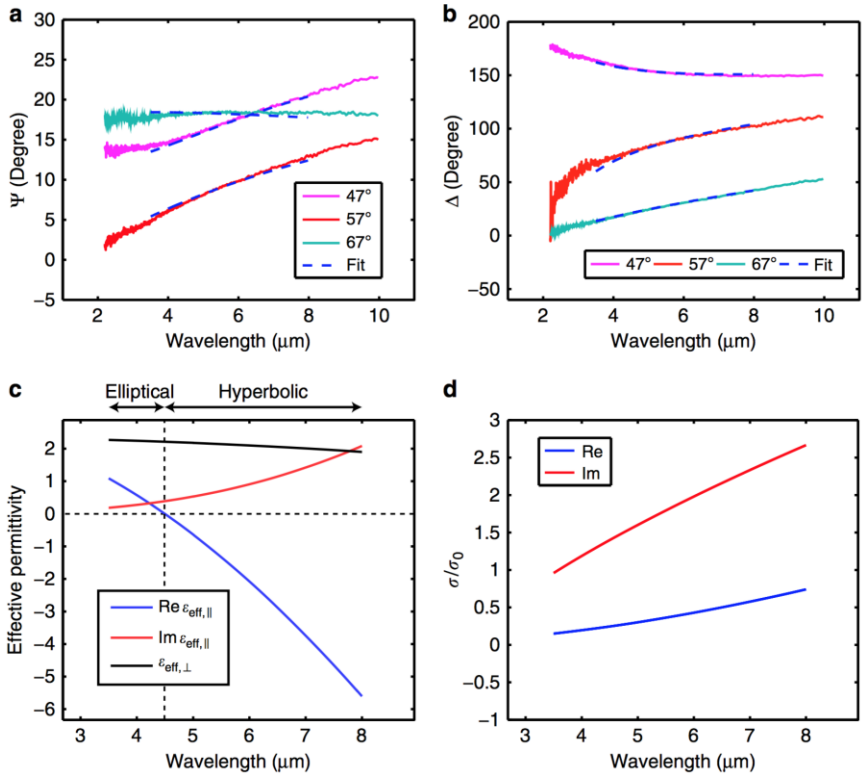


Figure 3-5 Extraction of the effective permittivity of the graphene HMM. (a,b) The ellipsometric angles Ψ and Δ acquired from the graphene-dielectric multilayer structure. The measurement is performed at incident angles of 47°, 57° and 67°. The blue dash lines show the fitting by homogenizing the multilayer structure into a metamaterial with the effective permittivities given by Equation 3-1. We extract from the fitting that $E_F$ = 365 meV and $\hbar\gamma$ = 41 meV. (c) The extracted effective permittivity of the metamaterial, which exhibits an optical topological transition from elliptical to hyperbolic dispersion at 4.5 μm. When the wavelength is at 6 μm, $\varepsilon_{eff,\parallel}$ equals 2.1+0.9i and $\varepsilon_{eff,\perp}$ equals 2.1. (d) The extracted optical conductivity of the constituent CVD graphene in the metamaterial.

Since our simulation in Figure 3-4 demonstrates that the EMA is an accurate description for the multilayer structure, we can apply Equation 3-1 in fitting the data. More precisely, we fit the experimental data to a layer of an anisotropic material on a $CaF_2$ substrate with the permittivities of the anisotropic material given by Equation 3-1. In Equation 3-1, we know everything except the optical conductivity of graphene, as we have measured the thickness independently after depositing each $Al_2O_3$ layer, and we have measured the refractive index of the ALD-grown $Al_2O_3$ in the relevant spectral range independently on a reference sample. Furthermore, as shown by Figure 3-3(b), considering the mid-infrared range with only the intra-band response, the expression of Equation 3-3 is a good description for the optical conductivity of the actual CVD graphene layers. Therefore, we can apply Equation 3-3 and parameterize the optical conductivity with only $E_F$ and $\gamma$. As a result of this independent knowledge of the sample, only two unknowns, $E_F$ and $\gamma$, are sufficient to fit the experimental data of the multilayer metamaterial.

The fitted results of the ellipsometric angles $\Psi$ and $\Delta$ are plotted as the blue dash lines in Figure 3-5(a) and Figure 3-5(b). We restrict the wavelengths range of the fitting to 3.5-8 μm, where the lower bound is limited by the requirement of intra-band only response in the application of Equation 3-3, and the upper bound is because of the limited

transparent spectral range of $Al_2O_3$. As shown by Figure 3-5, we are able to reproduce all six $\Psi$ and $\Delta$ curves acquired at different incident angles with only two free parameters in the fitting. The extracted $E_F$ is 365 meV, and the extracted $\hbar\gamma$ is 41 meV. The extracted $E_F$ is lower than the value we typically obtain from chemically doped monolayer CVD graphene, because some dopants are lost in the ALD process because of the vacuum environment and the elevated temperature. The obtained scattering rate $\hbar\gamma$ is higher than the value of graphene on $CaF_2$ substrate shown in Figure 3-3. This can be explained by the fact that the carrier scattering in graphene depends on the surrounding environment, from which we conclude that sandwiching graphene between $Al_2O_3$ increases the carrier scattering. Figure 3-5(c) shows the effective permittivity of the graphene metamaterial given by the extracted values of $E_F$ and $\gamma$. $\varepsilon_{eff,\perp}$ is always positive because it equals the permittivity of $Al_2O_3$. On the other hand, the real part of $\varepsilon_{eff,\parallel}$ changes from positive to negative at 4.5 μm indicating an optical topological transition from an elliptical metamaterial to a HMM. This graphene metamaterial is therefore a transverse epsilon-near-zero metamaterial at the wavelength of 4.5 μm [123]. The imaginary part of $\varepsilon_{eff,\parallel}$ is several times smaller than the real part in most of the spectral range with hyperbolic dispersion, indicating that the loss of this HMM is

reasonably low. In Figure 3-5(d), we plot the optical conductivity of the constituent graphene sheet of the metamaterial using the extracted $E_F$ and $\gamma$.

## 3.5 Conclusion

Our characterization by the infrared ellipsometry demonstrates that the graphene-dielectric multilayer structure indeed experiences an optical topological transition from an elliptical to a hyperbolic dispersion in the mid-infrared range, confirming the theoretical predictions in previous works [26], [35], [123]–[129]. Our metamaterial sample has an optical topological transition at a wavelength of 4.5 μm, and maintains good hyperbolic properties up to 8 μm. The upper bound of the wavelength range is limited by the absorption in $Al_2O_3$ and CVD graphene. While the absorption in the dielectric layer can be overcome by replacing $Al_2O_3$ with other infrared transparent materials such as ZnSe, the absorption in CVD graphene is limited by the quality of graphene. Recently, there have been reports of the growth of large-area CVD graphene with the quality of a single crystal [143], and new transfer process for CVD graphene without degrading the mobility [142]. With higher quality CVD graphene, the intra-band absorption resulted from scattering could potentially be suppressed. The transition wavelength, as determined by Equation 3-2, can be shifted by choosing the dielectric

thickness or controlling the doping of graphene. The latter is especially useful if it can be done by the electrical gating. Shifting the transition wavelength farther into the infrared can be done by using lightly doped graphene or thicker dielectric. We have also realized a graphene HMM with the same structure except that the CVD graphene layers were not chemically doped, resulting in a transition wavelength red-shifted to 7.2 μm. On the other hand, blue shifting the transition wavelength is limited by the highest doping and the thinnest dielectric layers achievable in practice. While the structure reported in this work has only five periods, the procedure developed here can be repeated to scale up the graphene HMM. Some applications of HMMs do not require a large number of periods; for example, only a few periods are sufficient to produce a Purcell factor close to a semi-infinite structure, according to the theoretical calculations [35].

# Chapter 4

# Review of Photo-Gating Effect for Broadband and High Responsivity Graphene Photodetectors

## 4.1 Introduction

The ability to detect light over a broad spectral range is central to several technological applications in imaging, sensing, spectroscopy and communication [144], [145]. Today, different technologically important wavelength regimes are detected by separate photoactive semiconductors with appropriate bandgaps. For example, GaN, silicon and InGaAs are typically exploited for sensing in the ultraviolet, visible and near-infrared regimes, respectively, whereas the detection of mid-infrared photons generally relies on small-bandgap semiconductor compounds such as HgCdTe, PbS or PbSe, and thermal sensing techniques are utilized for detection in the far-infrared regime. In contrast to these materials, graphene is a promising optoelectronic candidate material for ultra-broadband photodetectors due to its gapless band structure [56], [146], thus the absorption spectrum covers the entire ultraviolet to far-infrared range [56], [146].

The difficulty with utilizing graphene in standard photodetector structures is that the lifetime of photogenerated carriers is very short, and it is therefore necessary to separate the electrons and holes on a sub-picosecond timescale in order to efficiently generate a photocurrent and avoid simple heating of the graphene layer. So far, nearly all graphene-based photodetectors focus on exploiting graphene–metal junctions or graphene p–n junctions for extracting photocurrent [134], [147]–[152]. Unfortunately, these sensing schemes suffer from the small area of the effective junction region contributing to the photocurrent as well as the weak optical absorption of graphene monolayer nature, therefore the responsivity is therefore limited to a few $mAW^{-1}$. Integrating graphene with plasmonic nanostructures [153]–[155] or microcavities [156], [157] can enhance the light–graphene interaction and improve the responsivity to tens of $mAW^{-1}$. However, the enhancement can only be achieved at the designed resonant frequencies, restricting their applications for broadband photodetection. With this in mind, the idea of silicon waveguide-integrated graphene photodetectors was recently proposed, demonstrating broadband photodetection with enhanced responsivity to tens of $mAW^{-1}$ [156], [157]. Photoresponsivity above 0.1 $AW^{-1}$ can also be achieved in transition-metal dichalcogenide/graphene stacks by exploiting the strong light–matter interaction [158]. Band structure engineering in graphene has also recently been explored for

photoresponsivity enhancement [159], but efficient photodetection can only be achieved below 150 K due to the short electron lifetime in midgap states at elevated temperatures.

An alternative approach is to exploit photoconductive gain in graphene. Although graphene is conventionally regarded as a poor photoconductor because of its ultrafast hot carrier recombination [46], [49], [160], [161], recent studies have demonstrated that hybridized graphene/quantum-dot photodetectors can improve the responsivity and achieve high photoconductive gain to be ~ $1 \times 10^7$ $AW^{-1}$ [162], [163]. This sensitive detection scheme is attributed to a strong photo-gating effect induced by trapped photocarriers in the quantum dots. Despite the excellent device responsivity, light absorption relies on the quantum dots instead of the graphene, thus restricting the spectral range of photodetection.

Our group report an ultra-broadband photodetector design based on graphene double-layer heterostructures [33]. Under optical illumination, the trapped charges on the top graphene layer can result in a strong photo-gating effect on the bottom graphene channel layer, yielding an unprecedented photoresponsivity over an ultra-broad spectral range. By engineering a proper tunnel barrier, we demonstrate prototype devices achieving ultra-broadband photodetection and a room-temperature mid-infrared responsivity comparable with state-of-the-art infrared photodetectors operating at low

temperature [164]. These results address key challenges for broadband infrared detectors, and are promising for the development of graphene-based hot-carrier optoelectronic applications.

## 4.2 Graphene Double-Layer Heterostructure Photodetector

The graphene films used in this work were grown by chemical vapor deposition (CVD) on copper foil and then transferred onto a $Si/SiO_2$ substrate [165]. The single-layer nature of the graphene films was confirmed by Raman spectroscopy. To fabricate graphene double-layer heterostructures, we first transferred a graphene film onto a degenerately p-doped silicon wafer with 285 nm thermal oxide. Photolithography, graphene plasma etching and metal lift-off processes were used to fabricate the bottom graphene transistor. The sample was then covered by a thin tunnel barrier film, which are blanket-deposited by radiofrequency sputtering. Here, 5 nm $Ta_2O_5$ and 6 nm intrinsic silicon are used for visible and infrared photodetection respectively. Finally, the top graphene layer was transferred on top of the $Ta_2O_5$ thin film, and subsequent photolithography, graphene etching and metal lift-off processes were used to fabricate the top graphene transistor. Figure 4-1(a) shows the device schematic of graphene double-layer heterostructure photodetector, which is composed of a pair of stacked

graphene monolayers (top layer, gate; bottom layer, channel) sandwiching a thin tunnel barrier. The graphene functions not only as the charge transport channel but also as the light absorber.

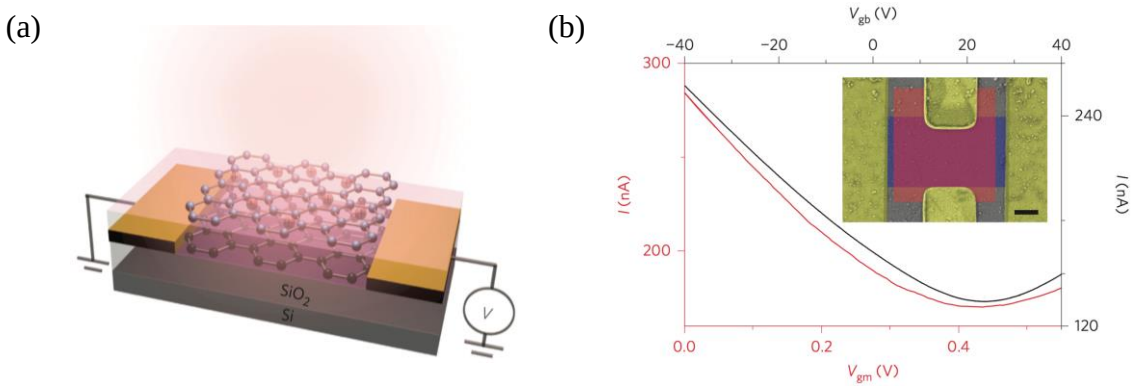


Figure 4-1 Graphene double-layer heterostructure photodetector. (a) Schematic of device structure. (b) Black (right and top axes): transfer curve for bottom graphene layer using a silicon backgate ($V_{gb}$). Red (left and bottom axes): transfer curve for top graphene layer using the bottom graphene as the gate ($V_{gm}$). From these transport curves, we calculate the Fermi energies of the top and bottom graphene layers to be 4.756 eV and 4.655 eV, respectively. Inset: False- color scanning electron microscopy (SEM) image of the device. The gold areas indicate the metal electrodes and the purple and red areas the bottom and top graphene layers, respectively. Scale bar, 1 μm.

The intrinsic doping level and Fermi energy of the bottom graphene layer can be readily determined by the backgate voltage ($V_{gb}$)-dependent transfer curve, as shown in Figure 4-1(b) black curve. To determine the Fermi energy of the top graphene layer, we can operate the bottom graphene layer as a gate ($V_{gm}$) and measure its gate effect on the top graphene layer, as shown in Figure 4-1(b) red curve. The top graphene layer was

found to be more heavily p-doped relative to the bottom graphene layer, with an average Fermi energy difference of 0.12 eV.

### 4.3 Photo-Gating Effect

The photo-gating working principle of the graphene double-layer heterostructure photodetector can be understood through the energy band diagram in Figure 4-2(a). Due to the Fermi energy difference between the top and bottom graphene layer, the energy band of the tunneling barrier is tilted toward the bottom graphene layer in order to equilibrate the Fermi level.

For typical photodetection operation, the potential of the top graphene layer is allowed to float while the light-induced conductance change of the bottom graphene layer is measured in the bottom graphene layer transistor. Under optical illumination, photoexcited hot carriers can tunnel efficiently into the nearby graphene layer. Most importantly, the asymmetric tunneling barrier favors hot electrons tunneling from the top to the bottom graphene layer. In contrast to conventional phototransistors as well as lateral graphene devices [134], [151], [166], photoexcited hot electrons and holes are separated in our structure by selective quantum tunneling into opposite graphene layers, thereby minimizing hot carrier recombination. As a result, this tunneling process leads to

trapped positive charges build-up in top graphene layer, affecting bottom channel conductance. In particular, the graphene channel has high carrier mobility and is very sensitive to external electrostatic perturbation, while the thin oxide film in this device design not only favors hot carrier tunneling, but also induces high interlayer dielectric capacitance. All these factors contribute to a strong photo-gating effect and yield efficient photon detection as well as an unprecedented photoresponsivity over an ultra-broad spectral range.

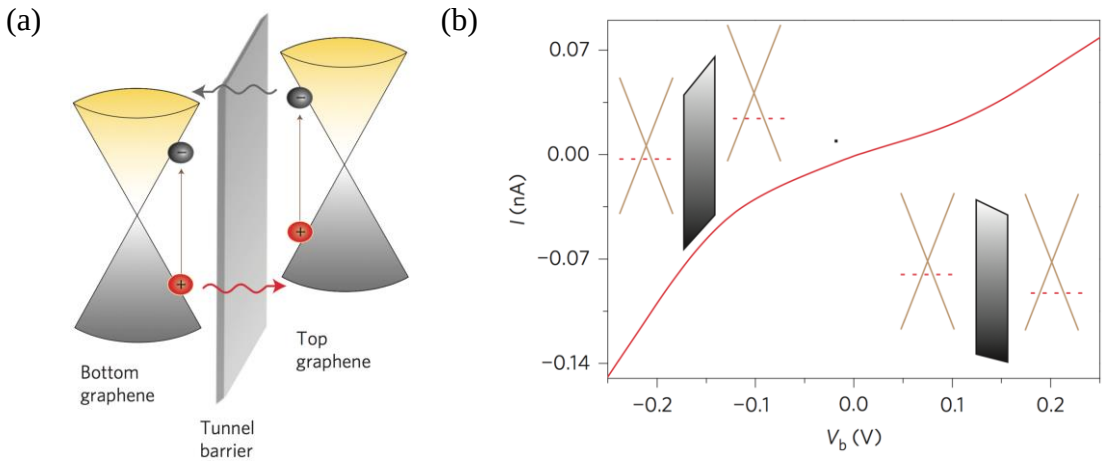


Figure 4-2 (a) Schematic of band diagram and photoexcited hot carrier transport under light illumination. Electrons and holes are represented by grey and red spheres, respectively. Vertical arrows represent photoexcitation, and lateral arrows represent tunneling of hot electron (grey) and hole (red). (b) Vertical tunneling current as a function of bias voltage applied across two graphene layers. The bottom layer is grounded, and bias voltage is applied to the top layer. Inset: Schematic band diagrams under forward and reverse bias. Red dashed lines indicate the Fermi levels of the graphene layers.

Critically, these two closely spaced graphene layers are electrically isolated, with an interlayer resistance of > 4 GΩ. The tunneling dark current can be measured by applying a bias voltage across the graphene double layer, as shown in Figure 4-2(b). The I–V characteristics show a larger magnitude of tunneling current in the negative bias region than in the positive bias region, also in agreement with the asymmetry of the tunnel barrier depicted in Figure 4-2(a).

To further confirm the hot carrier tunneling mechanism, we performed scanning photocurrent spectroscopy [147], [148], [151] and directly measured the hot carrier tunneling current across the graphene layers. The tunneling current due to photoexcitation was measured under the short-circuit condition with the bottom graphene layer grounded, as shown in Figure 4-3(a). Figure 4-3(b) shows a scanning photocurrent image of the device under continuous-wave laser excitation at 900 nm. The result clearly shows that photocurrent is generated within the overlapped region of two graphene layers instead of at the graphene–metal junctions, suggesting that the charge separation arises from hot carrier tunneling and not at the graphene-metal junctions as in conventional graphene detectors. Additionally, the photocurrent polarity is negative, providing direct evidence that the asymmetry of the tunnel barrier facilitates hot electron transport from the top to the bottom graphene layer. Furthermore, we measured the same device with a shorter

irradiation wavelength at 800 nm. A scanning photocurrent map shows qualitatively similar features, but nearly six times larger photocurrent compared with 900 nm excitation at the same laser intensity, as shown in Figure 4-3(c). The dependence of photocurrent on photon energy provides further support for hot carrier tunneling, because carriers excited to higher energies should have a higher injection rate through the barrier [167]. We also emphasize that the direct photocarrier tunneling current between two graphene layers is seven orders of magnitude smaller than the photo-gating effect shown in Figure 4-4(b) (10 pA versus 100 mA). This result further highlights the advantage of utilizing the photo-gating effect of the top graphene layer for high responsivity photodetection. The measured wavelength-dependent photoresponsivities of the graphene photodetector further support the concept that the responsivity is directly related to the photon energy dependence of the hot carrier tunneling rate. As shown in Figure 4-3(d), photoresponsivities of the graphene photodetector at 800 nm are also about six times greater than at 900 nm, suggesting that the device responsivity is closely related to hot carrier injection rate. As control experiments, we also measured the photoresponse of a graphene transistor covered by 5 nm $Ta_2O_5$ but without the top graphene layer. As shown in Figure 4-3(e), the transfer curve shifts are much smaller and, most importantly, in the opposite direction when compared with the photoresponse of the graphene double-layer

photodetector in Figure 4-4(a). This striking difference reveals the central role of the top graphene layer for both light absorption and photo-gating.

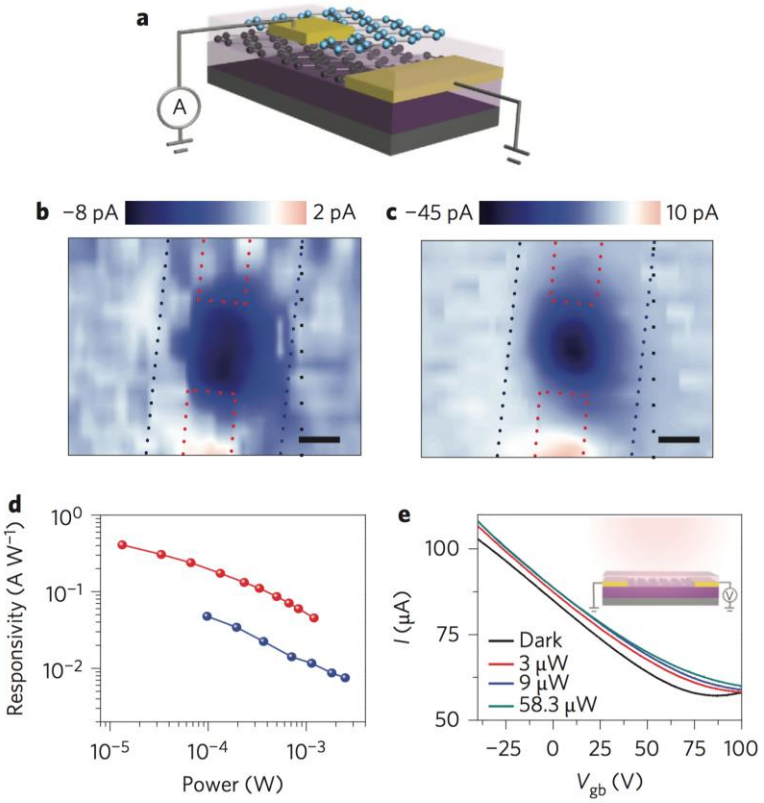


Figure 4-3 Photoexcited hot carrier tunneling in graphene double-layer heterostructures. (a) Schematic of electrical measurement setup for scanning photocurrent imaging. Photocurrent across the two graphene layers is directly measured to confirm the photoexcited hot carrier tunneling mechanism. (b)(c) Scanning photocurrent images of the graphene double-layer heterostructures at excitation wavelengths of 900 nm (b) and 800 nm (c). Blue dotted lines indicate the edges of the bottom electrodes and red dotted lines the edges of the top electrodes. Vertical tunneling current across the heterostructures was measured under the short-circuit condition with the bottom graphene layer grounded. The laser spot size for these scanning measurements was ~ 1.5 μm, and the laser power was 1 mW. Scale bar, 2 μm. (d) Responsivity comparison of graphene photodetector at wavelengths of 800 nm (red) and 900 nm (blue). (e) Photoresponse of a control device with identical design, except for the absence of the top graphene layer. Inset: Schematic of control device.

## 4.4 Broadband Photodetection

To confirm the above mechanism, the photoresponse of graphene double-layer heterostructure photodetectors is successfully demonstrated in visible, near- to mid-infrared regimes respectively.

### 4.4.1 Photoresponse in Visible Regime

Figure 4-4(a) shows the effect of light illumination (continuous wave, $\lambda$ = 532 nm) on the gate response of the bottom graphene transistor over four orders of magnitude optical power. Interestingly, the transfer curve shifts dramatically toward negative $V_{gb}$ with increasing laser power, and a Dirac point voltage shift of 40 V is observed, as shown in Figure 4-4(c) inset. This observation supports the proposed detection mechanism; that is, efficient tunneling of high energy hot electrons leads to positive charge build-up in the top graphene layer, giving rise to a strong photo-gating effect and n-doping of the bottom graphene channel, as shown in Figure 4-4(a) inset. The net photocurrent can be obtained by subtracting the dark current from the light current ($I_{light}$ - $I_{dark}$), and is plotted in Figure 4-4(b). It is clear that the magnitude of photocurrent increases with excitation power. More importantly, the photocurrent signal can be gate-modulated, offering convenient on–off switching control for photodetection.

The noise properties in this device design are determined mainly by the dark current in the conducting channel. We measured the frequency-dependent noise spectral density of the photodetector under 1 V bias and found that a room temperature noise equivalent power (NEP) of $1 \times 10^{-11}$ $WHz^{-1/2}$ at 1 Hz is achieved in our proof-of-concept device.

To gain further insight into the characteristics of this photodetector, we extracted the power dependence of the current and calculated the responsivity of the device, as shown in Figure 4-4(c) and Figure 4-4(d) respectively. Under low excitation power, the device shows a remarkable responsivity of greater than 1,000 $AW^{-1}$ at 1 V source-drain bias voltage ($V_{SD}$), suggesting that the built-in amplification mechanism can efficiently convert the photon energy into a large electrical signal. In addition, the photo-induced current also shows a linear dependence on the bias voltage, as shown in Figure 4-4(e), suggesting higher responsivity can be readily achieved by applying a larger bias voltage. The time-dependent photo-induced current measurement under on-off light modulation was also performed with 1 V bias voltage at room temperature, as shown in Figure 4-4(f). A reset gate voltage pulse of 10 ms was used for fast switching [162] and a current modulation of 7 μA was clearly evident. We note that the speed of our proof-of-concept devices is limited at 10 - 1,000 Hz, probably due to charge trap states in the sputtered tunneling barrier. Because the fundamental hot carrier tunneling rate is less than a

picosecond, we expect that significant improvement may be obtained with better dielectric quality.

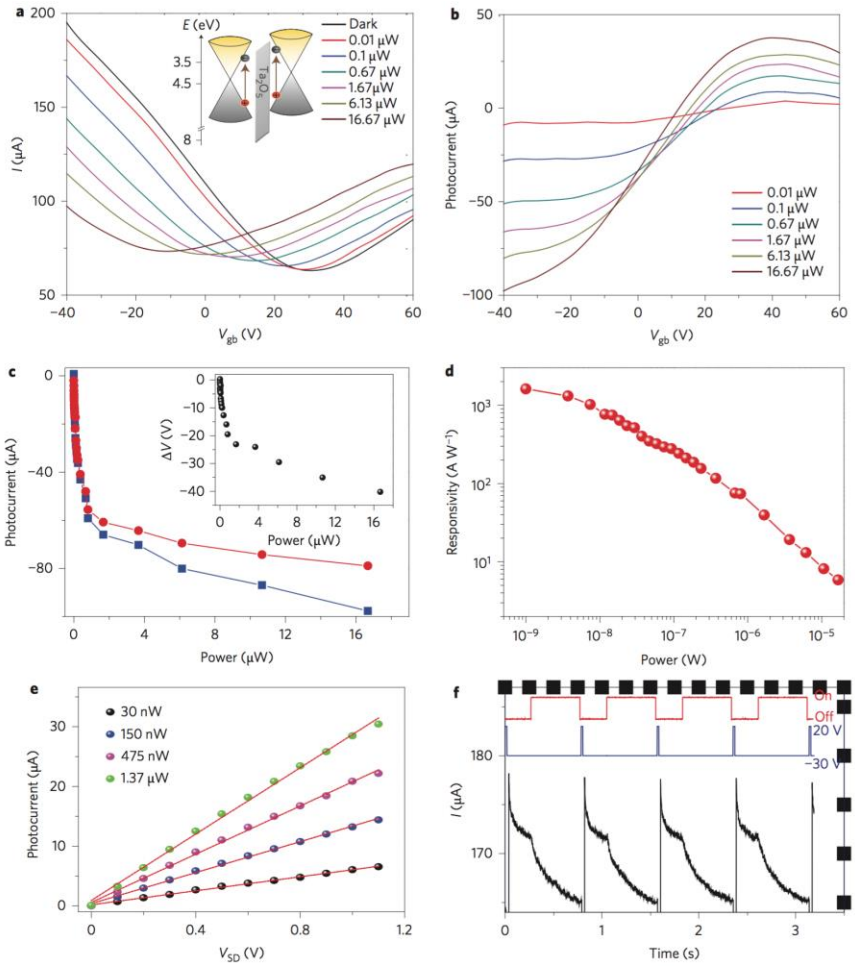


Figure 4-4 Photoresponse of the graphene double-layer heterostructures in the visible region. (a) I–$V_{gb}$ characteristics of the measured graphene photodetector under different laser powers. The potential of the top graphene layer was allowed to float, while the current of the bottom graphene transistor was measured under 1 V source–drain bias voltage. The laser wavelength is 532 nm with a spot size of 10 μm, covering the entire graphene photodetector. Inset: Energy band diagram of the graphene/$Ta_2O_5$/graphene heterostructures. (b) Gate dependence of photocurrent under different laser powers. (c) Power dependence of photocurrent at 240 V (blue squares) and 220 V (red circles) backgate voltages. Inset: Shift of Dirac point gate voltages as a function of illumination

power. (d) Measured photoresponsivity versus illumination power. (e) The magnitude of the photocurrent increases linearly with source–drain bias voltage of the bottom graphene layer transistor. Red lines are linear fits. $V_{gb}$ = 0 V. (f) Temporal photoresponse of the graphene photodetector (black curve). The illumination power is 0.3 μW and the laser wavelength is 532 nm. The laser on–off (red curve) is controlled by a mechanical shutter synchronized with the reset backgate voltage pulses (blue curve).

### 4.4.2 Photoresponse in Near- to Mid-Infrared Regime

The tunnel barrier height is a key parameter affecting device operation. To extend the range of high responsivity photodetection into the infrared regime we fabricated similar device structures, but incorporated intrinsic silicon as the tunnel barrier in place of the wide bandgap $Ta_2O_5$ layer, as shown in Figure 4-5(d) inset. The silicon conduction band is 0.5 eV above the Fermi level of intrinsic graphene [168], enabling tunneling of lower-energy electrons. The infrared photoresponses of the graphene/silicon/graphene heterostructures are similar to our previous measurements, displaying large shifts of the transfer curve and Dirac point voltage towards negative $V_{gb}$ with increasing illumination power. Figure 4-5(a)-(c) shows the extracted gate dependence of photocurrent under 1.3 μm, 2.1 μm, and 3.2 μm wavelength light illumination, respectively. The strong photo-gating effect and gate modulation of the photo-signal are again clearly observed in both near-infrared and mid-infrared regimes. Power-dependent photocurrent curves were extracted and plotted in Figure 4-5(d)-(f), respectively. Significantly, the near-infrared

responsivity of the device reaches 4 $AW^{-1}$ at $\lambda = 1.3$ μm and 1.9 $AW^{-1}$ at $\lambda = 2.1$ μm at room temperature. These values are more than three orders of magnitude higher than the responsivity of graphene/$Ta_2O_5$/graphene heterostructures at near-infrared wavelengths. Furthermore, our prototype graphene photodetector exhibits a room-temperature mid-infrared responsivity of 1.1 $AW^{-1}$ at $\lambda = 3.2$ μm (Figure 4-5(f)), rivalling state-of-the-art mid-infrared detectors without the need for cryogenic cooling.

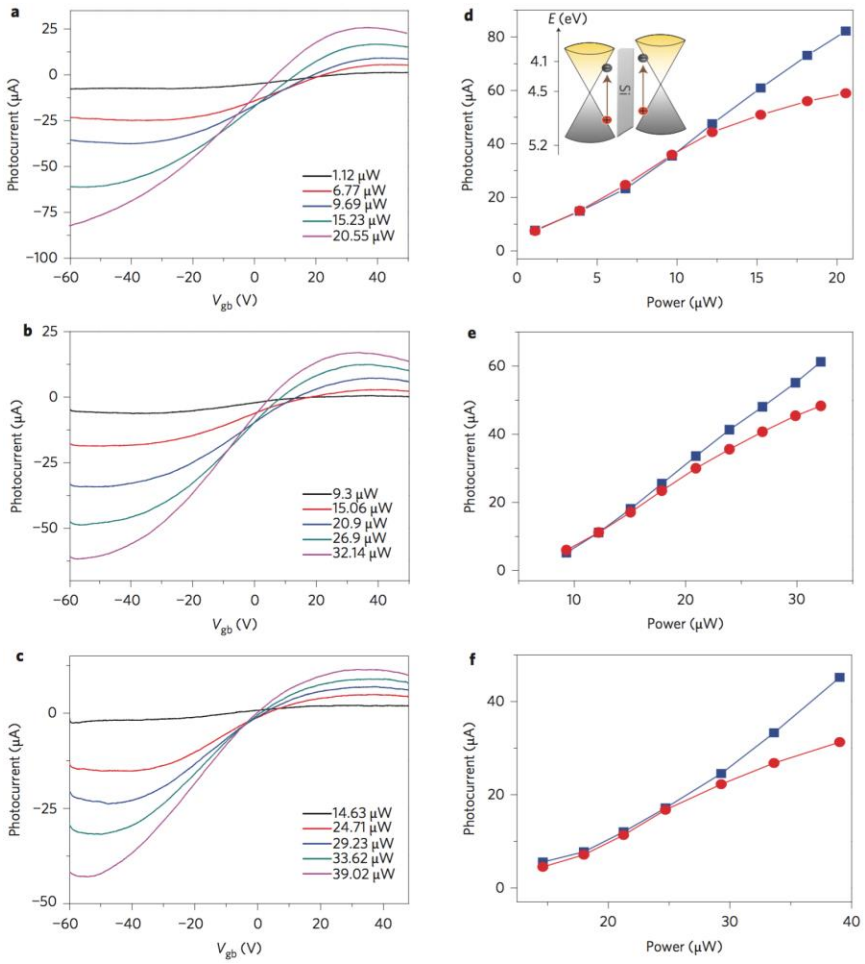


Figure 4-5 Near- to mid-infrared photoresponse of the graphene/silicon/graphene heterostructure photodetector. (a)-(c) Gate dependence of photocurrent under different

illumination powers with excitation wavelengths at 1.3 μm (a), 2.1 μm (b), and 3.2 μm (c). Measurements were conducted by applying 1.5 V bias voltage to the bottom graphene transistor, and the laser spots were focused to ~ 20 μm, covering the entire graphene photodetector. (d)-(f) Photocurrent versus illumination power under excitation wavelengths of 1.3 μm (d), 2.1 μm (e), and 3.2 μm (f). Representative curves with backgate voltages set at 260 V (blue squares) and 230 V (red circles) are shown. Inset in (d): band diagram of graphene/silicon/graphene heterostructures.

## 4.5 Conclusion

Hot carrier tunneling as a mechanism for photodetection in a graphene double-layer heterostructure provides a viable route for broadband and high sensitivity photodetection at room temperature. The photodetectors demonstrate room temperature photodetection from visible to mid-infrared range, with mid-infrared responsivity higher than 1 $AW^{-1}$, as required by most applications [169]. To further enhance device performance, the bottom graphene channel could be replaced with other thin-film semiconductors to reduce the background current. Furthermore, interlayer hot carrier tunneling and photo-gating could be enhanced by utilizing atomically thin two-dimensional (2D) semiconductors such as $MoS_2$ and $WS_2$ as the tunneling barrier layer [103].

# Chapter 5

# Graphene-SOI Heterojunction Broadband and High Responsivity Photodetectors

## 5.1 Introduction

In the previous chapter, photo-gating effect is introduced by the graphene double-layer structure sandwiched with sputtered dielectric/semiconductor, which serve as tunneling barrier between top and bottom asymmetric graphene energy band structures. Under optical illumination, photo-excited hot carriers generated in the absorption graphene layer tunnel through the heterojunction barrier into the channel silicon layer, leading to charges build-up in the absorption layer and resulting in the photo-gating effect on the channel conductance [33]. The photodetector shows impressive improvement compared with the first-introduced graphene photodetector [150], where photoresponsivity is more than six order of magnitude higher in visible regime. However, as shown in Figure 4-4(f), the photodetector on-off operation speed is within couple of seconds, which is resulting from the high-density defect states within the sputtered

dielectric/semiconductor tunneling barrier films. This inevitable amorphous nature of sputtered materials provides numerous photocarrier trapped states that not only slow down the photodetector on-off operation speed but also deteriorate the high photoresponsivity caused by photo-gating effect, more importantly, greatly limits and impedes the further development of such photodetectors in ultra-broadband and high responsivity image sensor array applications. In this regards, we propose a novel photodetector design based on graphene-SOI heterostructures, instead of using amorphous sputtered materials, utilizing the tunneling barrier naturally formed by the defect-free heterojunction interface between semi-metallic graphene and single crystalline silicon. In replacing of amorphous sputtered materials with the naturally formed heterojunction interface, we successfully reduce the photocarrier trapped states, not only boosting the photodetector on-off operation speed but also increasing the photoresponsivity with stronger photo-gating effect.

## 5.2 Graphene-SOI Heterojunction Photodetector

Starting with a silicon-on-insulator (SOI) wafer, we first fabricate a conventional bottom-gated silicon-on-insulator field-effect transistor (BG-SOI-FET) using the mature and well-developed silicon technology processes such as thermal oxidation, lithography,

reactive-ion etching (RIE), doping/diffusion, metal deposition, annealing. Then we transfer and pattern an isolated graphene film on top of exposed silicon channel, naturally forming a heterojunction barrier between semi-metallic graphene and semiconducting silicon. Figure 5-1 shows the cross-sectional view of our photodetector design. Here we utilize the heterojunction barrier in replacing of amorphous sputtered materials to successfully reduce photocarrier trapped states, not only boosting the photodetector on-off operation speed but also increasing the photoresponsivity with stronger photo-gating effect, which will be discussed later.

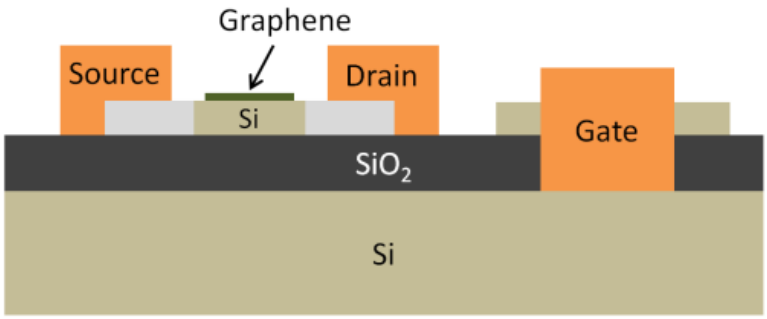


Figure 5-1 Cross-sectional view of graphene-SOI heterojunction photodetector.

### 5.3 Device I-V Characterization and Photodetection Measurement

We characterize the I-V characteristics of bottom-gated silicon-on-insulator field-effect transistor (BG-SOI-FET), as shown in Figure 5-2. Devices show turn-on threshold voltage close to zero, thus good for low power operation. In addition, the linear

and flat saturation I-$V_{ds}$ curves indicate the high quality and good control of the gate over the channel conductance.

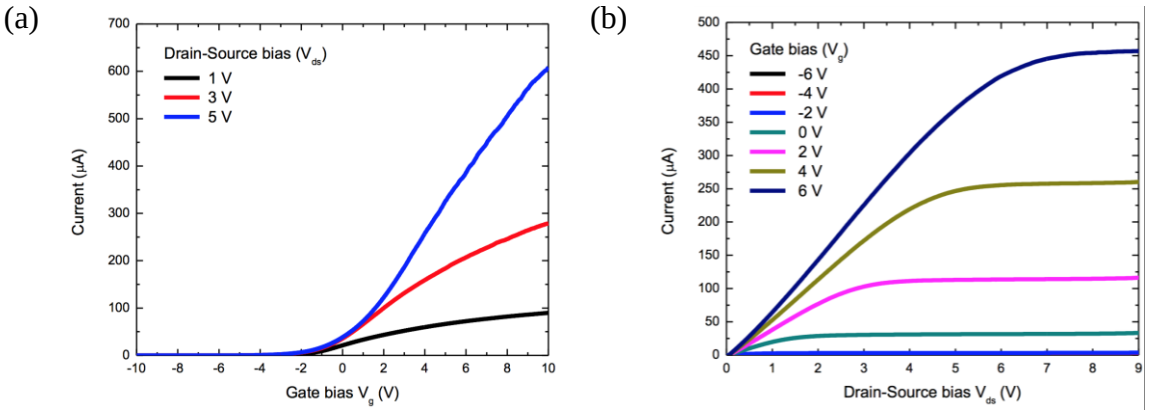


Figure 5-2 Characterization of bottom-gated silicon-on-insulator field-effect transistor (BG-SOI-FET). (a) I-$V_g$ transfer curves. (b) I-$V_{ds}$ linear and saturation characteristics.

Under optical illumination, photo-excited hot carriers generated in the top absorption graphene layer tunnel through the heterojunction barrier into the bottom channel silicon layer, leading to charges build-up in the absorption layer and a strong photo-gating effect on the channel conductance. We investigate this double-layer heterojunction photo-gating mechanism in our photodetector devices under the illumination of calibrated 1.2 μm wavelength pulse-laser from a custom-built optical parametric amplification (OPA) system. Specifically, the photon energy of incident light is lower than the absorption cut-off of silicon (~ 1.107 μm), which prevents other absorption pathways through

silicon and isolates the double-layer heterojunction photo-gating effect. Figure 5-3(a) shows the turn-on curves shift to left in response to the increasing incident laser power.

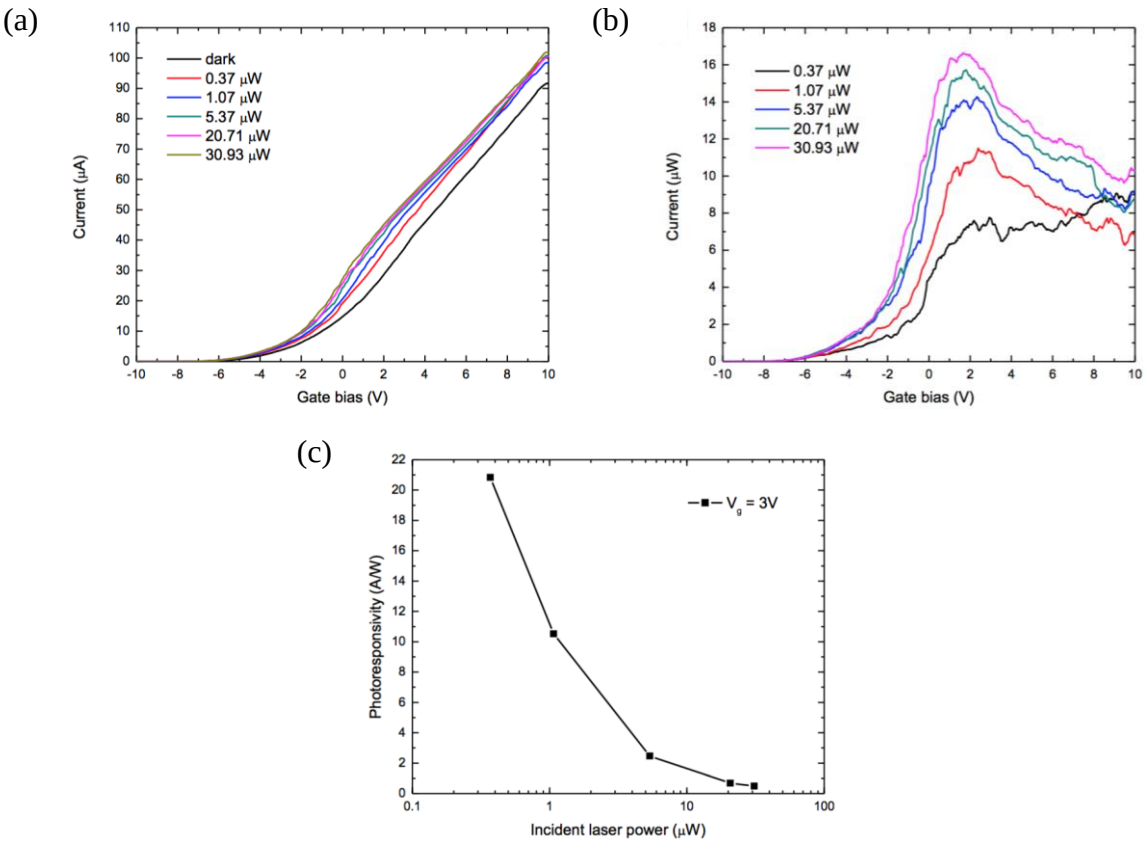


Figure 5-3 Near-infrared photodetection measurement of the graphene-SOI heterojunction photodetector. (a) I-$V_g$ transfer curves and (b) photocurrent under different laser power illumination. (c) Power dependence photoresponsivity.

Moreover, we can calculate the photocurrent under different laser power illumination by subtracting the dark current, as shown in Figure 5-3(b). Fixing the gate bias at 3 V, we can further calculate the power dependence photoresponsivity, as shown in

Figure 5-3(c). Our graphene-SOI heterojunction photodetector can achieve responsivity of more than 20 A/W, serving as an excellent building block for future image sensor array applications.

## 5.4 Conclusion

In order to improve the photodetector on-off operation speed as well as high photoresponsivity with stronger photo-gating effect, we successfully demonstrate a novel photodetector design based on graphene-SOI heterostructures, instead of using amorphous sputtered materials, utilizing the tunneling barrier naturally formed by the defect-free heterojunction interface between semi-metallic graphene and single crystalline silicon. The photodetector exhibits room temperature detection from visible to the near-infrared range, with near-infrared photoresponsivity higher than 20 A/W, sufficient for most applications [169]. Significantly, our result not only addresses the key challenge of slow response speed for conventional graphene-based phototransistor design but also showcases the promise of graphene-based photodetector integrated on silicon platform.

# Chapter 6

# All-Graphene Transparent Heterojunction Broadband Photodetectors for One-Dimensional Light-Field Ranging

## 6.1 Introduction

The light field is a vector function that describes the amount of light flowing in every direction through every point in space, which is a fundamental representation of light. In computer graphics, to produce a light-field views must be obtained for a large collection of viewpoints. Depending on the parameterization employed, this collection will typically span some portion of a line, circle, plane, sphere, other shape, or even the unstructured collections of viewpoints. As the computational power advanced, along with the rising demand of higher resolution and higher dimensionality in terms of viewpoints and angels in every aspects, devices and instruments that are capable of capturing photographically light-field information have been intensively studied for the past decade, including a robotically controlled camera (Levoy 2002), an arc of cameras, a dense array of cameras (Kanade 1998; Yang 2002; Wilburn 2005), handheld cameras (Ng 2005;

Georgiev 2006; Marwah 2013), microscopes (Levoy 2006), or other optical system (Bolles 1987). However, all these techniques are limited and relied on the conventional non-transparent two-dimensional (2D) image sensor array, which requires either precise mechanical control of optical components or delicate/complex microlens array comprised of many thousands of microscopic lenses to achieve light-field imaging. In this regards, we propose a transparent photodetector design based on multilayer graphene heterostrucures, using transparent graphene films (~ 97.7 %) as not only the conduction channel and the light absorption layer (utilizing heterojunction photo-gating effect) but also the gate-biasing layer. Due to the all-graphene heterostructure design, the photodetector is highly transparent. With proper stacking along the light propagation direction, all-graphene transparent heterojunction photodetectors may serve as excellent building blocks for future development of three-dimensional (3D) image sensor array and light-field ranging.

## 6.2 All-Graphene Transparent Heterojunction Photodetector

The schematic of our all-graphene transparent heterojunction photodetector is shown in Figure 6-1(a). On transparent glass substrate, we repeatedly transfer/pattern graphene then put down metal contacts for three times with conventional photolithography

processes, serving as bottom gate, middle channel, and top absorption layer respectively. Between bottom gate and middle channel, we deposit 40 nm $Al_2O_3$ with atomic layer deposition (ALD) technique; between middle channel and top absorption layer, we sputter 6 nm $Ta_2O_5$ instead. Here we deposit different dielectrics between graphene layers in order to make high performance bottom-gated (BG) field-effect transistor (FET) incorporated with double-layer graphene heterojunction on top, utilizing the photo-gating effect for high responsivity photodetection. Figure 6-1(b) shows the actual fabricated all-graphene transparent heterojunction photodetectors on a sheet of paper with Univ. of Michigan "M" logo printout. With our bare eyes, we can obviously see through the whole device and confirm its high transparency, except some metal pads for measurement wire-bonding purpose.

(a) (b)

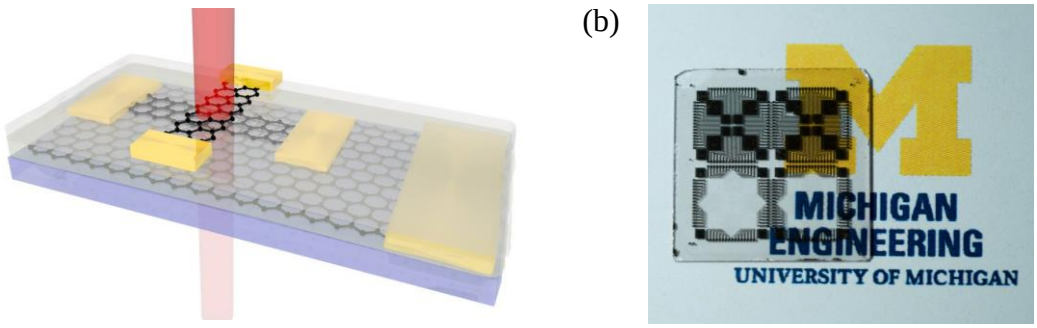


Figure 6-1 (a) The schematic of all-graphene transparent heterojunction photodetector. (b) Actual fabricated all-graphene transparent heterojunction photodetectors on a sheet of paper with Univ. of Michigan "M" logo printout.

## 6.3 Broadband Photodetection Characterization

We further investigate the broadband photodetection capability of the all-graphene transparent heterojunction photodetectors, under the illumination of calibrated pulse-laser at 1.2 μm (signal) and 2.4 μm (idler) wavelength from custom-built optical parametric amplification (OPA) system, which is well maintained and operated in Prof. Norris lab at the University of Michigan.

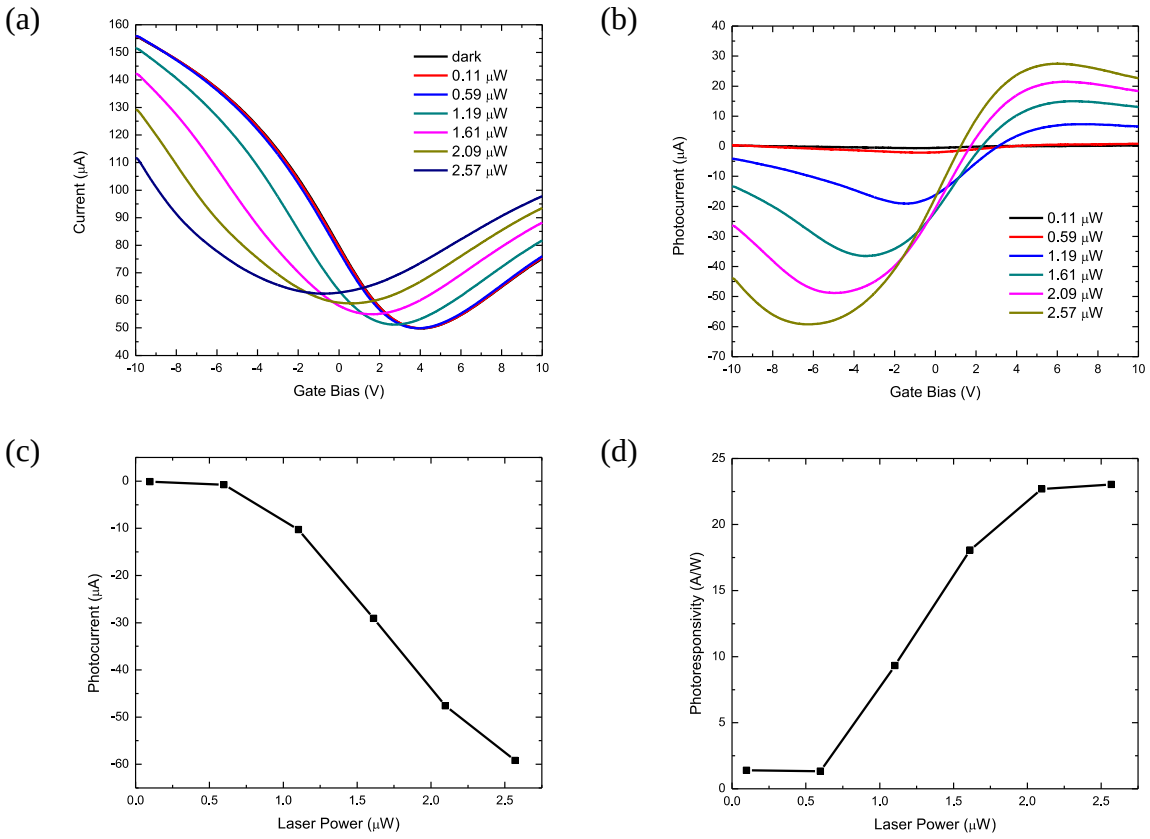


Figure 6-2 Photoresponse characterization of the all-graphene transparent heterojunction photodetector at 1.2 μm wavelength (signal). (a) I-$V_g$ transfer curves and (b) photocurrents under different laser power illumination. (c)(d) Laser power dependence photocurrent (c) and photoresponsivitiy (d) at gate bias ($V_g$) of -6 V.

We first examine the photoresponse at 1.2 μm wavelength (signal). Figure 6-2(a) shows the transfer curves under different laser power illumination and the Dirac points shift to the left in response to the increasing incident laser power. We calculate the photocurrents under different laser power illumination by subtracting the dark current from laser-on current, as shown in Figure 6-2(b). The photocurrents flip signs when sweeping through the Dirac points, which indicates the n-doping of the channel by the photo-gating effect. This phenomenon confirms the proposed asymmetric band diagram schematic shown in Figure 4-2(a), which is resulted from the stronger environmental p-doping of the exposed top graphene layer. We also calculate the laser power dependence photocurrent and photoresponsivity, as shown in Figure 6-2(c) and Figure 6-2(d) where we fix the gate bias ($V_g$) at -6 V. The maximum photoresponsivity at 1.2 μm wavelength (signal) can be achieved more than 20 A/W.

We also examine the photoresponse at 2.4 μm wavelength (idler). Figure 6-3(a) and Figure 6-3(b) shows the transfer curves and corresponding photocurrents under different laser power respectively. Compared with the curves for 1.2 μm wavelength (signal), the Dirac points also shift to the left in response to the increasing incident laser power. However, the photoresponse is greatly reduced, which agrees with the fact that graphene' light absorption rate decreases as the wavelength increases. Figure 6-3(c) and Figure

6-3(d) shows the laser power dependence photocurrent and photoresponsivity at gate bias ($V_g$) of -7 V. The maximum photoresponsivity at 2.4 μm wavelength (idler) can be achieved more than 0.45 A/W.

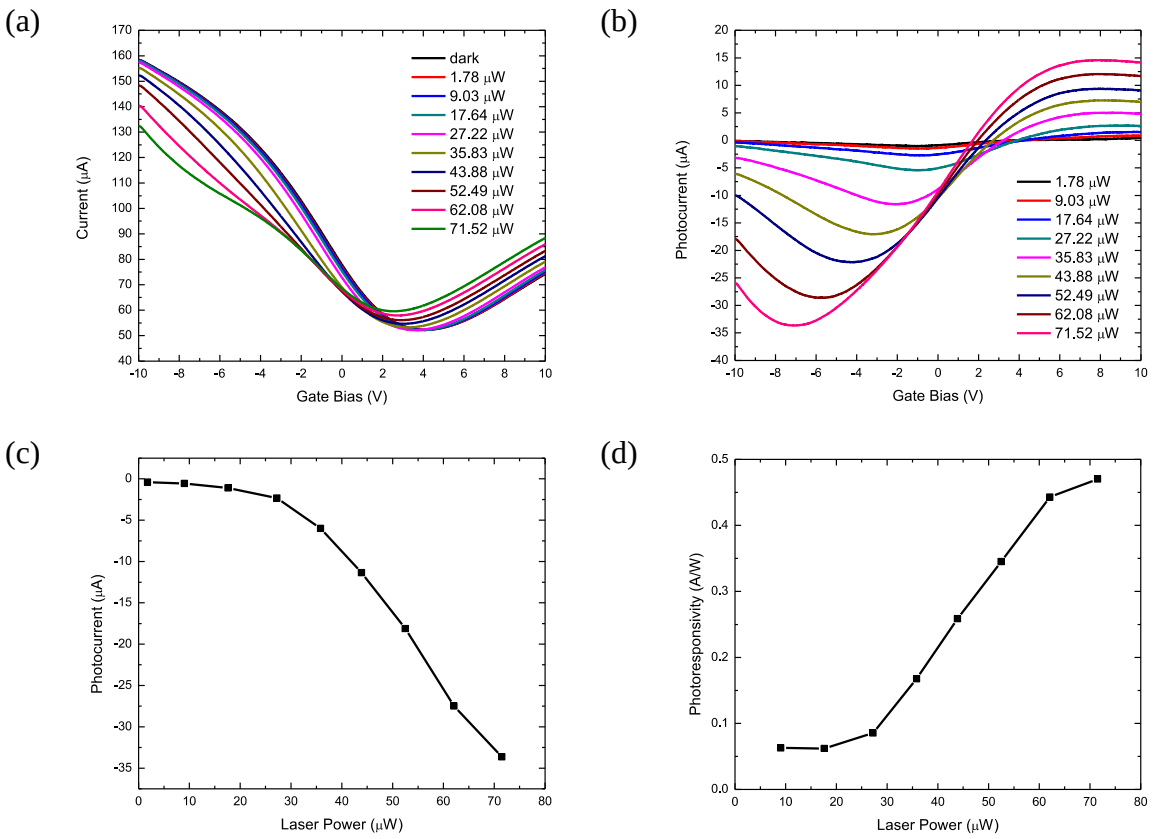


Figure 6-3 Photoresponse characterization of the all-graphene transparent heterojunction photodetector at 2.4 μm wavelength (idler). (a) I-$V_g$ transfer curves and (b) photocurrents under different laser power illumination. (c)(d) Laser power dependence photocurrent (c) and photoresponsivitiy (d) at gate bias ($V_g$) of -7 V.

## 6.4 One-Dimensional Light-Field Ranging

Due to the high transparency of our all-graphene heterojunction photodetector

design, we can easily surpass the limitation of conventional non-transparent image sensor array and successfully achieve light-field photodetection for ranging application by properly stacking photodetector devices along the light propagation direction. Figure 6-4(a) and Figure 6-4(b) show the cross-sectional and top-down views of two stacking all-graphene transparent heterojunction broadband photodetectors respectively.

(a)

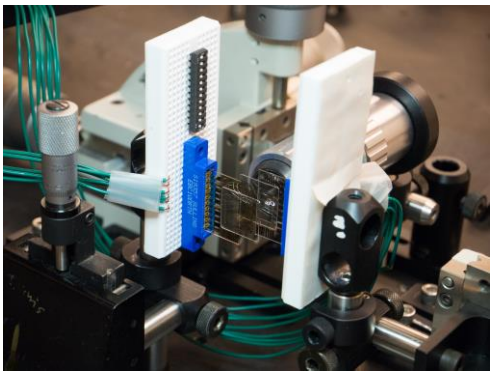

(b)

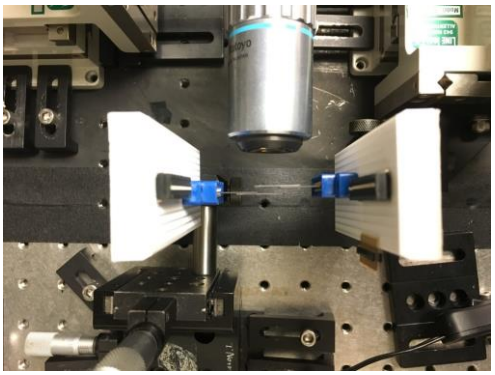

(c)

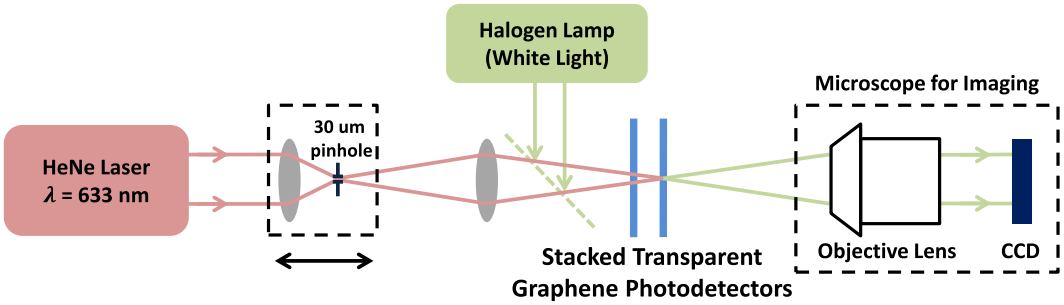


Figure 6-4 (a)(b) Cross-sectional (a) and top-down (b) views of two stacking all-graphene transparent heterojunction broadband photodetectors along the light propagation direction. (c) Schematic of one-dimensional (1D) light-field photodetection optical imaging system.

Figure 6-4(c) shows the schematic of the proof-of-concept one-dimensional (1D) light-field photodetection optical imaging system. We use helium-neon (HeNe) CW laser

with 632.8 nm wavelength for illumination in visible regime. A 30 μm pinhole is used to serve as our point source image object and construct a one-to-one image projection onto the stacked transparent photodetectors. In order to achieve high power illumination, we place a focusing lens in front of the 30 μm pinhole to ensure most of the beam profile can pass through. We also build a microscope imaging system with halogen lamp (white light) to help determine the light propagation, beam focus and the position of photodetectors. As we move the 30 μm pinhole with the focusing lens along the light propagation direction, we can precisely manipulate the beam profile and control beam spot to be focused on any device planes. With two individual x-y-z translation stages, we separate two individual transparent photodetectors by 2 mm distance, serving as focal plane 1 and 2 respectively, then measure the photoresponse of two individual transparent photodetectors while we control the focused beam spot position moving between two focal planes. Here we define 10 beam focusing positions: position #1 is on focal plane 1; position #10 is on focal plane 2; and position #2 to #9 are equal-space distributed in between. Figure 6-5(a) and Figure 6-5(b) shows the photoresponse curves for two individual transparent photodetectors on focal plane 1 (focusing position #1) and focal plane 2 (focusing position #10) respectively. We also calculate the photocurrents by subtracting the dark current from laser-on current for 10 different focusing positions, as

shown in Figure 6-5(c) and Figure 6-5(d).

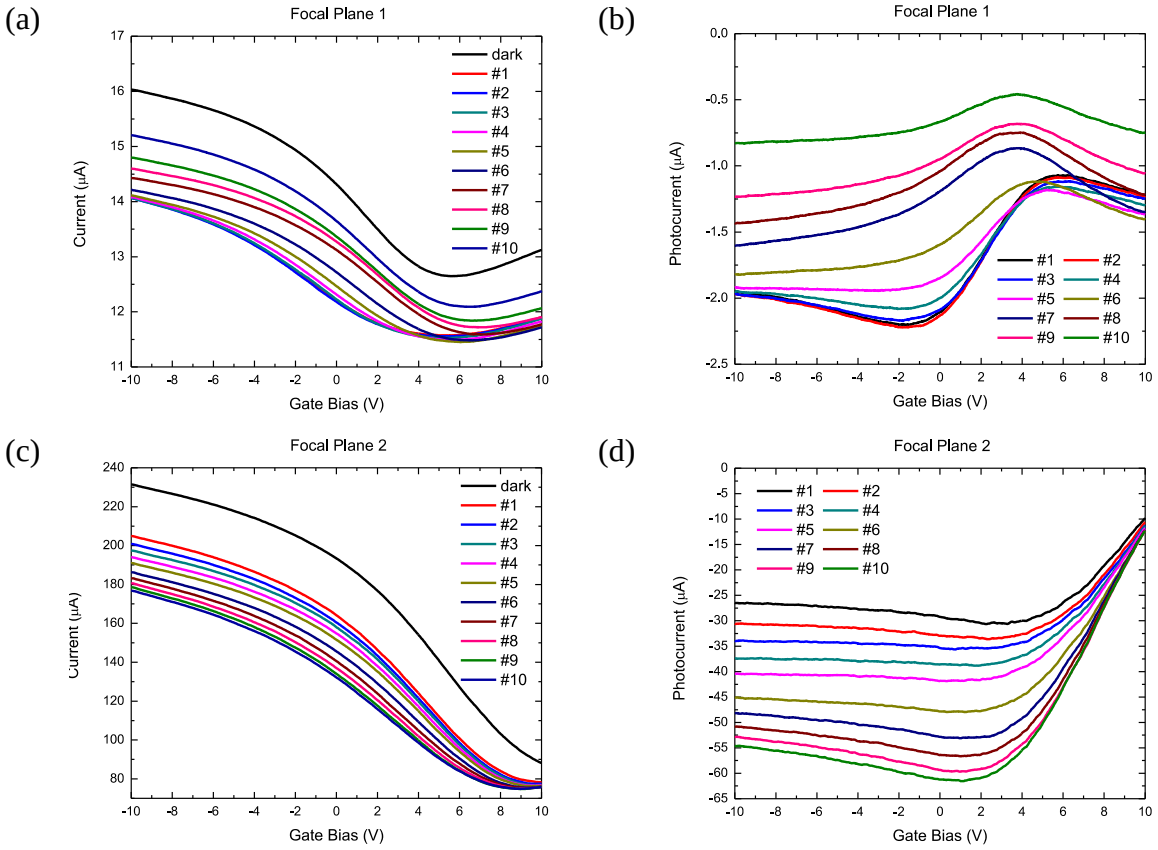


Figure 6-5 (a)(b) Transfer curve (a) and photocurrent (b) for the detector on focal plane 1 (focusing position #1). (c)(d) Transfer curve (c) and photocurrent (d) for the detector on focal plane 2 (focusing position #10).

According to the plots, for the transparent photodetector on focal plane 1 (focusing position #1), photoresponse decreased as the beam focusing position moves from #1 to #10, which indicates the focused beam spot goes from most focused to the most out-of-focus position. On the contrary, for the transparent photodetector on focal plane 2

(focusing position #10), photoresponse increased instead as the beam focusing position moves from #1 to #10, which indicates the beam spot goes from most out-of-focus to the most focused position. Here, we can clearly observe the photoresponse shows totally opposite trends as the beam focusing position moves from #1 to #10, but they always increase monotonically as the beam spot goes from the most out-of-focus to the most focused position, which agrees with our expectations.

To further interpret the trends, we fix the gate bias ($V_g$) at -5 V and extract the data points for both transparent photodetectors, then replot according to the focusing positions, as shown in Figure 6-6. From the plot, we can strongly conclude that, as the focused beam spot moves from position #1 to #10, the absolute photocurrent for the detector on focal plane 1 decreases (in response to the focused beam spot movement from the most focused to the most out-of-focus condition) while the photocurrent for the detector on focal plane 2 increases (in response to the focused bean spot movement from the most out-of-focus to the most focused condition). Based on this unique opposite trends from stacked transparent photodetectors, we can certainly go further and demonstrate three-dimensional (3D) light-field applications. For example, with proper design of optical camera imaging system and transparent photodetectors, we can easily detect the object moving away from the imaging system if the photocurrent of the detector on plane

1 increases while the detector on plane 2 decreases, vice versa. That is, we can utilize the opposite photocurrent trends from transparent detectors to determine the movement, speed and even acceleration of an object, which is so-called the light-field ranging. Here we successfully demonstrate the proof-of-concept one-dimensional (1D) light-field ranging with only two individual transparent photodetectors. We believe, with more photodetectors on the stacked focal planes, we can even approach not only the light-field ranging in more dimensionality but also more light-field applications in the future.

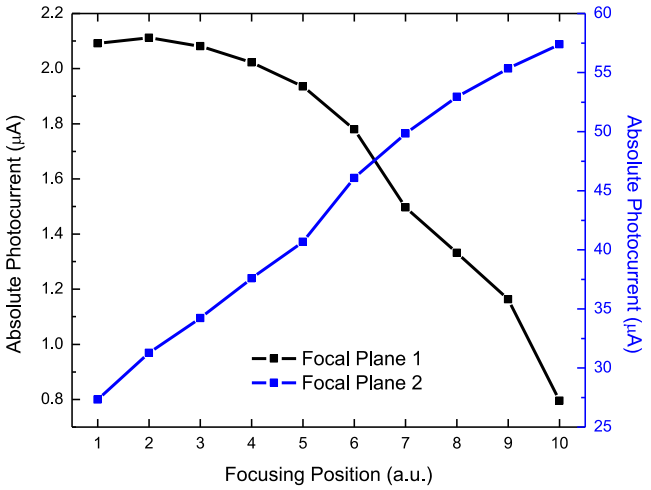


Figure 6-6 Photocurrent versus laser beam focusing position at gate bias ($V_g$) of -5 V for two individual all-graphene transparent heterojunction photodetectors placed along the light propagation direction separated by 2 mm distance.

## 6.5 Conclusion

In order to surpass the limitation of conventional non-transparent two-dimensional

(2D) image sensor array and achieve light-field imaging, we successfully demonstrate a transparent photodetector design based on multilayer graphene heterostrucures, using transparent graphene films (~ 97.7 %) as not only the conduction channel and the light absorption layer (utilizing heterojunction photo-gating effect) but also the gate-biasing layer. Due to the all-graphene heterostructure design, the photodetector is highly transparent. In addition, the near-infrared photoresponsivity of the all-graphene transparent heterojunction photodetector can be achieved more than 20 A/W at 1.2 μm wavelength (signal) and 0.45 A/W at 2.4 μm wavelength (idler) respectively. With proper stacking of two individual all-graphene transparent heterojunction photodetectors along the light propagation direction, we successfully demonstrate the proof-of-concept one-dimensional (1D) light-field ranging, which can certainly be utilized to determine the movement of an image object. Furthermore, we believe, with more photodetectors on the stacked planes, our all-graphene transparent heterojunction broadband photodetectors serve as excellent building blocks to approach not only the light-field ranging in more dimensionality but also more light-field applications in the future.

# Chapter 7

# Conclusions and Future Work

## 7.1 Conclusions

In this thesis, we have demonstrated several novel nanostructure and transistor designs for both electrical and optical applications by exploiting graphene's unique properties.

Firstly, we demonstrate the dual-gate graphene ambipolar transistors with capability of operating under both common and differential modes to realize signal amplification within one single device, which is not possible in the conventional silicon-based amplifier circuit configuration. In addition, a common-mode rejection ratio (CMRR) over 80 dB can be achieved, making it possible for future low noise circuit applications.

Secondly, we demonstrate the hyperbolic metamaterials (HMMs) by using precisely controlled periodic graphene-dielectric multilayer nanostructures with proper chemical doping. The graphene HMMs have an optical topological transition at a wavelength of 4.5 μm and maintain good hyperbolic properties up to 8 μm. Moreover, we also realize

the graphene HMMs with the same structure except that the graphene layers are not chemically doped, resulting in a transition wavelength red-shifted to 7.2 μm.

Thirdly, we demonstrate the graphene-SOI heterojunction photodetectors to improve the device on-off operation speed as well as strengthen the photo-gating effect. Instead of using amorphous sputtered materials, utilizing the tunneling barrier naturally formed by the defect-free heterojunction interface between semi-metallic graphene and single crystalline silicon. The photodetector exhibits room temperature detection from visible to the near-infrared range, with near-infrared photoresponsivity higher than 20 A/W. This result not only addresses the key challenge of slow response speed for conventional graphene-based phototransistor design but also showcases the promise of graphene-based photodetector integrated on silicon platform.

Lastly, we demonstrate the all-graphene transparent broadband photodetectors based on multilayer graphene heterostrucures in order to surpass the limitation of non-transparent two-dimensional (2D) image sensor array and achieve light-field imaging. The near-infrared photoresponsivity can be achieved more than 20 A/W at 1.2 μm wavelength (signal) and 0.45 A/W at 2.4 μm wavelength (idler) respectively. With proper stacking of two individual all-graphene transparent heterojunction photodetectors along the light propagation direction, we successfully demonstrate the proof-of-concept

one-dimensional (1D) light-field ranging, which can certainly be utilized to determine the movement, speed and even acceleration of an object. Furthermore, we believe, with more photodetectors on the stacked planes, our all-graphene transparent heterojunction broadband photodetectors serve as excellent building blocks to approach not only light-field ranging in more dimensionality but also more light-field applications in the future.

## 7.2 Future Work

Based on the research studies being discussed in this thesis, they certainly serve as the solid foundation and enable several interesting/promising topics worthy of further investigation and exploration.

### 7.2.1 Graphene-SOI Heterojunction Photodetector Image Sensor Array

In Chapter 5, we propose and successfully demonstrate a novel photodetector design based on graphene-SOI heterostructures. In replacing of amorphous sputtered materials with the naturally formed defect-free heterojunction interface between semi-metallic graphene and single crystalline silicon, we successfully reduce the photocarrier trapped states, not only boosting the photodetector on-off operation speed but also increasing the

photoresponsivity with stronger photo-gating effect. The single-pixel photodetector exhibits room temperature detection from visible to the near-infrared range, with near-infrared photoresponsivity higher than 20 A/W.

With those promising results, we continue to fabricate a 32 x 32 photodetector array by arranging pixels to share sources in row and drains in column with a global bottom gate. Figure 7-1(a) shows two 32 x 32 photodetector arrays fabricated on SOI wafer and Figure 7-1(b) shows the SEM image of graphene-SOI heterojunction photodetectors in array matrix arrangement. The array is then wire-bonded onto a chip carrier (Spectrum LCC 8423), as shown in Figure 7-1(c), mounted on a custom designed PCB board with four digital to analog converters (DACs), which can provide 0-5 V independently. Moreover, there are 16 matrix switches on board designed to perform 32 x 32 routing and the matrix data can be collected using a 12-bit analog to digital converter (ADC). The integrated system is controlled by a Spartan 6 XC6SLX9 field-programmable gate array (FPGA) through programming tools as Python (array operation and image readout) and $C^{++}$ (architecture and PCB/FPGA control). Due to the clean heterojunction interface between graphene and single crystalline silicon, each pixel's photoresponse can be individually read out at less than 1 millisecond, limited only by the external readout circuitry. Now we are working on building an optical projection setup with the optical

parametric amplification (OPA) system, trying to demonstrate the array image readout and characterization as well as further possible applications.

(a) (b)

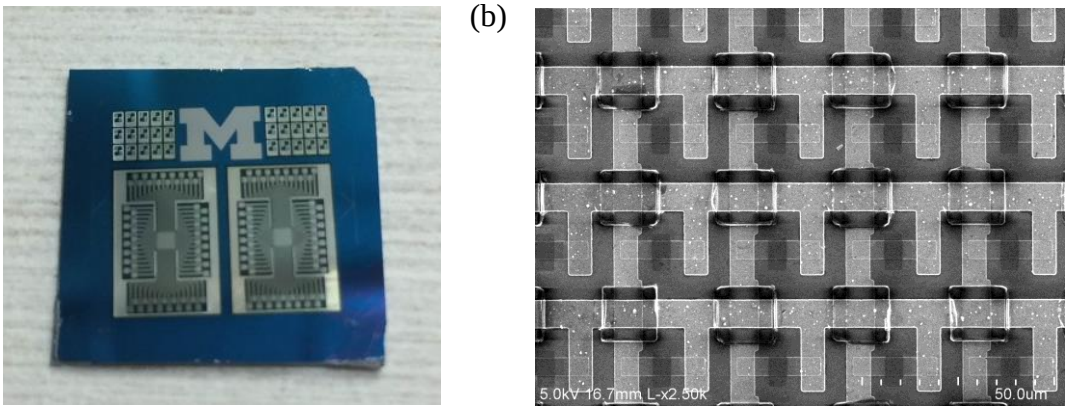


(c)

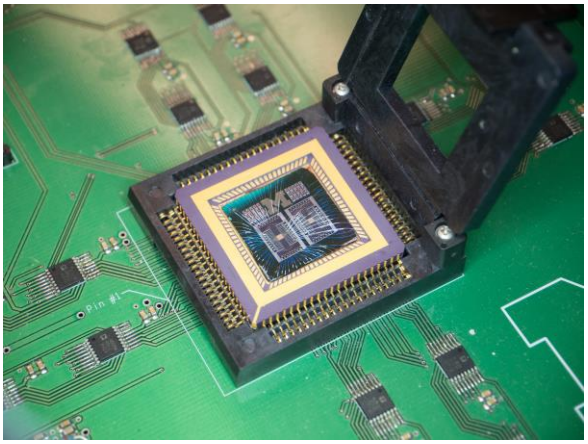

Figure 7-1 (a) Top view of thirty single-pixel devices and two 32 x 32 photodetector arrays fabricated on SOI wafer. (b) The SEM image of graphene-SOI heterojunction photodetectors in array matrix arrangement. (c) Integration of a 32 x 32 array wire-bonded onto a chip carrier mounted on a custom designed PCB board with 4 DACs, 16 matrix switches and a 12-bit ADC.

### 7.2.2 All-Graphene Transparent Photodetector for Light-Field Imaging

In Chapter 6, we propose and successfully demonstrate a transparent photodetector

design based on multilayer graphene heterostrucures in order to surpass the limitation of non-transparent two-dimensional (2D) image sensor array and achieve light-field imaging. Moreover, the near-infrared photoresponsivity of the all-graphene transparent heterojunction photodetector can be achieved more than 20 A/W at 1.2 μm wavelength (signal) and 0.45 A/W at 2.4 μm wavelength (idler) respectively. With proper stacking of two individual all-graphene transparent heterojunction photodetectors along the light propagation direction, we successfully demonstrate the proof-of-concept one-dimensional (1D) light-field ranging, which can certainly be utilized to determine the movement, speed and even acceleration of an object.

With those promising results, we would definitely like to explore its possibilities in more dimensionality. Figure 7-2 shows the schematic of the optical measurement setup with optical parametric amplification (OPA) system, where we can produce and project images from hollowed Cr-patterned masks onto the stacked photodetector arrays. We can directly measure the projected images at different focal plane, which is totally not allowed with conventional non-transparent two-dimensional (2D) image sensor array. All in all, we believe, with more photodetectors on the stacked planes, our all-graphene transparent heterojunction broadband photodetectors serve as excellent building blocks to approach not only light-field ranging in more dimensionality but also more light-field

applications, especially three-dimensional (3D) imaging, in the future.

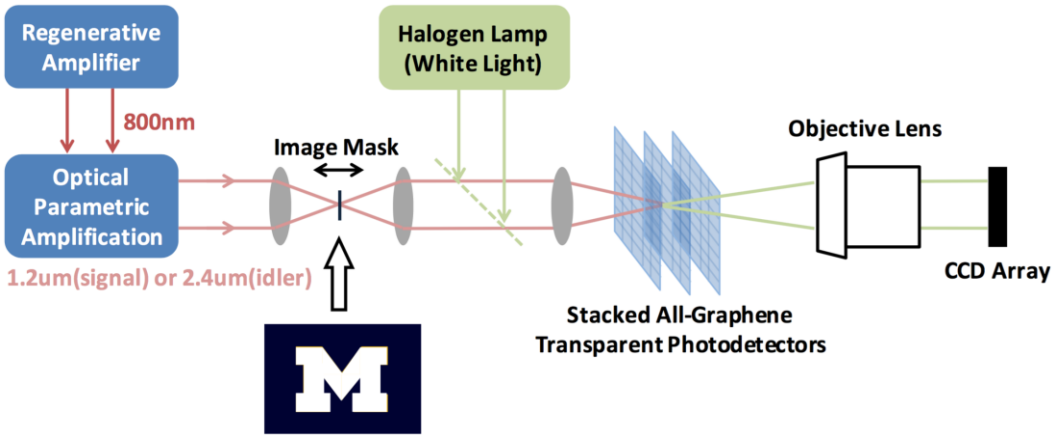


Figure 7-2 Schematic of an optical parametric amplification (OPA) system setup for light-field photodetection with stacked all-graphene transparent heterojunction photodetector arrays along the light propagation direction.

# Bibliography


[1] Y. Li, F. Qian, J. Xiang, and C. M. Lieber, "Nanowire electronic and optoelectronic devices," *Mater. Today*, vol. 9, no. 10, pp. 18–27, Oct. 2006.

[2] M. Grundmann, *Nano-Optoelectronics: Concepts, Physics and Devices*. Springer Science & Business Media, 2002.

[3] G. Konstantatos and E. H. Sargent, "Nanostructured materials for photon detection," *Nat. Nanotechnol.*, vol. 5, no. 6, pp. 391–400, Jun. 2010.

[4] R. W. Kelsall, I. W. Hamley, and rk Geoghegan, Eds., "Front Matter," in *Nanoscale Science and Technology*, John Wiley & Sons, Ltd, 2005, pp. i–xvi.

[5] W. Lu and C. M. Lieber, "Nanoelectronics from the bottom up," *Nat. Mater.*, vol. 6, no. 11, pp. 841–850, Nov. 2007.

[6] K. S. Novoselov, A. K. Geim, S. V. Morozov, D. Jiang, Y. Zhang, S. V. Dubonos, I. V. Grigorieva, and A. A. Firsov, "Electric Field Effect in Atomically Thin Carbon Films," *Science*, vol. 306, no. 5696, pp. 666–669, Oct. 2004.

[7] A. K. Geim and K. S. Novoselov, "The rise of graphene," *Nat. Mater.*, vol. 6, no. 3, pp. 183–191, Mar. 2007.

[8] A. H. Castro Neto, F. Guinea, N. M. R. Peres, K. S. Novoselov, and A. K. Geim, "The electronic properties of graphene," *Rev. Mod. Phys.*, vol. 81, no. 1, pp. 109–162, Jan. 2009.

[9] A. Dato, Z. Lee, K.-J. Jeon, R. Erni, V. Radmilovic, T. J. Richardson, and M. Frenklach, "Clean and highly ordered graphene synthesized in the gas phase," *Chem. Commun.*, no. 40, pp. 6095–6097, Oct. 2009.

[10] P. R. Wallace, "The Band Theory of Graphite," *Phys. Rev.*, vol. 71, no. 9, pp. 622–634, May 1947.

[11] J. W. McClure, "Diamagnetism of Graphite," *Phys. Rev.*, vol. 104, no. 3, pp. 666–671, Nov. 1956.

[12] M. Freitag, "Graphene: Nanoelectronics goes flat out," *Nat. Nanotechnol.*, vol. 3, no. 8, pp. 455–457, Aug. 2008.

[13] X. Du, I. Skachko, A. Barker, and E. Y. Andrei, "Approaching ballistic transport in

suspended graphene," *Nat. Nanotechnol.*, vol. 3, no. 8, pp. 491–495, Aug. 2008.

[14] S. V. Morozov, K. S. Novoselov, M. I. Katsnelson, F. Schedin, D. C. Elias, J. A. Jaszczak, and A. K. Geim, "Giant Intrinsic Carrier Mobilities in Graphene and Its Bilayer," *Phys. Rev. Lett.*, vol. 100, no. 1, p. 016602, Jan. 2008.

[15] K. S. Novoselov, A. K. Geim, S. V. Morozov, D. Jiang, M. I. Katsnelson, I. V. Grigorieva, S. V. Dubonos, and A. A. Firsov, "Two-dimensional gas of massless Dirac fermions in graphene," *Nature*, vol. 438, no. 7065, pp. 197–200, Nov. 2005.

[16] K. I. Bolotin, K. J. Sikes, Z. Jiang, M. Klima, G. Fudenberg, J. Hone, P. Kim, and H. L. Stormer, "Ultrahigh electron mobility in suspended graphene," *Solid State Commun.*, vol. 146, no. 9–10, pp. 351–355, Jun. 2008.

[17]K. Nomura and A. H. MacDonald, "Quantum Transport of Massless Dirac Fermions," *Phys. Rev. Lett.*, vol. 98, no. 7, p. 076602, Feb. 2007.

[18] E. H. Hwang and S. Das Sarma, "Acoustic phonon scattering limited carrier mobility in two-dimensional extrinsic graphene," *Phys. Rev. B*, vol. 77, no. 11, p. 115449, Mar. 2008.

[19]F. Schedin, A. K. Geim, S. V. Morozov, E. W. Hill, P. Blake, M. I. Katsnelson, and K. S. Novoselov, "Detection of individual gas molecules adsorbed on graphene," *Nat. Mater.*, vol. 6, no. 9, pp. 652–655, Sep. 2007.

[20] M. I. Katsnelson and A. K. Geim, "Electron scattering on microscopic corrugations in graphene," *Philos. Trans. R. Soc. Lond. Math. Phys. Eng. Sci.*, vol. 366, no. 1863, pp. 195–204, Jan. 2008.

[21] J.-H. Chen, C. Jang, S. Xiao, M. Ishigami, and M. S. Fuhrer, "Intrinsic and extrinsic performance limits of graphene devices on SiO2," *Nat. Nanotechnol.*, vol. 3, no. 4, pp. 206–209, Apr. 2008.

[22] L. A. Falkovsky and A. A. Varlamov, "Space-time dispersion of graphene conductivity," *Eur. Phys. J. B*, vol. 56, no. 4, pp. 281–284, May 2007.

[23] L. A. Falkovsky and S. S. Pershoguba, "Optical far-infrared properties of a graphene monolayer and multilayer," *Phys. Rev. B*, vol. 76, no. 15, p. 153410, Oct. 2007.

[24] T. Stauber, N. M. R. Peres, and A. K. Geim, "Optical conductivity of graphene in the visible region of the spectrum," *Phys. Rev. B*, vol. 78, no. 8, p. 085432, Aug. 2008.

[25] S. A. Mikhailov and K. Ziegler, "New Electromagnetic Mode in Graphene," *Phys. Rev. Lett.*, vol. 99, no. 1, p. 016803, Jul. 2007.

[26] I. V. Iorsh, I. S. Mukhin, I. V. Shadrivov, P. A. Belov, and Y. S. Kivshar, "Hyperbolic metamaterials based on multilayer graphene structures," *Phys. Rev. B*, vol. 87, no. 7, p. 075416, Feb. 2013.

[27] Y.-C. Chang, C.-H. Liu, C.-H. Liu, Z. Zhong, and T. B. Norris, "Extracting the

complex optical conductivity of mono- and bilayer graphene by ellipsometry," *Appl. Phys. Lett.*, vol. 104, no. 26, p. 261909, Jun. 2014.

[28] M. Jablan, H. Buljan, and M. Soljačić, "Plasmonics in graphene at infrared frequencies," *Phys. Rev. B*, vol. 80, no. 24, p. 245435, Dec. 2009.

[29] S. H. Mousavi, I. Kholmanov, K. B. Alici, D. Purtseladze, N. Arju, K. Tatar, D. Y. Fozdar, J. W. Suk, Y. Hao, A. B. Khanikaev, R. S. Ruoff, and G. Shvets, "Inductive Tuning of Fano-Resonant Metasurfaces Using Plasmonic Response of Graphene in the Mid-Infrared," *Nano Lett.*, vol. 13, no. 3, pp. 1111–1117, Mar. 2013.

[30] H. Yan, X. Li, B. Chandra, G. Tulevski, Y. Wu, M. Freitag, W. Zhu, P. Avouris, and F. Xia, "Tunable infrared plasmonic devices using graphene/insulator stacks," *Nat. Nanotechnol.*, vol. 7, no. 5, pp. 330–334, May 2012.

[31] Z. Q. Li, E. A. Henriksen, Z. Jiang, Z. Hao, M. C. Martin, P. Kim, H. L. Stormer, and D. N. Basov, "Dirac charge dynamics in graphene by infrared spectroscopy," *Nat. Phys.*, vol. 4, no. 7, pp. 532–535, Jul. 2008.

[32] F. Bonaccorso, Z. Sun, T. Hasan, and A. C. Ferrari, "Graphene photonics and optoelectronics," *Nat. Photonics*, vol. 4, no. 9, pp. 611–622, Sep. 2010.

[33] C.-H. Liu, Y.-C. Chang, T. B. Norris, and Z. Zhong, "Graphene photodetectors with ultra-broadband and high responsivity at room temperature," *Nat. Nanotechnol.*, vol. 9, no. 4, pp. 273–278, Apr. 2014.

[34] Y.-C. Chang, C.-H. Liu, C.-H. Liu, S. Zhang, S. R. Marder, E. E. Narimanov, Z. Zhong, and T. B. Norris, "Realization of mid-infrared graphene hyperbolic metamaterials," *Nat. Commun.*, vol. 7, p. 10568, Feb. 2016.

[35] A. M. DaSilva, Y.-C. Chang, T. Norris, and A. H. MacDonald, "Enhancement of photonic density of states in finite graphene multilayers," *Phys. Rev. B*, vol. 88, no. 19, p. 195411, Nov. 2013.

[36] W. Shockley and H. J. Queisser, "Detailed Balance Limit of Efficiency of p-n Junction Solar Cells," *J. Appl. Phys.*, vol. 32, no. 3, pp. 510–519, Mar. 1961.

[37] N. M. Gabor, Z. Zhong, K. Bosnick, J. Park, and P. L. McEuen, "Extremely Efficient Multiple Electron-Hole Pair Generation in Carbon Nanotube Photodiodes," *Science*, vol. 325, no. 5946, pp. 1367–1371, Sep. 2009.

[38] W. A. Tisdale, K. J. Williams, B. A. Timp, D. J. Norris, E. S. Aydil, and X.-Y. Zhu, "Hot-Electron Transfer from Semiconductor Nanocrystals," *Science*, vol. 328, no. 5985, pp. 1543–1547, Jun. 2010.

[39] J. B. Sambur, T. Novet, and B. A. Parkinson, "Multiple Exciton Collection in a Sensitized Photovoltaic System," *Science*, vol. 330, no. 6000, pp. 63–66, Oct. 2010.

[40] R. D. Schaller and V. I. Klimov, "High Efficiency Carrier Multiplication in PbSe

Nanocrystals: Implications for Solar Energy Conversion," *Phys. Rev. Lett.*, vol. 92, no. 18, p. 186601, May 2004.

[41] L. M. Malard, M. A. Pimenta, G. Dresselhaus, and M. S. Dresselhaus, "Raman spectroscopy in graphene," *Phys. Rep.*, vol. 473, no. 5–6, pp. 51–87, Apr. 2009.

[42] M. Lazzeri, C. Attaccalite, L. Wirtz, and F. Mauri, "Impact of the electron-electron correlation on phonon dispersion: Failure of LDA and GGA DFT functionals in graphene and graphite," *Phys. Rev. B*, vol. 78, no. 8, p. 081406, Aug. 2008.

[43] J. Maultzsch, S. Reich, C. Thomsen, H. Requardt, and P. Ordejón, "Phonon Dispersion in Graphite," *Phys. Rev. Lett.*, vol. 92, no. 7, p. 075501, Feb. 2004.

[44] J. M. Dawlaty, S. Shivaraman, M. Chandrashekhar, F. Rana, and M. G. Spencer, "Measurement of ultrafast carrier dynamics in epitaxial graphene," *Appl. Phys. Lett.*, vol. 92, no. 4, p. 042116, Jan. 2008.

[45] H. Wang, J. H. Strait, P. A. George, S. Shivaraman, V. B. Shields, M. Chandrashekhar, J. Hwang, F. Rana, M. G. Spencer, C. S. Ruiz-Vargas, and J. Park, "Ultrafast relaxation dynamics of hot optical phonons in graphene," *Appl. Phys. Lett.*, vol. 96, no. 8, p. 081917, Feb. 2010.

[46] M. Breusing, C. Ropers, and T. Elsaesser, "Ultrafast Carrier Dynamics in Graphite," *Phys. Rev. Lett.*, vol. 102, no. 8, p. 086809, Feb. 2009.

[47] J. H. Strait, H. Wang, S. Shivaraman, V. Shields, M. Spencer, and F. Rana, "Very Slow Cooling Dynamics of Photoexcited Carriers in Graphene Observed by Optical-Pump Terahertz-Probe Spectroscopy," *Nano Lett.*, vol. 11, no. 11, pp. 4902–4906, Nov. 2011.

[48] R. Bistritzer and A. H. MacDonald, "Electronic Cooling in Graphene," *Phys. Rev. Lett.*, vol. 102, no. 20, p. 206410, May 2009.

[49] M. W. Graham, S.-F. Shi, D. C. Ralph, J. Park, and P. L. McEuen, "Photocurrent measurements of supercollision cooling in graphene," *Nat. Phys.*, vol. 9, no. 2, pp. 103–108, Feb. 2013.

[50] J. C. W. Song, M. Y. Reizer, and L. S. Levitov, "Disorder-Assisted Electron-Phonon Scattering and Cooling Pathways in Graphene," *Phys. Rev. Lett.*, vol. 109, no. 10, p. 106602, Sep. 2012.

[51] A. C. Betz, S. H. Jhang, E. Pallecchi, R. Ferreira, G. Fève, J.-M. Berroir, and B. Plaçais, "Supercollision cooling in undoped graphene," *Nat. Phys.*, vol. 9, no. 2, pp. 109–112, Feb. 2013.

[52] W.-T. Liu, S. W. Wu, P. J. Schuck, M. Salmeron, Y. R. Shen, and F. Wang, "Nonlinear broadband photoluminescence of graphene induced by femtosecond laser irradiation," *Phys. Rev. B*, vol. 82, no. 8, p. 081408, Aug. 2010.

[53] C. H. Lui, K. F. Mak, J. Shan, and T. F. Heinz, “Ultrafast Photoluminescence from Graphene,” *Phys. Rev. Lett.*, vol. 105, no. 12, p. 127404, Sep. 2010.

[54] K. J. Tielrooij, J. C. W. Song, S. A. Jensen, A. Centeno, A. Pesquera, A. Zurutuza Elorza, M. Bonn, L. S. Levitov, and F. H. L. Koppens, “Photoexcitation cascade and multiple hot-carrier generation in graphene,” *Nat. Phys.*, vol. 9, no. 4, pp. 248–252, Apr. 2013.

[55] A. B. Kuzmenko, E. van Heumen, F. Carbone, and D. van der Marel, “Universal Optical Conductance of Graphite,” *Phys. Rev. Lett.*, vol. 100, no. 11, p. 117401, Mar. 2008.

[56] R. R. Nair, P. Blake, A. N. Grigorenko, K. S. Novoselov, T. J. Booth, T. Stauber, N. M. R. Peres, and A. K. Geim, “Fine Structure Constant Defines Visual Transparency of Graphene,” *Science*, vol. 320, no. 5881, pp. 1308–1308, Jun. 2008.

[57] C. Berger, Z. Song, T. Li, X. Li, A. Y. Ogbazghi, R. Feng, Z. Dai, A. N. Marchenkov, E. H. Conrad, P. N. First, and W. A. de Heer, “Ultrathin Epitaxial Graphite: 2D Electron Gas Properties and a Route toward Graphene-based Nanoelectronics,” *J. Phys. Chem. B*, vol. 108, no. 52, pp. 19912–19916, Dec. 2004.

[58] P. W. Sutter, J.-I. Flege, and E. A. Sutter, “Epitaxial graphene on ruthenium,” *Nat. Mater.*, vol. 7, no. 5, pp. 406–411, May 2008.

[59] G. Eda, G. Fanchini, and M. Chhowalla, “Large-area ultrathin films of reduced graphene oxide as a transparent and flexible electronic material,” *Nat. Nanotechnol.*, vol. 3, no. 5, pp. 270–274, May 2008.

[60] Y. Hernandez, V. Nicolosi, M. Lotya, F. M. Blighe, Z. Sun, S. De, I. T. McGovern, B. Holland, M. Byrne, Y. K. Gun’Ko, J. J. Boland, P. Niraj, G. Duesberg, S. Krishnamurthy, R. Goodhue, J. Hutchison, V. Scardaci, A. C. Ferrari, and J. N. Coleman, “High-yield production of graphene by liquid-phase exfoliation of graphite,” *Nat. Nanotechnol.*, vol. 3, no. 9, pp. 563–568, Sep. 2008.

[61] M. Lotya, Y. Hernandez, P. J. King, R. J. Smith, V. Nicolosi, L. S. Karlsson, F. M. Blighe, S. De, Z. Wang, I. T. McGovern, G. S. Duesberg, and J. N. Coleman, “Liquid Phase Production of Graphene by Exfoliation of Graphite in Surfactant/Water Solutions,” *J. Am. Chem. Soc.*, vol. 131, no. 10, pp. 3611–3620, Mar. 2009.

[62] D. V. Kosynkin, A. L. Higginbotham, A. Sinitskii, J. R. Lomeda, A. Dimiev, B. K. Price, and J. M. Tour, “Longitudinal unzipping of carbon nanotubes to form graphene nanoribbons,” *Nature*, vol. 458, no. 7240, pp. 872–876, Apr. 2009.

[63] W. Choi, I. Lahiri, R. Seelaboyina, and Y. S. Kang, “Synthesis of Graphene and Its Applications: A Review,” *Crit. Rev. Solid State Mater. Sci.*, vol. 35, no. 1, pp. 52–71, Feb. 2010.

[64] S. Bae, H. Kim, Y. Lee, X. Xu, J.-S. Park, Y. Zheng, J. Balakrishnan, T. Lei, H. Ri Kim, Y. I. Song, Y.-J. Kim, K. S. Kim, B. Özyilmaz, J.-H. Ahn, B. H. Hong, and S. Iijima, "Roll-to-roll production of 30-inch graphene films for transparent electrodes," *Nat. Nanotechnol.*, vol. 5, no. 8, pp. 574–578, Aug. 2010.

[65] X. Li, Y. Zhu, W. Cai, M. Borysiak, B. Han, D. Chen, R. D. Piner, L. Colombo, and R. S. Ruoff, "Transfer of Large-Area Graphene Films for High-Performance Transparent Conductive Electrodes," *Nano Lett.*, vol. 9, no. 12, pp. 4359–4363, Dec. 2009.

[66] A. Reina, X. Jia, J. Ho, D. Nezich, H. Son, V. Bulovic, M. S. Dresselhaus, and J. Kong, "Large Area, Few-Layer Graphene Films on Arbitrary Substrates by Chemical Vapor Deposition," *Nano Lett.*, vol. 9, no. 1, pp. 30–35, Jan. 2009.

[67] S. Lee, K. Lee, and Z. Zhong, "Wafer Scale Homogeneous Bilayer Graphene Films by Chemical Vapor Deposition," *Nano Lett.*, vol. 10, no. 11, pp. 4702–4707, Nov. 2010.

[68] X. Li, W. Cai, J. An, S. Kim, J. Nah, D. Yang, R. Piner, A. Velamakanni, I. Jung, E. Tutuc, S. K. Banerjee, L. Colombo, and R. S. Ruoff, "Large-Area Synthesis of High-Quality and Uniform Graphene Films on Copper Foils," *Science*, vol. 324, no. 5932, pp. 1312–1314, Jun. 2009.

[69] T. Gao, S. Xie, Y. Gao, M. Liu, Y. Chen, Y. Zhang, and Z. Liu, "Growth and Atomic-Scale Characterizations of Graphene on Multifaceted Textured Pt Foils Prepared by Chemical Vapor Deposition," *ACS Nano*, vol. 5, no. 11, pp. 9194–9201, Nov. 2011.

[70] J. Martin, N. Akerman, G. Ulbricht, T. Lohmann, J. H. Smet, K. von Klitzing, and A. Yacoby, "Observation of electron–hole puddles in graphene using a scanning single-electron transistor," *Nat. Phys.*, vol. 4, no. 2, pp. 144–148, Feb. 2008.

[71] P. Y. Huang, C. S. Ruiz-Vargas, A. M. van der Zande, W. S. Whitney, M. P. Levendorf, J. W. Kevek, S. Garg, J. S. Alden, C. J. Hustedt, Y. Zhu, J. Park, P. L. McEuen, and D. A. Muller, "Grains and grain boundaries in single-layer graphene atomic patchwork quilts," *Nature*, vol. 469, no. 7330, pp. 389–392, Jan. 2011.

[72] J. C. Meyer, C. Kisielowski, R. Erni, M. D. Rossell, M. F. Crommie, and A. Zettl, "Direct Imaging of Lattice Atoms and Topological Defects in Graphene Membranes," *Nano Lett.*, vol. 8, no. 11, pp. 3582–3586, Nov. 2008.

[73] C. Mattevi, H. Kim, and M. Chhowalla, "A review of chemical vapour deposition of graphene on copper," *J Mater Chem*, vol. 21, no. 10, pp. 3324–3334, 2011.

[74] X. Li, W. Cai, L. Colombo, and R. S. Ruoff, "Evolution of Graphene Growth on Ni and Cu by Carbon Isotope Labeling," *Nano Lett.*, vol. 9, no. 12, pp. 4268–4272, Dec.

2009.

[75] A. S. Sedra and K. C. Smith, *Microelectronic Circuits*. Oxford University Press, USA, 2007.

[76] B. Razavi, *Design of Analog CMOS Integrated Circuits*. McGraw-Hill, 2001.

[77] Y. Zhang, Y.-W. Tan, H. L. Stormer, and P. Kim, "Experimental observation of the quantum Hall effect and Berry's phase in graphene," *Nature*, vol. 438, no. 7065, pp. 201–204, Nov. 2005.

[78] T. Palacios, A. Hsu, and H. Wang, "Applications of graphene devices in RF communications," *IEEE Commun. Mag.*, vol. 48, no. 6, pp. 122–128, Jun. 2010.

[79] S. Lee and Z. Zhong, "Nanoelectronic circuits based on two-dimensional atomic layer crystals," *Nanoscale*, vol. 6, no. 22, pp. 13283–13300, Oct. 2014.

[80] H. Wang, A. Hsu, J. Wu, J. Kong, and T. Palacios, "Graphene-Based Ambipolar RF Mixers," *IEEE Electron Device Lett.*, vol. 31, no. 9, pp. 906–908, Sep. 2010.

[81] H. Madan, M. J. Hollander, M. LaBella, R. Cavalero, D. Snyder, J. A. Robinson, and S. Datta, "Record high conversion gain ambipolar graphene mixer at 10GHz using scaled gate oxide," in *Electron Devices Meeting (IEDM), 2012 IEEE International*, 2012, pp. 4.3.1–4.3.4.

[82] O. Habibpour, J. Vukusic, and J. Stake, "A 30-GHz Integrated Subharmonic Mixer Based on a Multichannel Graphene FET," *IEEE Trans. Microw. Theory Tech.*, vol. 61, no. 2, pp. 841–847, Feb. 2013.

[83] J. S. Moon, H.-C. Seo, M. Antcliffe, D. Le, C. McGuire, A. Schmitz, L. O. Nyakiti, D. K. Gaskill, P. M. Campbell, K.-M. Lee, and P. Asbeck, "Graphene FETs for Zero-Bias Linear Resistive FET Mixers," *IEEE Electron Device Lett.*, vol. 34, no. 3, pp. 465–467, Mar. 2013.

[84] Z. Wang, Z. Zhang, H. Xu, L. Ding, S. Wang, and L.-M. Peng, "A high-performance top-gate graphene field-effect transistor based frequency doubler," *Appl. Phys. Lett.*, vol. 96, no. 17, p. 173104, Apr. 2010.

[85] M. E. Ramon, K. N. Parrish, J. Lee, C. W. Magnuson, L. Tao, R. S. Ruoff, S. K. Banerjee, and D. Akinwande, "Graphene frequency doubler with record 3GHz bandwidth and the maximum conversion gain prospects," in *Microwave Symposium Digest (MTT), 2012 IEEE MTT-S International*, 2012, pp. 1–3.

[86] H.-Y. Chen and J. Appenzeller, "Graphene-Based Frequency Tripler," *Nano Lett.*, vol. 12, no. 4, pp. 2067–2070, Apr. 2012.

[87] H. Wang, D. Nezich, J. Kong, and T. Palacios, "Graphene Frequency Multipliers," *IEEE Electron Device Lett.*, vol. 30, no. 5, pp. 547–549, May 2009.

[88] H. Wang, A. Hsu, K. K. Kim, J. Kong, and T. Palacios, "Gigahertz ambipolar

frequency multiplier based on CVD graphene," in *Electron Devices Meeting (IEDM), 2010 IEEE International*, 2010, pp. 23.6.1–23.6.4.

[89] M. Dragoman, A. A. Muller, D. Dragoman, F. Coccetti, and R. Plana, "Terahertz antenna based on graphene," *J. Appl. Phys.*, vol. 107, no. 10, p. 104313, May 2010.

[90] M. Tamagnone, J. S. Gómez-Díaz, J. R. Mosig, and J. Perruisseau-Carrier, "Reconfigurable terahertz plasmonic antenna concept using a graphene stack," *Appl. Phys. Lett.*, vol. 101, no. 21, p. 214102, Nov. 2012.

[91] I. Llatser, C. Kremers, A. Cabellos-Aparicio, J. M. Jornet, E. Alarcón, and D. N. Chigrin, "Graphene-based nano-patch antenna for terahertz radiation," *Photonics Nanostructures - Fundam. Appl.*, vol. 10, no. 4, pp. 353–358, Oct. 2012.

[92] S.-J. Han, A. V. Garcia, S. Oida, K. A. Jenkins, and W. Haensch, "Graphene radio frequency receiver integrated circuit," *Nat. Commun.*, vol. 5, Jan. 2014.

[93] R. Sordan, F. Traversi, and V. Russo, "Logic gates with a single graphene transistor," *Appl. Phys. Lett.*, vol. 94, no. 7, p. 073305, Feb. 2009.

[94] F. Traversi, V. Russo, and R. Sordan, "Integrated complementary graphene inverter," *Appl. Phys. Lett.*, vol. 94, no. 22, p. 223312, Jun. 2009.

[95] N. Harada, K. Yagi, S. Sato, and N. Yokoyama, "A polarity-controllable graphene inverter," *Appl. Phys. Lett.*, vol. 96, no. 1, p. 012102, Jan. 2010.

[96] S.-L. Li, H. Miyazaki, A. Kumatani, A. Kanda, and K. Tsukagoshi, "Low Operating Bias and Matched Input−Output Characteristics in Graphene Logic Inverters," *Nano Lett.*, vol. 10, no. 7, pp. 2357–2362, Jul. 2010.

[97] S. Lee, K. Lee, C.-H. Liu, G. S. Kulkarni, and Z. Zhong, "Flexible and transparent all-graphene circuits for quaternary digital modulations," *Nat. Commun.*, vol. 3, p. 1018, Aug. 2012.

[98] B. Sensale-Rodriguez, R. Yan, M. M. Kelly, T. Fang, K. Tahy, W. S. Hwang, D. Jena, L. Liu, and H. G. Xing, "Broadband graphene terahertz modulators enabled by intraband transitions," *Nat. Commun.*, vol. 3, p. 780, Apr. 2012.

[99] J. S. Bunch, A. M. van der Zande, S. S. Verbridge, I. W. Frank, D. M. Tanenbaum, J. M. Parpia, H. G. Craighead, and P. L. McEuen, "Electromechanical Resonators from Graphene Sheets," *Science*, vol. 315, no. 5811, pp. 490–493, Jan. 2007.

[100] C. Chen, S. Rosenblatt, K. I. Bolotin, W. Kalb, P. Kim, I. Kymissis, H. L. Stormer, T. F. Heinz, and J. Hone, "Performance of monolayer graphene nanomechanical resonators with electrical readout," *Nat. Nanotechnol.*, vol. 4, no. 12, pp. 861–867, Dec. 2009.

[101] K. M. Milaninia, M. A. Baldo, A. Reina, and J. Kong, "All graphene electromechanical switch fabricated by chemical vapor deposition," *Appl. Phys. Lett.*,

vol. 95, no. 18, p. 183105, Nov. 2009.

[102] Y.-M. Lin, A. Valdes-Garcia, S.-J. Han, D. B. Farmer, I. Meric, Y. Sun, Y. Wu, C. Dimitrakopoulos, A. Grill, P. Avouris, and K. A. Jenkins, "Wafer-Scale Graphene Integrated Circuit," *Science*, vol. 332, no. 6035, pp. 1294–1297, Jun. 2011.

[103] T. Georgiou, R. Jalil, B. D. Belle, L. Britnell, R. V. Gorbachev, S. V. Morozov, Y.-J. Kim, A. Gholinia, S. J. Haigh, O. Makarovsky, L. Eaves, L. A. Ponomarenko, A. K. Geim, K. S. Novoselov, and A. Mishchenko, "Vertical field-effect transistor based on graphene-WS2 heterostructures for flexible and transparent electronics," *Nat. Nanotechnol.*, vol. 8, no. 2, pp. 100–103, Feb. 2013.

[104] S. Kim, J. Nah, I. Jo, D. Shahrjerdi, L. Colombo, Z. Yao, E. Tutuc, and S. K. Banerjee, "Realization of a high mobility dual-gated graphene field-effect transistor with Al2O3 dielectric," *Appl. Phys. Lett.*, vol. 94, no. 6, p. 062107, Feb. 2009.

[105] S.-J. Han, K. A. Jenkins, A. Valdes Garcia, A. D. Franklin, A. A. Bol, and W. Haensch, "High-Frequency Graphene Voltage Amplifier," *Nano Lett.*, vol. 11, no. 9, pp. 3690–3693, Sep. 2011.

[106] M. A. Andersson, O. Habibpour, J. Vukusic, and J. Stake, "10 dB small-signal graphene FET amplifier," *Electron. Lett.*, vol. 48, no. 14, pp. 861–863, Jul. 2012.

[107] R. Van Noorden, "Moving towards a graphene world," *Nature*, vol. 442, no. 7100, pp. 228–229, Jul. 2006.

[108] M. Taghioskoui, "Trends in graphene research," *Mater. Today*, vol. 12, no. 10, pp. 34–37, Oct. 2009.

[109] R. K. Cavin, P. Lugli, and V. V. Zhirnov, "Science and Engineering Beyond Moore's Law," *Proc. IEEE*, vol. 100, no. Special Centennial Issue, pp. 1720–1749, May 2012.

[110] J. Wu, Y.-L. Shen, K. Reinhardt, H. Szu, and B. Dong, "A Nanotechnology Enhancement to Moore's Law," *Appl Comp Intell Soft Comput*, vol. 2013, pp. 2:2–2:2, Jan. 2013.

[111] D. R. Smith and D. Schurig, "Electromagnetic Wave Propagation in Media with Indefinite Permittivity and Permeability Tensors," *Phys. Rev. Lett.*, vol. 90, no. 7, p. 077405, Feb. 2003.

[112] A. Poddubny, I. Iorsh, P. Belov, and Y. Kivshar, "Hyperbolic metamaterials," *Nat. Photonics*, vol. 7, no. 12, pp. 948–957, Dec. 2013.

[113] Z. Jacob, J.-Y. Kim, G. V. Naik, A. Boltasseva, E. E. Narimanov, and V. M. Shalaev, "Engineering photonic density of states using metamaterials," *Appl. Phys. B*, vol. 100, no. 1, pp. 215–218, Jun. 2010.

[114] H. N. S. Krishnamoorthy, Z. Jacob, E. Narimanov, I. Kretzschmar, and V. M.

Menon, “Topological Transitions in Metamaterials,” *Science*, vol. 336, no. 6078, pp. 205–209, Apr. 2012.

[115] C. Guclu, S. Campione, and F. Capolino, “Hyperbolic metamaterial as super absorber for scattered fields generated at its surface,” *Phys. Rev. B*, vol. 86, no. 20, p. 205130, Nov. 2012.

[116] S.-A. Biehs, M. Tschikin, R. Messina, and P. Ben-Abdallah, “Super-Planckian near-field thermal emission with phonon-polaritonic hyperbolic metamaterials,” *Appl. Phys. Lett.*, vol. 102, no. 13, p. 131106, Apr. 2013.

[117] Z. Liu, H. Lee, Y. Xiong, C. Sun, and X. Zhang, “Far-Field Optical Hyperlens Magnifying Sub-Diffraction-Limited Objects,” *Science*, vol. 315, no. 5819, pp. 1686–1686, Mar. 2007.

[118] E. E. Narimanov and A. V. Kildishev, “Metamaterials: Naturally hyperbolic,” *Nat. Photonics*, vol. 9, no. 4, pp. 214–216, Apr. 2015.

[119] S. Dai, Z. Fei, Q. Ma, A. S. Rodin, M. Wagner, A. S. McLeod, M. K. Liu, W. Gannett, W. Regan, K. Watanabe, T. Taniguchi, M. Thiemens, G. Dominguez, A. H. C. Neto, A. Zettl, F. Keilmann, P. Jarillo-Herrero, M. M. Fogler, and D. N. Basov, “Tunable Phonon Polaritons in Atomically Thin van der Waals Crystals of Boron Nitride,” *Science*, vol. 343, no. 6175, pp. 1125–1129, Mar. 2014.

[120] J. D. Caldwell, A. V. Kretinin, Y. Chen, V. Giannini, M. M. Fogler, Y. Francescato, C. T. Ellis, J. G. Tischler, C. R. Woods, A. J. Giles, M. Hong, K. Watanabe, T. Taniguchi, S. A. Maier, and K. S. Novoselov, “Sub-diffractional volume-confined polaritons in the natural hyperbolic material hexagonal boron nitride,” *Nat. Commun.*, vol. 5, p. 5221, Oct. 2014.

[121] M. A. Noginov, Y. A. Barnakov, G. Zhu, T. Tumkur, H. Li, and E. E. Narimanov, “Bulk photonic metamaterial with hyperbolic dispersion,” *Appl. Phys. Lett.*, vol. 94, no. 15, p. 151105, Apr. 2009.

[122] A. J. Hoffman, L. Alekseyev, S. S. Howard, K. J. Franz, D. Wasserman, V. A. Podolskiy, E. E. Narimanov, D. L. Sivco, and C. Gmachl, “Negative refraction in semiconductor metamaterials,” *Nat. Mater.*, vol. 6, no. 12, pp. 946–950, Dec. 2007.

[123] M. A. K. Othman, C. Guclu, and F. Capolino, “Graphene–dielectric composite metamaterials: evolution from elliptic to hyperbolic wavevector dispersion and the transverse epsilon-near-zero condition,” *J. Nanophotonics*, vol. 7, no. 1, pp. 073089–073089, 2013.

[124] M. A. K. Othman, C. Guclu, and F. Capolino, “Graphene-based tunable hyperbolic metamaterials and enhanced near-field absorption,” *Opt. Express*, vol. 21, no. 6, p. 7614, Mar. 2013.

[125] B. Wang, X. Zhang, F. J. García-Vidal, X. Yuan, and J. Teng, "Strong Coupling of Surface Plasmon Polaritons in Monolayer Graphene Sheet Arrays," *Phys. Rev. Lett.*, vol. 109, no. 7, p. 073901, Aug. 2012.

[126] Y.-C. Chang, A. V. Kildishev, E. E. Narimanov, C.-H. Liu, C.-H. Liu, S. Zhang, S. R. Marder, Z. Zhong, and T. B. Norris, "Mid-infrared hyperbolic metamaterial based on graphene-dielectric multilayers," 2015, vol. 9544, pp. 954417–954417–8.

[127] I. S. Nefedov, C. A. Valaginnopoulos, and L. A. Melnikov, "Perfect absorption in graphene multilayers," *J. Opt.*, vol. 15, no. 11, p. 114003, 2013.

[128] K. V. Sreekanth, A. D. Luca, and G. Strangi, "Negative refraction in graphene-based hyperbolic metamaterials," *Appl. Phys. Lett.*, vol. 103, no. 2, p. 023107, Jul. 2013.

[129] A. Andryieuski, A. V. Lavrinenko, and D. N. Chigrin, "Graphene hyperlens for terahertz radiation," *Phys. Rev. B*, vol. 86, no. 12, p. 121108, Sep. 2012.

[130] O. Kidwai, S. V. Zhukovsky, and J. E. Sipe, "Effective-medium approach to planar multilayer hyperbolic metamaterials: Strengths and limitations," *Phys. Rev. A*, vol. 85, no. 5, p. 053842, May 2012.

[131] M. Liu, X. Yin, E. Ulin-Avila, B. Geng, T. Zentgraf, L. Ju, F. Wang, and X. Zhang, "A graphene-based broadband optical modulator," *Nature*, vol. 474, no. 7349, pp. 64–67, Jun. 2011.

[132] Q. Bao, H. Zhang, Y. Wang, Z. Ni, Y. Yan, Z. X. Shen, K. P. Loh, and D. Y. Tang, "Atomic-Layer Graphene as a Saturable Absorber for Ultrafast Pulsed Lasers," *Adv. Funct. Mater.*, vol. 19, no. 19, pp. 3077–3083, Oct. 2009.

[133] S. H. Lee, J. Choi, H.-D. Kim, H. Choi, and B. Min, "Ultrafast refractive index control of a terahertz graphene metamaterial," *Sci. Rep.*, vol. 3, Jul. 2013.

[134] N. M. Gabor, J. C. W. Song, Q. Ma, N. L. Nair, T. Taychatanapat, K. Watanabe, T. Taniguchi, L. S. Levitov, and P. Jarillo-Herrero, "Hot Carrier–Assisted Intrinsic Photoresponse in Graphene," *Science*, vol. 334, no. 6056, pp. 648–652, Nov. 2011.

[135] J. Yan, M.-H. Kim, J. A. Elle, A. B. Sushkov, G. S. Jenkins, H. M. Milchberg, M. S. Fuhrer, and H. D. Drew, "Dual-gated bilayer graphene hot-electron bolometer," *Nat. Nanotechnol.*, vol. 7, no. 7, pp. 472–478, Jul. 2012.

[136] C.-H. Liu, Y.-C. Chang, S. Lee, Y. Zhang, Y. Zhang, T. B. Norris, and Z. Zhong, "Ultrafast Lateral Photo-Dember Effect in Graphene Induced by Nonequilibrium Hot Carrier Dynamics," *Nano Lett.*, vol. 15, no. 6, pp. 4234–4239, Jun. 2015.

[137] E. H. Hwang, S. Adam, and S. D. Sarma, "Carrier Transport in Two-Dimensional Graphene Layers," *Phys. Rev. Lett.*, vol. 98, no. 18, p. 186806, May 2007.

[138] A. Tarasov, S. Zhang, M.-Y. Tsai, P. M. Campbell, S. Graham, S. Barlow, S. R. Marder, and E. M. Vogel, "Controlled Doping of Large-Area Trilayer $MoS_2$ with Molecular Reductants and Oxidants," *Adv. Mater.*, vol. 27, no. 7, pp. 1175–1181, Feb. 2015.

[139] S. A. Paniagua, J. Baltazar, H. Sojoudi, S. K. Mohapatra, S. Zhang, C. L. Henderson, S. Graham, S. Barlow, and S. R. Marder, "Production of heavily n- and p-doped CVD graphene with solution-processed redox-active metal–organic species," *Mater. Horiz.*, vol. 1, no. 1, pp. 111–115, Nov. 2013.

[140] K. F. Mak, J. Shan, and T. F. Heinz, "Seeing Many-Body Effects in Single- and Few-Layer Graphene: Observation of Two-Dimensional Saddle-Point Excitons," *Phys. Rev. Lett.*, vol. 106, no. 4, p. 046401, Jan. 2011.

[141] L. Yang, J. Deslippe, C.-H. Park, M. L. Cohen, and S. G. Louie, "Excitonic Effects on the Optical Response of Graphene and Bilayer Graphene," *Phys. Rev. Lett.*, vol. 103, no. 18, p. 186802, Oct. 2009.

[142] L. Banszerus, M. Schmitz, S. Engels, J. Dauber, M. Oellers, F. Haupt, K. Watanabe, T. Taniguchi, B. Beschoten, and C. Stampfer, "Ultrahigh-mobility graphene devices from chemical vapor deposition on reusable copper," *Sci. Adv.*, vol. 1, no. 6, p. e1500222, Jul. 2015.

[143] Y. Hao, M. S. Bharathi, L. Wang, Y. Liu, H. Chen, S. Nie, X. Wang, H. Chou, C. Tan, B. Fallahazad, H. Ramanarayan, C. W. Magnuson, E. Tutuc, B. I. Yakobson, K. F. McCarty, Y.-W. Zhang, P. Kim, J. Hone, L. Colombo, and R. S. Ruoff, "The Role of Surface Oxygen in the Growth of Large Single-Crystal Graphene on Copper," *Science*, vol. 342, no. 6159, pp. 720–723, Nov. 2013.

[144] A. Rogalski, "Infrared detectors: status and trends," *Prog. Quantum Electron.*, vol. 27, no. 2–3, pp. 59–210, 2003.

[145] J. Clark and G. Lanzani, "Organic photonics for communications," *Nat. Photonics*, vol. 4, no. 7, pp. 438–446, Jul. 2010.

[146] K. F. Mak, L. Ju, F. Wang, and T. F. Heinz, "Optical spectroscopy of graphene: From the far infrared to the ultraviolet," *Solid State Commun.*, vol. 152, no. 15, pp. 1341–1349, Aug. 2012.

[147] J. Park, Y. H. Ahn, and C. Ruiz-Vargas, "Imaging of Photocurrent Generation and Collection in Single-Layer Graphene," *Nano Lett.*, vol. 9, no. 5, pp. 1742–1746, May 2009.

[148] F. Xia, T. Mueller, R. Golizadeh-Mojarad, M. Freitag, Y. Lin, J. Tsang, V. Perebeinos, and P. Avouris, "Photocurrent Imaging and Efficient Photon Detection in a Graphene Transistor," *Nano Lett.*, vol. 9, no. 3, pp. 1039–1044, Mar. 2009.

[149] F. Xia, T. Mueller, Y. Lin, A. Valdes-Garcia, and P. Avouris, “Ultrafast graphene photodetector,” *Nat. Nanotechnol.*, vol. 4, no. 12, pp. 839–843, Dec. 2009.

[150] T. Mueller, F. Xia, and P. Avouris, “Graphene photodetectors for high-speed optical communications,” *Nat. Photonics*, vol. 4, no. 5, pp. 297–301, May 2010.

[151] C.-H. Liu, N. M. Dissanayake, S. Lee, K. Lee, and Z. Zhong, “Evidence for Extraction of Photoexcited Hot Carriers from Graphene,” *ACS Nano*, vol. 6, no. 8, pp. 7172–7176, Aug. 2012.

[152] X. Xu, N. M. Gabor, J. S. Alden, A. M. van der Zande, and P. L. McEuen, “Photo-Thermoelectric Effect at a Graphene Interface Junction,” *Nano Lett.*, vol. 10, no. 2, pp. 562–566, Feb. 2010.

[153] T. J. Echtermeyer, L. Britnell, P. K. Jasnos, A. Lombardo, R. V. Gorbachev, A. N. Grigorenko, A. K. Geim, A. C. Ferrari, and K. S. Novoselov, “Strong plasmonic enhancement of photovoltage in graphene,” *Nat. Commun.*, vol. 2, p. 458, Aug. 2011.

[154] Z. Fang, Z. Liu, Y. Wang, P. M. Ajayan, P. Nordlander, and N. J. Halas, “Graphene-Antenna Sandwich Photodetector,” *Nano Lett.*, vol. 12, no. 7, pp. 3808–3813, Jul. 2012.

[155] A. N. Grigorenko, M. Polini, and K. S. Novoselov, “Graphene plasmonics,” *Nat. Photonics*, vol. 6, no. 11, pp. 749–758, Nov. 2012.

[156] M. Furchi, A. Urich, A. Pospischil, G. Lilley, K. Unterrainer, H. Detz, P. Klang, A. M. Andrews, W. Schrenk, G. Strasser, and T. Mueller, “Microcavity-Integrated Graphene Photodetector,” *Nano Lett.*, vol. 12, no. 6, pp. 2773–2777, Jun. 2012.

[157] M. Engel, M. Steiner, A. Lombardo, A. C. Ferrari, H. v Löhneysen, P. Avouris, and R. Krupke, “Light–matter interaction in a microcavity-controlled graphene transistor,” *Nat. Commun.*, vol. 3, p. 906, Jun. 2012.

[158] L. Britnell, R. M. Ribeiro, A. Eckmann, R. Jalil, B. D. Belle, A. Mishchenko, Y.-J. Kim, R. V. Gorbachev, T. Georgiou, S. V. Morozov, A. N. Grigorenko, A. K. Geim, C. Casiraghi, A. H. C. Neto, and K. S. Novoselov, “Strong Light-Matter Interactions in Heterostructures of Atomically Thin Films,” *Science*, vol. 340, no. 6138, pp. 1311–1314, Jun. 2013.

[159] B. Y. Zhang, T. Liu, B. Meng, X. Li, G. Liang, X. Hu, and Q. J. Wang, “Broadband high photoresponse from pure monolayer graphene photodetector,” *Nat. Commun.*, vol. 4, p. 1811, May 2013.

[160] M. Freitag, T. Low, F. Xia, and P. Avouris, “Photoconductivity of biased graphene,” *Nat. Photonics*, vol. 7, no. 1, pp. 53–59, Jan. 2013.

[161] D. Brida, A. Tomadin, C. Manzoni, Y. J. Kim, A. Lombardo, S. Milana, R. R. Nair, K. S. Novoselov, A. C. Ferrari, G. Cerullo, and M. Polini, “Ultrafast collinear

scattering and carrier multiplication in graphene," *Nat. Commun.*, vol. 4, p. 1987, Jun. 2013.

[162] G. Konstantatos, M. Badioli, L. Gaudreau, J. Osmond, M. Bernechea, F. P. G. de Arquer, F. Gatti, and F. H. L. Koppens, "Hybrid graphene-quantum dot phototransistors with ultrahigh gain," *Nat. Nanotechnol.*, vol. 7, no. 6, pp. 363–368, Jun. 2012.

[163] Z. Sun, Z. Liu, J. Li, G. Tai, S.-P. Lau, and F. Yan, "Infrared Photodetectors Based on CVD-Grown Graphene and PbS Quantum Dots with Ultrahigh Responsivity," *Adv. Mater.*, vol. 24, no. 43, pp. 5878–5883, Nov. 2012.

[164] G. Konstantatos and E. H. Sargent, "Nanostructured materials for photon detection," *Nat. Nanotechnol.*, vol. 5, no. 6, pp. 391–400, Jun. 2010.

[165] S. Lee, K. Lee, C.-H. Liu, and Z. Zhong, "Homogeneous bilayer graphene film based flexible transparent conductor," *Nanoscale*, vol. 4, no. 2, pp. 639–644, Jan. 2012.

[166] J. C. W. Song, M. S. Rudner, C. M. Marcus, and L. S. Levitov, "Hot Carrier Transport and Photocurrent Response in Graphene," *Nano Lett.*, vol. 11, no. 11, pp. 4688–4692, Nov. 2011.

[167] P. Thissen, B. Schindler, D. Diesing, and E. Hasselbrink, "Optical response of metal–insulator–metal heterostructures and their application for the detection of chemicurrents," *New J. Phys.*, vol. 12, no. 11, p. 113014, 2010.

[168] X. Li, H. Zhu, K. Wang, A. Cao, J. Wei, C. Li, Y. Jia, Z. Li, X. Li, and D. Wu, "Graphene-On-Silicon Schottky Junction Solar Cells," *Adv. Mater.*, vol. 22, no. 25, pp. 2743–2748, Jul. 2010.

[169] K. S. Novoselov, V. I. Fal′ko, L. Colombo, P. R. Gellert, M. G. Schwab, and K. Kim, "A roadmap for graphene," *Nature*, vol. 490, no. 7419, pp. 192–200, Oct. 2012.